ALMA MATER STUDIORUM - UNIVERSITÀ DI BOLOGNA

SCUOLA DI SCIENZE

CORSO DI LAUREA MAGISTRALE IN FISICA DEL SISTEMA TERRA

Analysis of the aerosol number size distribution variability and characterization of new particle formation events at Monte Cimone GAW global station

Relatore:
Prof. Federico Porcù

Candidata:
Martina Mazzini

Correlatori:
Dott. Angelo Lupi
Dott.ssa Angela Marinoni

Sessione III
Anno Accademico 2019-2020

Abstract

To better assess how aerosols impact on Earth system, the observations of ultrafine particle number concentration and their size distribution in different location and environments are crucial, especially in remote sites, like high altitude mountain sites, where the atmosphere is representative of baseline conditions.

The aim of this thesis is to obtain long-term information on aerosol number size distribution and new particle formation (NPF) at the Mt. Cimone GAW global station (CMN, 2165 m a.s.l.). The size distribution of particles ranging from 9nm to 500nm was continuously observed with a DMPS from November 2005 to July 2013 in the framework of EUSAAR and ACTRIS European projects. Size distribution and number concentration are studied at different time scales, together with occurrences of NPFs. CMN typical aerosol number size distribution is bimodal. On average, CMN aerosol population features a total number concentration of $1534 \pm 1332\,cm^{-3}$. The number concentration shows large seasonal variations with higher values during warm months, almost four times higher than those observed in winter. On a daily time scale, the maximum of total particles occurs in the afternoon. When classifying aerosol number size distribution into nucleation mode (9-25nm), Aitken mode (25-100nm), and accumulation mode (100-500nm), Aitken mode is the main contributor to the total number concentration for about 53%, followed by particles in the accumulation and nucleation modes with 31% and 16%, respectively.

According to the procedure laid down by Kulmala et al., 2012 NPFs are identified by distinguishing each day following standardised classification criteria. CMN is characterized by a NPF events frequency of 26.7%, with the highest event occurrence in May and August, while non-events are more frequent during winter. The growth of nucleation mode particle and the time evolution of the nucleation number concentration begin, on average, around local noon. The first one lasts almost three hours, with a mean growth rate of $4.65 \pm 1.97\,nm/h$, while the latter lasts more than one hour and a half, with a rate of $0.50 \pm 0.56\,cm^{-3}s^{-1}$. The average condensation sink is $0.280 \cdot 10^{-3}s^{-1}$ during a typical non-event day, and $0.483 \cdot 10^{-3}s^{-1}$ during a typical event day. However, low CS observed before the nucleation onset time can be an important factor triggering NPFs, except during winter season.

Sommario

Una migliore comprensione degli effetti degli aerosol sul sistema climatico beneficia di osservazioni a lungo termine della concentrazione del numero di particelle ultrafini e della loro distribuzione dimensionale in luoghi ed ambienti diversi. Questo vale, in particolare per siti remoti, come quelli ad alta quota, dove l'atmosfera è rappresentativa delle condizioni di background a larga scala.

Lo scopo di questa tesi è ottenere informazioni sulla variabilità delle osservazioni di distribuzione dimensionale in numero degli aerosol e sugli eventi di formazione di nuove particelle (NPF) osservati presso la GAW Global Station di Monte Cimone (CMN, 2165 m s.l.m.). La distribuzione dimensionale di particelle con dimensioni comprese tra 9 nm e 500 nm è stata continuamente monitorata tramite un DMPS, a partire da Novembre 2005 fino a Luglio 2013, nell'ambito dei progetti europei EUSAAR e ACTRIS. In questo elaborato, la distribuzione dimensionale e la concentrazione numerica vengono analizzate considerando scale temporali differenti, insieme agli eventi di NPF.

La distribuzione numerica dimensionale tipica del sito CMN risulta bimodale. In media, la popolazione di aerosol ha una concentrazione totale di $1534 \pm 1332 cm^{-3}$. L'andamento tipico annuale della concentrazione numerica presenta un massimo estivo, quasi quattro volte superiore ai valori osservati mediamente in inverno. Su scala giornaliera, il numero massimo di particelle si osserva nel pomeriggio, molto più accentuato in estate rispetto alle altre stagioni. Suddividendo lo spettro della distribuzione numerica dimensionale nella moda di nucleazione (9-25 nm), nella moda di Aitken (25-100 nm) e nella moda di accumulazione (100-500 nm), la moda di Aitken è quella che contribuisce maggiormente alla concentrazione totale con circa il 53%, seguita dalle mode di accumulazione e nucleazione che contribuiscono rispettivamente con il 31% e il 16%.

Secondo la procedura stabilita da Kulmala et al., 2012, abbiamo identificato gli eventi di NPF, classificando ogni giorno in base a criteri di classificazione noti in letteratura. Presso il sito CMN si registra una frequenza di eventi di NPF del 26.7%, con la più alta presenza di eventi nei mesi di Maggio e Agosto, mentre i non-eventi sono più frequenti durante l'inverno. Nei casi di NPF più chiari, abbiamo studiato la crescita delle particelle nella moda di nucleazione e l'aumento di concentrazione, che iniziano ogni giorno mediamente intorno al mezzogiorno locale. In media, la crescita in diametro dura quasi tre ore, con una velocità di $4.65 \pm 1.97 nm/h$, mentre la crescita in concentrazione dura più di un'ora e mezza, con un rate di $0.50 \pm 0.56 cm^{-3}s^{-1}$. Il condensation sink medio è $0.280 \cdot 10^{-3}s^{-1}$ durante una tipica giornata non-evento, mentre ha un valore medio di $0.483 \cdot 10^{-3}s^{-1}$ durante una giornata in cui avviene NPF. Viene osservato un CS basso prima che la nucleazione abbia inizio, ad eccezione della stagione invernale. Ciò significa che CS può essere considerato un fattore importante per innescare il meccanismo di NPF.

Contents

Introduction

Aerosol particles can influence the Earth radiation budget by scattering and absorbing sunlight (direct effect). They can also affect Earth albedo by serving as cloud condensation nuclei (CCN) and ice nuclei (IN), and thus they can influence cloud formation and lifetime as well (IPCC, 2013). The cloud albedo effect of aerosols is one of the biggest uncertainties in global climate models (IPCC, 2013), and strongly depends on the number concentration and size distribution of particles. Numerous studies have focused on monitoring the particle number size distribution (PNSD) within the planet boundary layer (PBL), where anthropogenic sources have strong impacts (Peng et al., 2014). However, particles in the pristine free troposphere (FT) have rarely been studied. Mountain sites are located far from anthropogenic emissions and thus they are the ideal sites for monitoring the temporal variations of aerosols in the atmosphere at background levels.

The overall aim of this thesis is to enrich the information of aerosol concentration and size distribution by analyzing the longest Italian record gathered by the mountain ground based station *O. Vittori* at Mt. Cimone (2165 m a.s.l.). This station is the only one among the 31 Global Stations of the Global Atmospheric Watch (GAW) program set up by the World Meteorological Organization (WMO) present on the Italian territory and in the Mediterranean Basin. The aerosol number size distribution observation at Mt. Cimone was implemented in the frame of EUSAAR FP6 program, in November 2005, and it has been continuously carried out also in the frame of ACTRIS-FP7 and ACTRIS-2-H2020 programs. This site represents a strategic platform to study the climatology of the free troposphere in the South Europe and the Mediterranean basin. For these reasons, its contribution to extent the view of particle number concentration and size distribution within observational networks is fundamental.

To accomplish this aim, size distributions data collected from a differential mobility particle sizer (DMPS) from November 2005 to July 2013 are analyzed. In particular, information about diurnal, seasonal, annual and inter-annual variability of aerosol number concentration and size distributions is obtained. Then, a study of new particle formation (NPF) is carried out. New particle formation is estimated to provide the 45% of global cloud condensation nuclei, but the abundance of nucleated particles responds

in complex ways to variations in precursor gases, existing particle concentrations, and other environmental factors that are still not completely understood (Merikanto et al., 2009). In order to understand the phenomenon of NPF at Mt. Cimone, we first need to know its frequency and characteristics. For this reason, in the present work a preliminary detailed investigation of NPF event and non event is carried out.

Chapter one provides the most relevant information on tropospheric aerosol. It contains a description of the main sources and removal mechanisms and offers an overview of aerosol particles physical, chemical and electrical properties. This Chapter depicts the key aspects of current knowledge about their impact on visibility, health, and climate. Finally, it deepens into the new particle formation mechanisms and main evolutionary processes to which aerosol particles are subjects in the atmosphere.

Chapter two contains a detailed description of the measurement site and the methodology of NPSD observation and data analysis. First of all, the chapter provides a presentation of the *O. Vittori* atmospheric observatory managed by the National Research Council of Italy. Then, a description of the operating principles of the DMPS, used to measure the aerosol size distribution, is given. Finally, the methods adopted to process raw data and to create a homogeneous data set together with the complete analysis procedure used to analyze it are explained.

Chapter three reports the main results obtained by studying the available data. Starting from a description of the data set obtained through the preprocessing of raw data, the third chapter proceeds with the long-term characterization of the aerosol population measured at Mt. Cimone. The properties of the aerosol population are investigated by outlining the diurnal, monthly, seasonal, and interannual differences in size distributions and number concentrations. Then, the total aerosol number concentration recorded at Mt. Cimone is compared with that observed at other stations in a global context. Finally, the results concerning the observation of new particle formation are reported. In particular, the characteristics of events occurring at Mt. Cimone are studied and compared to those observed at other high altitude ground based sites, which performed experimental NPF studies providing an overall picture of the frequency of occurrence of the process and of some events features.

Chapter 1

Atmospheric aerosol

Atmospheric aerosol is a suspension of fine solid particles or liquid droplets in air, ubiquitously present in the Earth's atmosphere. The term aerosol commonly refers to aerosol particles.

Emitted directly as particles (primary aerosol) or formed in the atmosphere by gas-to-particle conversion processes (secondary aerosol), atmospheric aerosol particles range in size from a few nanometers (nm) to tens of micrometers (μm) in diameter. They play an important role influencing the energy balance of the Earth's system, visibility, climate, human health and environment as a whole. In spite of the great efforts made by the scientific community in the last decades, the atmospheric aerosol still presents unknowns due to its large variability and complexity in terms of sources, transport and transformation mechanisms, chemical composition, size distribution, global distribution and interaction with other components of the Earth's system.

This chapter summarizes the present knowledge on aerosols properties, impacts and new particle formation mechanisms in the atmosphere.

1.1 Aerosol life cycle

1.1.1 Sources and formation

A way to classify aerosol particles is based on their origin. Aerosol can originate from natural sources and anthropogenic sources (Boucher, 2015). Particles emitted from both natural and anthropogenic sources are given in Table 1.1.

Significant natural sources of particles include volcanic activity, wind-driven soil erosion processes, sea spry, biomass burning, and reactions between natural gaseous emissions.

Emissions of particulate matter attributable to the activities of humans arise primarily from four source categories: fuel combustion, industrial processes, nonindustrial fugitive sources (roadway dust from paved and unpaved roads, wind erosion of cropland, construction, etc.) and transportation sources (automobiles, etc.)
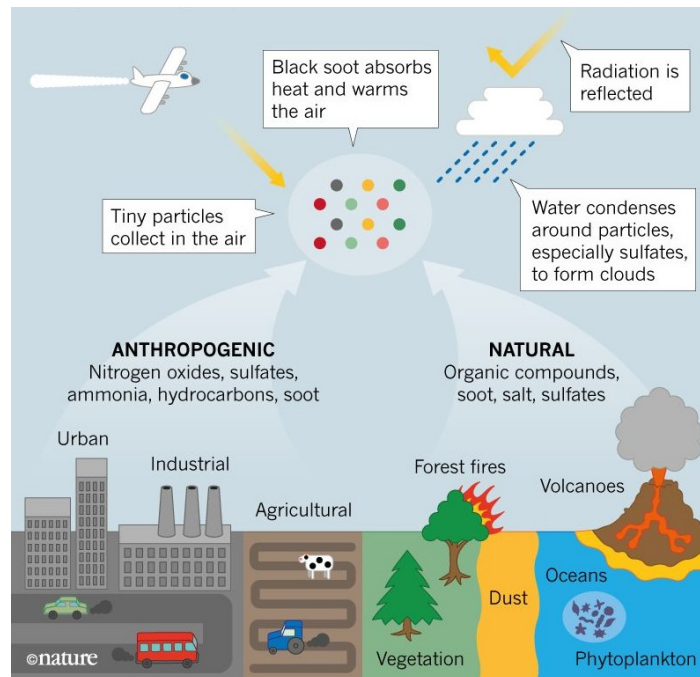
(Seinfeld and Pandis, 2016).

Figure 1.1: Diagram of the role and sources of atmospheric aerosols in the atmosphere, showing emmission processes and the action of aerosol while in the atmosphere (Penner, 2019).

Aerosols can also be classified according to their formation processes into two groups: primary aerosols and secondary aerosols.

Primary aerosols are particles emitted or injected directly into the atmosphere, and they can have both natural origins, like salt from the sea, dust from dry regions, or particles released by wildfires, and anthropogenic origins, like particulate resulting from fuel combustion, transport activities and industrial processes.

Secondary aerosols are particles formed via gas to particle conversion, in which condensable vapours lead either to growth of preexisting particles by condensation processes, or nucleation of new particles (Tomasi, Fuzzi, and Kokhanovsky, 2017). The phenomenon involving the nucleation of gas-phase atmospheric components into newly-formed particles, as well as their subsequent growth and coagulation, is called atmospheric new particle formation (NPF) (Kalkavouras et al., 2021). Such process is important since it represents the first step in the complex processes leading to formation of cloud condensation nuclei and it has a major influence on the radiative balance of the global climate system. NPF will be treated in details in Section 1.4 since it is a fundamental topic for the work that has been carried out in this thesis.

Source		Particle size (μm)	Emission (Tg/yr)
Natural			
Primary	Soil dust (mineral aerosols);	D<1	110
		D=1-2	290
		D=2-20	1750
	Sea to air flux of sea salt;	D<1	54
		D=1-16	3290
	Biogenic organic matter;	Coarse	1000
	Volcanic ash;	Fine	20
Secondary	Sulfate from aerosols from marine biogenic gases (mainly DMS);	Fine	16-32
	Sulfate from aerosols form terrestrial biogenic gases;	Fine	57
	Nitrate aerosols from NO_x (lightining, soil microbes);	Mainly coarse	3.9
	Organic matter from biogenic gases;	Fine	16
	Sulfate aerosols from volcanic SO_2;	Fine	9-21
Natural subtotals		**At least**	**6600**
Anthropogenic			
Primary	Aerosols from all kinds of fossil fuel burning, cement manufacturing, metallurgy, waste incineration, etc;	Coarse and fine	100
	Soot (black carbon) from fossil fuel burning (coal, oil);	Fine	8
	Soot from biomass burning;	Fine	5
	Biomass burning without soot;	Fine	80
Secondary	Sulfate from SO_2 (mainly from coal and oil burning);	Fine	140
	Nitrate aerosol from NO_x (fossil fuel and biomass combustion);	Mainly coarse	36
	Organic matter from anthropogenic gases;	Fine	5
	Organic matter from biomass burning;	Fine	54
	Organic matter from fossil fuel burning;	Fine	28
Anthropogenic subtotals			**460**
Total			**7100**

Table 1.1: Natural and anthropogenic sources of primary and secondary aerosols in global scale [based on Maenhaut, 1996; Raes et al., 2000; Mather et al., 2003; Jaenicke, 2005]. Adapted from (Wang, 2010).

1.1.2   Removal

The atmospheric life of aerosol particles emitted by the primary sources or formed from the precursor gases is schematically illustrated in Figure 1.2 and it is regulated by nucleation, coagulation, and condensation processes which will be explained in detail in Section 1.4. Subsequently, aerosol removal may occur through dry and wet deposition.
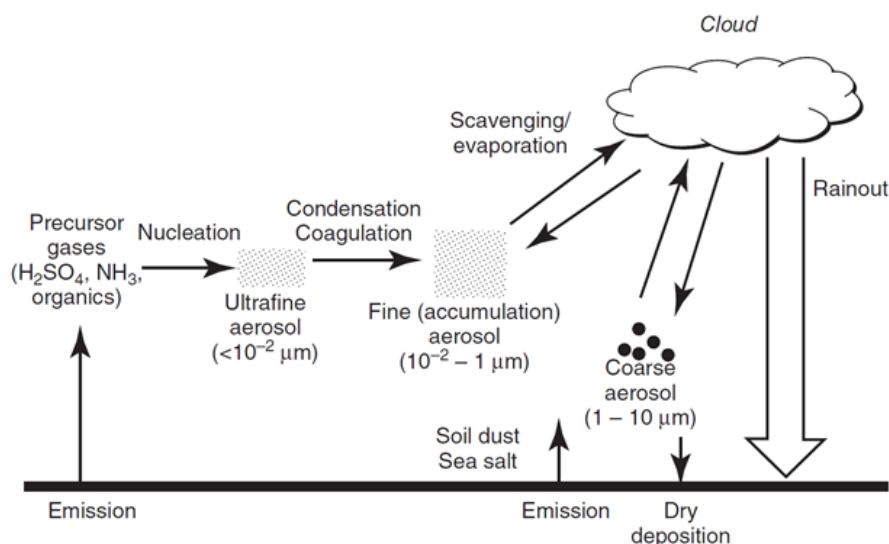

Figure 1.2: Schematic representation of the sequence of processes involving the atmospheric life of aerosol particles after the emission of the precursor gases, until their removal from the atmosphere through dry deposition and wet (rainout) mechanisms (Tomasi, Fuzzi, and Kokhanovsky, 2017).

The most important removal process for submicron aerosols is wet deposition, also called wet scavening (Xu et al., 2019), defined as the removal of any material from the atmosphere to the Earth's surface by the precipitation of liquid or frozen hydrometeorites. Arimoto et al. [1985] have measured a contribution of the aerosol wet deposition flux to the total deposition flux in the Pacific of 70 to 90% for trace elements, far from their source region. In a rural area, i.e., closer to source areas, Prakasa Rao et al. [1992] measured wet deposition flux contributions of 74 and 62% for sulfate and nitrate aerosols, respectively. In regions far from the sources, where the largest particles have already been removed by gravitational settling, this contribution has been estimated to be 60 to 85% for desert dust (Guelle et al., 1998). Two processes lead to wet deposition: the nucleation scavenging and the impaction scavenging. The former mechanism refers to aerosols (cloud condensation nuclei: CCN) inducing formation of cloud droplets in supersaturated water vapour and the latter mechanism refers to collision-coalescence of aerosols and water droplets. The impaction scavenging usually splits in two processes: in-cloud impaction scavenging, which treats the

interactions between cloud droplets and raindrops with interstitial aerosol particles (particles too small to nucleate to cloud droplets) and below cloud scavenging, which concerns the collection of aerosol particles by falling raindrops below the cloud base. The relative importance between in-cloud scavenging processes (nucleation and impaction scavenging), also called washout, and below cloud scavenging, also called rainout, depends on meteorological conditions and on the properties of aerosol particles (size distribution and chemical composition) as well as on the stage of cloud development (Berthet et al., 2010). Scavenged aerosols are irreversibly removed from the atmosphere if the water droplets gravitationally fall and reach the ground.

If wet deposition is an efficient sink for aerosols, it is of course conditional on the presence of precipitating clouds whose spatial and temporal distribution is very heterogeneous. Some regions experience very little precipitation while other regions exhibit very strong seasonal variations in precipitation (Boucher, 2015). In the absence of precipitation, the direct deposition of aerosols and aerosol precursors onto the Earth's surface, called dry deposition, becomes important. The relative importance of the removal effects by dry deposition depends on various factors, such as the atmospheric turbulence level, the chemical and water solubility characteristics of the particles, and surface and terrain characteristics. In fact, the level of turbulence governs the rate at which aerosols are delivered down to the surface, especially within the layer nearest to the ground, such a rate varying as a function of aerosol size, density, and morphological characteristics. The surface roughness constitute also a very important factor in dry deposition, since a smooth surface may lead to particle bounce-off, and canopies generally promote dry deposition (Tomasi, Fuzzi, and Kokhanovsky, 2017). Many investigators have chosen to represent the overall dry deposition process in terms of three simplified steps (Hosker Jr and Lindberg, 1982; Hicks et al., 1987). The first step is the aerodynamic transport by turbulent diffusion down through the atmospheric surface layer until to a very thin layer of stagnant air just adjacent to the surface. The second step is the Brownian transport across this thin stagnant layer of air until reaching the surface, called the quasi-laminar sublayer. Finally, the last step is the uptake of particles, which adhere to the surface, whose moisture and stickiness are important factors. Each of the steps can occur at a different rate; the slowest step generally determines the overall rate of dry deposition (Wu et al., 1992).

1.2 Physical and Chemical Aerosol Properties

1.2.1 Morphology and size characterization

Particulate matter is commonly characterized by its size. The latter can be defined as geometric or physical diameter (d_p) at the simplest level. If the particle is spherical the meaning of this parameter is obvious, otherwise it does not have a precise meaning and atmospheric aerosol particles are often nonspherical (DeCarlo et al., 2004). In fact, atmospheric particles can be characterised by various shapes: from the rough-edge shape of a crustal particle in Figure 1.3a, to the long branched chains of small nanoparticles characterizing Diesel exhausts emission in Figure 1.3b, to the flat appearance of a skin fragment in Figure 1.3c, to the cubic shape of a sodium chloride crystal in Figure 1.3d (Perrino, 2010).
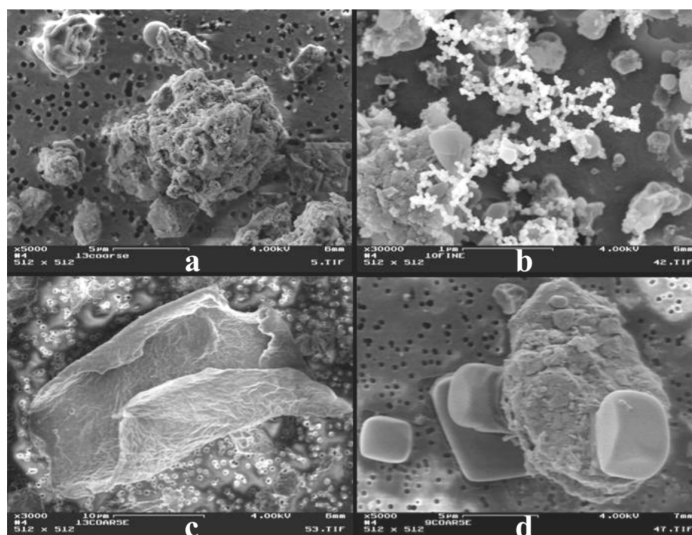

Figure 1.3: Shapes of atmospheric particles. Photos by courtesy of
Prof. Y. Mamane, Technion, Haifa (Israel) (Perrino, 2010).

Nonspherical particles are generally characterized by equivalent diameters, defined as the diameter of a sphere, which with a given instrument would yield the same size measurement as the particle under consideration (DeCarlo et al., 2004). For exemple, the equivalent volume diameter (d_e) is defined as the diameter of a sphere of the same volume as that of the irregular particle. Also commonly used is the aerodynamic diameter (d_a). This is defined as the diameter of a spherical particle with unit density which has the same settling velocity as the particle in question (Baron and Willeke, 2001). Aerodynamic diameter is useful for characterising particles with significant inertia, which are typically particles larger than $0.5 \mu m$. Smaller particles undergo Brownian motion and diffusion diameter is used for them. Diffusion diameter is defined as the diameter of a spherical particle with density of unity which has the

same diffusion as the particle in question (Salimi, 2014). However, for the aim of the thesis it is fundamental to introduce the electrical mobility diameter (Dp), since all the data analyzed in the present work were obtained by a Differential Mobility Particle Sizer (DMPS) which classifies charged particles according to their mobility in an electric field. The instrument will be described in detail in Chapter 2. Electrical mobility diameter is defined as the diameter of a spherical particle with unit density which has the same electrical mobility (Z_p) as the particle in question (Flagan, 2001). The behavior of a particle in an electric field is deepened in Section 1.3.3, where the equation of the electric mobility is derived. The equation of the electrical mobility diameter is the following:

$$Dp = \frac{neC_c}{3\pi\eta Z_p} \tag{1.1}$$

where n is the number of excess elementary charges e carried by the particle, η is the viscosity of air and C_c is the Cunningham slip corrector factor (Kulmala et al., 2012). For spherical particles, Dp equals d_p and d_e (DeCarlo et al., 2004).

1.2.2   Ultrafine, Fine and Coarse Modes

Taking into account the size characterization explained in the previous paragraph, this chapter assumes spherical aerosols of a known diameter Dp and density ρ_p, in order to provide a single coherent mathematical description of the particles. Aerosol sizes span several orders of magnitude, from a few nanometers for new particles produced by nucleation, to several hundred micrometers for the largest particles produced by the wind friction on the land and the ocean surface (Boucher, 2015). Particles less than $2.5\mu m$ in diameter are generally referred to as *fine* and those greater than $2.5\mu m$ diameter as *coarse* (Seinfeld and Pandis, 2016).

Fine and coarse particles differ in sources, formation mechanisms, composition, atmospheric lifetimes, spatial distribution, indoor–outdoor ratios, and temporal variability. Therefore the distinction between fine and coarse particulate matter is a fundamental one in any discussion of the physics, chemistry, measurement, or health effects of aerosols.

Fine particles can be divided roughly into three modes: the nucleation mode with a particle diameter $Dp < 25nm$ (also called the ultrafine mode), the Aitken mode $25nm < Dp < 100nm$ (named after the Scottish meteorologist and physicist John Aitken), the accumulation mode $100nm < Dp < 2,5\mu m$. The nucleation particles mainly form through condensation of hot vapors during combustion processes and/or nucleation of atmospheric gaseous species to form fresh particles and they are lost principally by coagulation with larger particles.

The accumulation mode is so named because mass accumulates in this size range by coagulation of particles in the nuclei mode and condensation of vapors onto existing

particles.

The coarse mode is formed by mechanical processes and usually consists of man-made and natural dust particles. A supercoarse mode can be found close to the source point but is generally absent in more aged aerosol populations.

1.2.3 Size Distribution

The size of aerosol particles affects both their lifetime in the atmosphere and their physical and chemical properties (Seinfeld and Pandis, 2016). It is therefore necessary to develop methods of mathematically characterizing aerosol size distributions. A measured distribution of particle sizes can be described by a histogram of the number of particles per unit volume within defined size bins. By making the bin sizes tend to zero a continuous function is formed called the diameter number density distribution $N(Dp)$ which represents the number of particles with diameters between Dp and $Dp + \Delta Dp$ per unit volume. The differential diameter number density distribution $n_N(Dp)$ is defined by

$$n_N(Dp) = \frac{dN(Dp)}{dDp}.$$
(1.2)

The same equation can be written in integral form as

$$dN(Dp) = \int_{Dp}^{Dp+\Delta Dp} n_N(Dp)dDp.$$
(1.3)

The total number of particles per unit volume N is given by

$$N = \int_{0}^{\infty} n_N(Dp)dDp.$$
(1.4)

Several aerosol properties depend on the particle surface area and volume distributions with respect to particle size. So it is important to define the aerosol surface area distribution as

$$n_S(Dp) = \pi Dp^2 n_N(Dp)$$
(1.5)

and the aerosol volume distribution

$$n_V(Dp) = \frac{\pi}{6} Dp^3 n_N(Dp).$$
(1.6)

The observed aerosol distribution is fitted reasonably well by log-normal distribution, the most useful in situations where the distributed quantity can have only positive values and covers a wide range of values. Therefore, atmospheric aerosol size

distributions can be described as the sum of n log-normal distributions

$$n_N(logDp) = \sum_{i=1}^{n} \frac{N_{0,i}}{\sqrt{2\pi}log\sigma_{g,i}} exp\left(-\frac{1}{2}\frac{(logDp - log\overline{D}_{pg,i})^2}{log^2\sigma_{g,i}}\right) \qquad (1.7)$$

where $N_{0,i}$ is the integral of the i_{th} lognormal function, $\overline{D}_{pg,i}$ is the mean geometric diameter, and $\sigma_{g,i}$ is the geometric standard deviation of the ith log-normal mode.
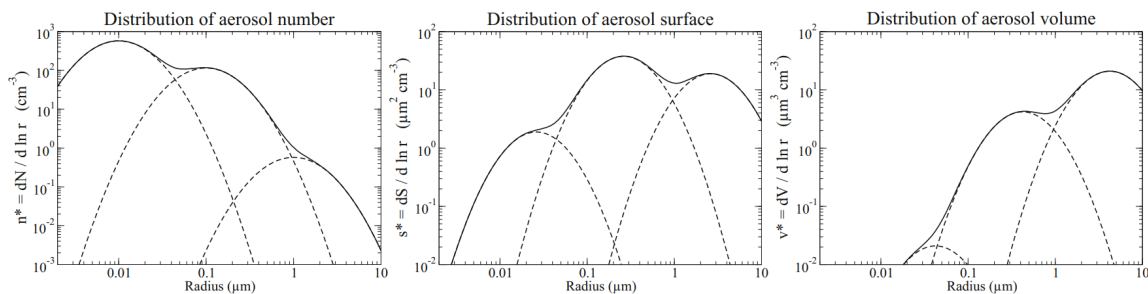

Figure 1.4: Schematic of the three modes of the aerosol size distribution (Boucher, 2015).

Figure 2.9 shows the superposition of three log-normal distributions with mean geometric number radius r_g of 0.01, 0.1 and $1\mu m$, geometric standard deviation σ_g of 2 and with total concentrations of 1000, 200 and $1cm^{-1}$, respectively. This illustration shows how the fine mode dominates the aerosol number distribution, while the accumulation mode dominates the aerosol surface distribution and the coarse mode dominates the aerosol volume. The ultrafine and supercoarse modes that may also exist are not represented in this schematic.

1.2.4 Chemical composition

The chemical composition affects aerosol properties like radiative effects, hygroscopic growth, reactivity, ability to form cloud droplets, and, consequently, their effects on the environment, from visibility impairment to effects on human health and from effects on the biosphere to material deterioration and to climate change (Tomasi, Fuzzi, and Kokhanovsky, 2017).

Primary aerosol

Primary aerosols are atmospheric particles that are emitted directly into the atmosphere and consist of both inorganic and organic components. Inorganic primary aerosols are relatively large (often larger than $1\mu m$) and originate from sea spray, mineral dust, and volcanoes. Primary organic aerosols (POA) sources include biomass/fossil fuel combustion, higher plants and soil dust. Some examples of POA are primary biological aerosol particles (PBAPs) such as pollen, spores, bacteria, plant and

animal fragments. These coarse aerosols have short atmospheric lifetimes, typically only a few days.

Secondary aerosol

Secondary aerosols are mainly composed by sulfate, nitrate, ammonium ions and secondary organic carbon, especially in the finest fractions. The secondary aerosols concentration depends on concentrations of precursor gasses or other reactive gaseous species, such as O_3 and radical OH, and on atmospheric conditions.

Sulfate aerosols are a suspension of fine solid particles of a sulfate (SO_4^{2-}) or tiny droplets of a solution of a sulfate or of sulfuric acid (hydrogen sulfate). They are produced by chemical reactions in the atmosphere from gaseous precursors, with the exception of sea salt sulfate and gypsum dust particles. The two main sulfuric acid precursors are sulfur dioxide (SO_2) from anthropogenic sources and volcanoes, and dimethyl sulfide (DMS) from biogenic sources, especially marine phytoplankton.

Ammonium (NH_4^+) is the principle cation associated with fine sulfate and fine nitrate in the continental aerosol. Ammonia (NH_3) is released by natual soils, coal combustion, biomass burning, fertilizer application and production or is emitted as a result of the decay of waste products from domestic animals, wild animals, seas and oceans (Wang, 2010).

Nitrate (NO_3^-) is often found in both fine and coarse atmospheric aerosol particles. Nitrate in fine particles is produced from the reaction of gas-phase nitrate (nitric acid; HNO_3) and ammonia (NH_3) (Kim, 2019). Nitrate in coarse particles comes primarily from the reaction of gas-phase nitric acid with pre-existing coarse particles. Typical sources of nitric oxides are fossil fuel combustion, soils, biomass burning and lightning.

Secondary organic aerosols (SOA) components are formed by chemical reaction and gas-to-particle conversion of volatile organic compounds ($VOCs$). Formation of $VOCs$ from the gas phase can be both natural and anthropogenic. The main natural compounds are isoprene, monoterpenes and sesquiterpenes while the main anthropogenic are aromatics, alkanes and alkenes. The SOA formation can then be due to nucleation and growth of aerosol particles, adsorption and absorption of $VOCs$ by preexisting aerosols or cloud particles, heterogeneous and multi-phase chemical reaction of $VOCs$ or semi-volatile organic compounds ($SVOC$), at the surface or in the bulk of aerosol or cloud particles. There are still many uncertainties in emission and processes involving POA and SOA, which reflects in a lack of knowledge about their concentration and role in the climate system (Renzi, 2019).

Geographic Distibution

Long-term aerosol mass concentrations are measured systematically at the surface by global and regional networks. A survey of the main aerosol types can be constructed from such measurements. Figure 1.5, taken from the IPCC report Climate Change 2013, shows bar chart plots summarizing the mass concentration ($\mu g m^{-3}$) of seven major aerosol components for particles with diameter smaller than $10 \mu m$, from various rural and urban sites in six continental areas of the world with at least an entire year of data and two marine sites. Mineral dust dominates the aerosol mass over some continental regions with relatively higher concentrations especially in urban South Asia and China. In the urban North America and South America, organic carbon (OC) contributes the largest mass fraction to the atmospheric aerosol, while in other areas of the world the OC fraction ranks second or third. Sulfate is an important component of the inorganic fraction of the aerosol, and is systematically accompanied by ammonium. Nitrate can be present in very variable quantities but concentrations decrease rapidly outside source regions. Sea salt can be dominant at oceanic remote sites with 50 to 70% of aerosol mass (IPCC 2013).
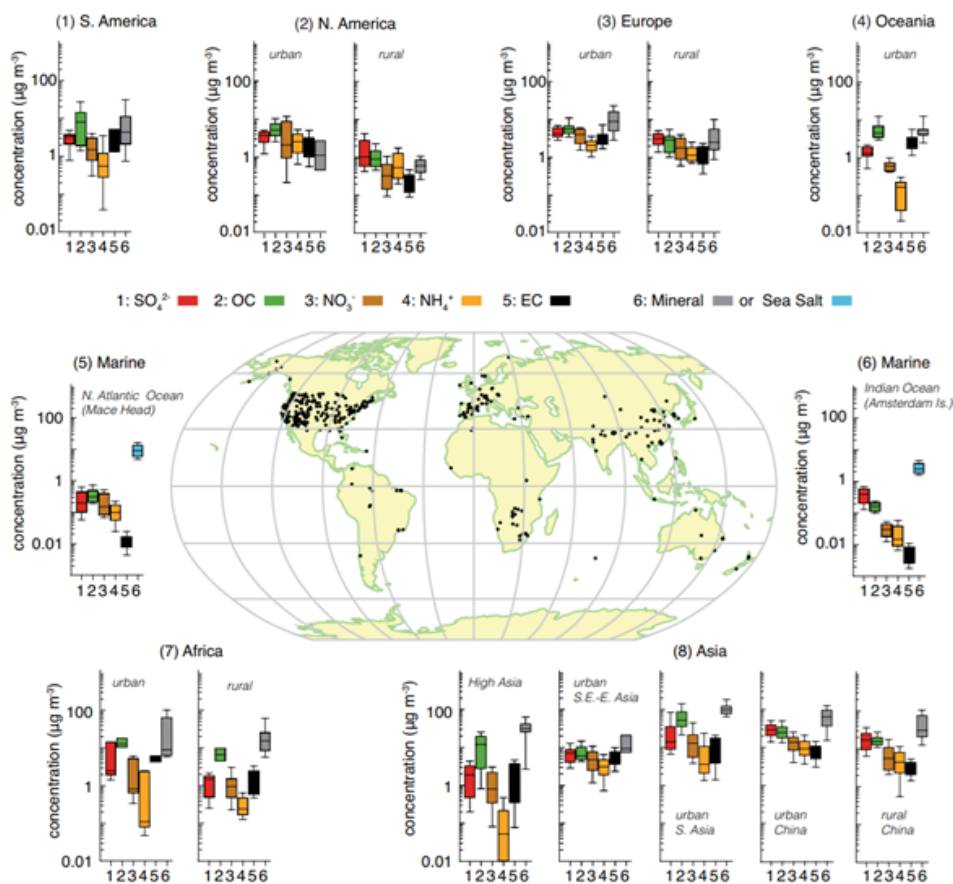

Figure 1.5: Climatology of the mass concentrations ($\mu g m^{-3}$) of seven major chemical species of the atmospheric aerosol in different regions of the world. Reproduced from Boucher, 2015. (© IPCC)

1.3   Electrical Properties

In aerosol mechanics, the most important electrostatic effect is the force exerted on a charged particle in an electrostatic field (Hinds, 1999). Most aerosol particles carry some electric charge since they are formed, but they can also be charged during their life cycle or, artificially, using specific tools, like particle charger, where ions are mixed with the aerosol sample. This is a fundamental property because the motion induced by electrostatic forces forms the basis for important type of air-cleaning equipment and aerosol sampling and measuring instruments. Indeed, all the data analyzed for the present thesis where collected using a Differential Mobility Particle Sizer (DMPS), described in detail in Chapter 2. The DMPS operating principle is based on the charging of collected particulate through a particle charger and the application of an electric field in order to classify charged particles according to their electrical mobility. In this section some charging mechanism observable in nature by which particle acquire charge are described. Among them, the *diffusion charging* mechanism is exploited by the Neutralizer, described in 2.2.2, which is part of the Differential Mobility Particle Sizer used at Mt. Cimone. Then, the definition of the so called *Boltzmann equilibrium* of charge distribution is given and the concept of the electric mobility, already introduced in Section 1.2.1, is examined more closely.

1.3.1   Charging mechanism

The principal mechanisms by which aerosol particles acquire charge are flame charging, static electrification, field charging, and diffusion charging. The last two require the production of unipolar ions and are used to produce highly charged aerosols. Most of the information of this paragraph is taken from (Hinds, 1999).

Flame charging occurs when particles are formed in or pass through a flame. At the high temperature of the flame, direct ionization of gas molecules creates high concentrations of positive and negative ions and thermionic emissions of electrons or ions from particles. Indeed, flames generate large numbers of ions and charged clusters with concentrations as high as $10^{10}/cm^3$ (Wang et al., 2017). The highly concentrated ions and charged clusters actively collide with the formed nanoparticles, adding electrostatic potentials to the system, and further altering the properties of the generated particles, such as their size, shape, and crystallinity (Zhang et al., 2012).

Static electrification causes particles to become charged by mechanical action as they are separated from the bulk material or other surfaces. Particles are usually charged by static electrification during their formation, resuspension, or high-velocity transport. The three primary mechanisms of static electrification that can charge aerosol particles during their generation are electrolytic charging, when a liquids

with a high-dielectric constant are separated from solid surfaces, spray electrification, when the surface of some liquids is disrupted during the formation of droplets by atomization or bubbling, and contact charging, when a particle contacts a surface, charge is transferred between the particle and the surface.

Field charging is charging by unipolar ions in the presence of a strong electric field. This mechanism is depicted in Figure 1.6, in which the negatively charged plate is at the left and negative ions are present. When an uncharged spherical particle is placed in a uniform electric field, it distorts the field, as shown in Figure 1.6a. The field lines shown represent the trajectories of ions. For an uncharged particle, the greater the value of ϵ, the greater the number of field lines that converge on the particle. Ions in this electric field travel along the field lines and collide with the particle where the field lines intersect the particle and transfer their charge to it. As the particle becomes charged, it will tend to repel the like-charged incoming ions, as shown in Figure 1.6b. The rate of ions reaching the particle decreases as the particle becomes charged. Ultimately, the charge builds up to the point where no incoming field lines converge on the particle, as in Figure 1.6c, and no ions can reach the particle. At this maximum-charge condition, the particle is said to be at saturation charge.
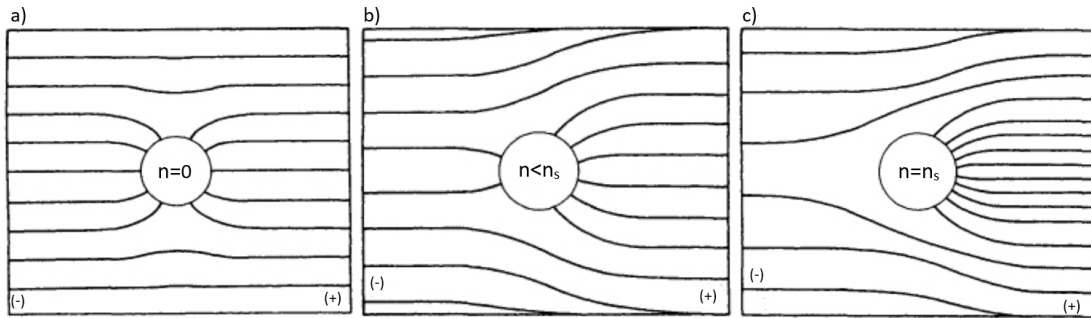

Figure 1.6: Electric field lines for a conductiong particle in a uniform field with a negative plate at left. a) An uncharged particle. b) A partially charged particle. c) A particle at saturation charge. (Hinds, 1999).

According to Hinds, 1999, the number of charges, n_{field}, acquired by a spherical particle of diameter D_p during a time t in an electric field E_c with an ion number concentration N_i is

$$n_{field}(t) = \left(\frac{3\epsilon}{\epsilon + 2}\right)\left(\frac{E_c \pi \epsilon_0 D_p^2}{e}\right)\left(\frac{\pi e Z_i N_i t}{4\pi\epsilon_0 + \pi e Z_i N_i t}\right) \tag{1.8}$$

where Z_i is the electric mobility of ions and ϵ_0 is the permittivity of the vacuum. In this equation the first two factors represent the saturation charge n_s reached after sufficient time at a given charging condition:

$$n_s = \left(\frac{3\epsilon}{\epsilon + 2}\right)\left(\frac{E_c \pi \epsilon_0 D_p^2}{e}\right) \tag{1.9}$$

The rate of charging does not depend on the particle size or field strength, but only on the ion concentration. When particles are intentionally charged by field charging, the ion concentration is usually $10^7/cm^3$ or greater, so charging will be 95% complete in 3 s or less.

Finally, particles mixed with ions become charged by random collisions between the ions and the particles. This process is called *diffusion charging* because the collisions result from the Brownian motion of the ions and particles. This mechanism does not require an external electrical field and, to a first approximation, does not depend on the particle material. As the charge accumulates, it produces a field that tends to repel additional ions, reducing the charging rate. The ions, being in equilibrium with the gas molecules, have a Boltzmann distribution of velocities. As the charge on the particle increases, fewer and fewer ions have sufficient velocity to overcome the repulsive force, and the charging rate slowly approaches zero. It never reaches zero, however, because the Boltzmann distribution of velocities has no upper limit. An approximate expression taken from Hinds, 1999, for the number of charges $n_{diff}(t)$ acquired by a spherical particle of diameter D_p by diffusion charging during a time t is

$$n_{diff}(t) = \frac{2\pi\epsilon_0 D_p kT}{e^2} ln\left(1 + \frac{D_p c_i e^2 N_i t}{8\epsilon_0 kT}\right) \qquad (1.10)$$

where ϵ_0 is the permittivity of the vacuum, k is the Boltzmann constant, T is the temperature, e is the charge of the elementary charge, c_i is the mean thermal velocity of the ions and N_i is their concentration. Although theoretical charging equations, such as the above, are usually valid for spherical particles only, the particle diameter is often substituted by mobility equivalent diameter. Even in the presence of an electrostatic field, diffusion charging is the predominant mechanism for charging particles less than $0.2\mu m$ in diameter (Hinds, 1999).

1.3.2 Equilibrium charge distribution

Uncharged particles are rare because of random collisions with the omnipresent air ions. Indeed, every cubic centimeter of air contains about 10^3 ions with approximately equal numbers of positive and negative ions (Epa, 2004). Aerosol particles that are initially neutral will acquire charge by collision with ions due to their random thermal motion. Aerosol particles that are initially charged will lose their charge slowly as the charged particles attract oppositely charged ions. These competing processes eventually lead to an equilibrium charge state called the *Boltzmann equilibrium charge distribution*. The latter represents the charge distribution of an aerosol in charge equilibrium with bipolar ions. For equal concentrations of positive and negative ions, a reasonable first approximation for normal air, the fraction of particles f_n of a given size having n

positive (or n negative) elementary units of charge is given by

$$f_n = \frac{exp(K_E n^2 e^2 / D_p kT)}{\sum_{n=-\infty}^{\infty} exp(K_E n^2 e^2 / D_p kT)} \tag{1.11}$$

where $K_E = \frac{1}{4\pi\epsilon_0}$ is the Coulomb's constant equal to $9.0 \cdot 10^9 N \cdot m^2 / C^2$. For particle diameters D_p larger than $0.01 \mu m$, over 99% of the particles carry no charges when they are at the Boltzmann equilibrium charge distribution. The percentage of uncharghed particles drops to 42.6% for $0.1 \mu m$ particles, 13.5% for $1 \mu m$ particles, and 4.3% for $10 \mu m$ particles (Wang, 2005).

1.3.3   Motion of a particle in an external field

To derive the equation of motion for a particle of mass m_p, let us begin with a force balance on the particle, which we write in vector form as

$$m_p \frac{d\boldsymbol{v}}{dt} = \sum_i \boldsymbol{F_i} \tag{1.12}$$

As long as the particle is not moving in a vacuum, the drag force will always be present, so let us isolate the drag force from the summation of forces

$$m_p \frac{d\boldsymbol{v}}{dt} = \frac{3\pi\mu D_p}{C_c}(\boldsymbol{u} - \boldsymbol{v}) + \sum_i \boldsymbol{F_{ei}} \tag{1.13}$$

where $\boldsymbol{F_{ei}}$ denotes external force i (those force arising from external potential fields, such as gravity and electrical forces) and C_c is the Cunningham slip corrector factor. If a particle has an electric charge q in an electric field of strength $\boldsymbol{E}$, an electrostatic force $\boldsymbol{F_{ee}} = q\boldsymbol{E}$ acts on the particle. The equation of motion for a particle of charge q moving at velocity $\boldsymbol{v}$ in a fluid with velocity $\boldsymbol{u}$ in the presence of an electric field of strength $\boldsymbol{E}$ is

$$m_p \frac{d\boldsymbol{v}}{dt} = \frac{3\pi\mu D_p}{C_c}(\boldsymbol{u} - \boldsymbol{v}) + q\boldsymbol{E} \tag{1.14}$$

At steady state in the absence of a background fluid velocity, the particle velocity is such that the electrical force is balanced by

$$\boldsymbol{v_e} = \frac{qC_c}{3\pi\mu D_p}\boldsymbol{E} \tag{1.15}$$

where $\boldsymbol{v_e}$ is termed the *electrical migration velocity*. Finally, we can define the *electrical mobility* of a charged particle Z_p as

$$Z_p = \frac{neC_c}{3\pi\eta D_p} \tag{1.16}$$

The electrical mobility of a particle is defined as the ratio of the constant limiting velocity a charged particle will reach in a uniform electric field to the magnitude of this field (Kulkarni, Baron, and Willeke, 2011).

1.4 Impacts

1.4.1 Climate effects

One of the driving reasons for the analysis provided in this thesis is the important role aerosol particles play in the climate system. The new terminologies adopted in this paragraph can be found in the Fifth Assessment Report (AR5) of the Intergovernmental Panel on Climate Change. Indeed, the IPCC report of 2013 pointed out the importance of distinguishing between the traditional concept of radiative forcing (RF) and the relatively new concept of effective radiative forcing (ERF) that also includes rapid adjustments. In the next paragraph the concept of rapid adjustment is analysed more in detail. RF, in units of Wm^{-2}, is defined, as it was in the Fourth Assessment Report AR4 of 2007, as the instantaneous perturbation in net radiative flux at the tropopause exerted by a change in a component of the radiative budget, with surface temperature and tropospheric state maintained in their unperturbed state. By convention, negative RFs denote a decrease in net radiative flux, or a loss of energy from the climate system. Conversely, positive RFs denote a gain of energy to the climate system. ERF represents the change in net downward radiative flux at the top of the atmosphere after allowing for atmospheric temperatures, water vapour and clouds to adjust, but with global mean surface temperature or a portion of surface conditions unchanged. So, ERF is the sum of RF and its fast adjustments, and it is a better predictor of the subsequent long-term change in surface temperature than instantaneous RF (Bellouin, 2014).

Forcing, Rapid Adjustments and Feedbacks

Aerosols can be defined as *forcing agents*, which are elements of the climate system with the ability to influence the global mean surface temperature by acting on the Earth's energy balance. This action can be direct or driven by *rapid adjustaments*. The latter, sometimes called rapid responses, arise when forcing agents, by altering flows of energy internal to the system, affect cloud cover or other components of the climate system and thereby alter the global budget indirectly. Adjustments can occur through geographic temperature variations, lapse rate changes, cloud changes and vegetation effects. These adjustments are generally very quick and do not operate through changes in surface temperature, that are slowed by the ocean's heat capacity. The effect on climate of forcing agents can then be amplified or decreased through *feedback mechanisms*

or changes in climatic variables mediated by a variation in the global mean surface temperature which impact on radiative budget. For aerosols, the IPCC report of 2013 distinguishes forcing processes arising from aerosol–radiation interactions (ari), and aerosol–cloud interactions (aci), whose global impact are respectively defined as Effective Radiative Forcing from aerosol-radiation interaction (ERFari) and Effective Radiative Forcing from aerosolcloud interaction (ERFaci). Both these components of the change are divided into Radiative Forcing and adjustments as in Figure 1.7. The blue arrows depict solar radiation, the grey arrows terrestrial radiation and the brown arrow symbolizes the importance of couplings between the surface and the cloud layer for rapid adjustments.
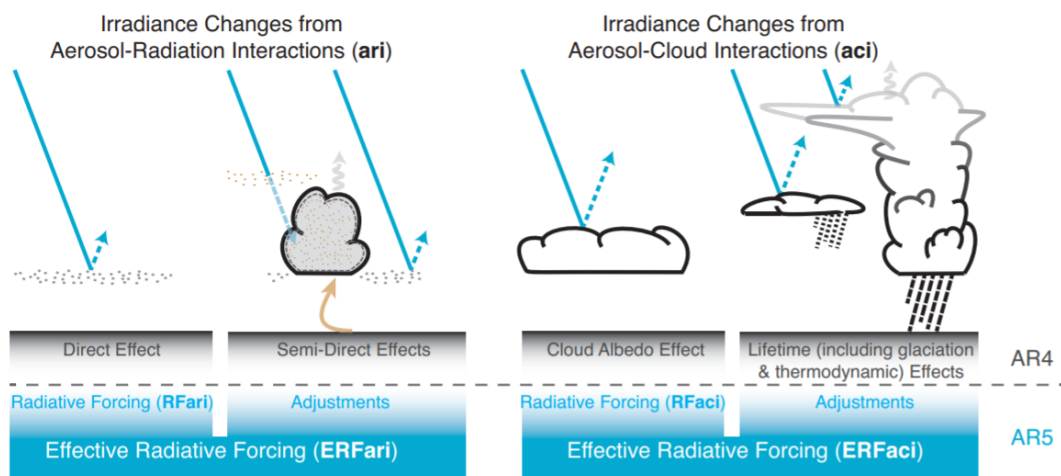
Figure 1.7: Schematic of the new terminology used in the Fifth Assessment Report (AR5) for aerosol–radiation and aerosol–cloud interactions and how they relate to the terminology used in Fourth Assessment Report AR4.

Aerosol–Radiation Interactions

The radiative effect due to aerosol–radiation interactions (RFari), formerly known as direct radiative effect, is the change in radiative flux caused by the combined scattering and absorption of radiation by anthropogenic and natural aerosols. A schematic representation of the aerosol radiation interaction is shown in Figure 1.8. Aerosols increase the reflection of solar radiation back to the space through various radiative and physical processes. Moreover, a small fraction of them is also capable of heating the lower atmosphere when they contain energy absorbers likely elemental carbon and mineral dust. RFari depends on the horizontal and vertical distributions of aerosol concentrations and scattering and absorption properties, which in turn depend on aerosol sizes and chemical composition. Environmental factors, such as the solar zenith angle, and the reflectance of the surface or cloud underlying the aerosol layer, also play important roles. Approximate formulas to quantify RFari at the Top of the

Atmosphere in cloud-free sky have been derived, such as the following (Bellouin, 2014), which is valid for both scattering and absorbing aerosols:

$$RFari \sim ST^2\overline{\omega_0}\beta\Delta\tau[(1 - R_s)^2 - 2R_s(1 - \overline{\omega_0}/(\beta\overline{\omega_0}))] \tag{1.17}$$

where S is the solar constant, in Wm^{-2}, T is the dimensionless transmittance of the atmosphere above the aerosol layer, and R_s is the dimensionless reflectance of the surface. Aerosols are characterized by three dimensionless parameters: the change in optical thickness, $\Delta\tau$; the single scattering albedo $\overline{\omega_0}$; the upscatter fraction, β, which quantifies the fraction of radiation that is scattered upward with respect to the particle's horizontal plan. Equation 1.17 highlights the fact that the sign of RFari depends on the aerosol absorption properties and the reflectance of the surface. It also shows that for a given set of optical properties, RFari depends linearly on the change in aerosol optical thickness or, equivalently, aerosol concentrations.
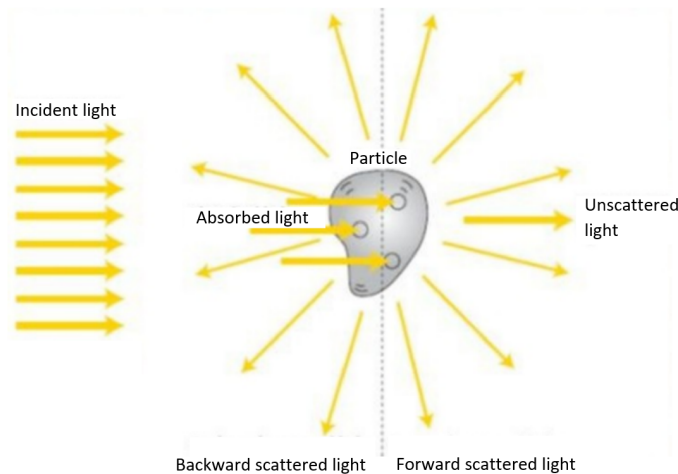
Figure 1.8: Schematic representation of scattering and absorption by a single particle.

Aerosol–radiation interactions give rise to rapid adjustments, which are particularly pronounced for absorbing aerosols such as BC. Indeed, aerosols that are highly absorbing of solar radiation may reduce cloud cover and liquid water content by heating the cloud and the environment within which the cloud forms. This is known as the semi-direct effect (Hansen, Sato, and Ruedy, 1997) because it is the result of direct interaction of aerosols with radiation but also influences climate indirectly by altering clouds.

Aerosol–Cloud Interactions

The radiative forcing due to aerosol–cloud interactions (RFaci), termed alternatively aerosol first indirect RF, cloud albedo forcing, or Twomey forcing in the scientific

literature, arises from the role aerosols play in the hydrological cycle as cloud condensation nuclei. Cloud droplets are formed by the condensation of water on already existing aerosol particles called cloud condensation nuclei (CCN). The presence of suitable particles in the air greatly reduces the supersaturation needed to form water droplets and hence clouds. The ability of a particle to act as a nucleus for water droplet formation (i.e., to become activated as a CCN) depends on size, chemical composition, and the local supersaturation. Hygroscopic materials such as sulfates and sea salts are especially efficient as CCN; mineral dust and combustion products can also be effective, especially if they are wet or have hygroscopic coatings. Organic substances have also been recognised as active cloud condensation and ice formation nuclei. Increased numbers of CCNs, recognised by several studies summarized in the IPCC report (2007), lead to more cloud droplets and a concurrent decrease in droplet sizes and it is called Twomey effect. The non-linear relationship derived in Feingold and Graham, 2003, between the concentrations in number of aerosols and raindrops is as follows:

$$N_d \sim (N_a)^b \tag{1.18}$$

where N_d is the drop concentration, N_a is the total particle concentration and b can vary widely, with values ranging from 0.06 to 0.48 (low values of b correspond to low hygroscopicity), because of the great sensitivity to the characteristics of the aerosol. An approximate formula for the computation of RFaci proposed by Bellouin et al. (2014) is:

$$RFaci \sim -S \cdot f \cdot \frac{\delta \alpha}{\delta N_d} \cdot \frac{\delta N_d}{\delta N_a} \cdot dN_a \tag{1.19}$$

where S is the solar constant, f is the fractional cloud cover, δN_a is the change in cloud condensation nuclei due to anthropogenic activities, $\delta N_d / \delta N_a$ is the sensitivity of cloud droplet number, N_d, to a change in cloud condensation nuclei, and $\delta \alpha / \delta N_d$ is the susceptibility of cloud albedo, α, to a change in cloud droplet number.

Efforts to understand the other component of the ERFaci, cloud adjustments, have been similarly clouded in uncertainty (Douglas and L'Ecuyer, 2020) and are associated with both albedo and so-called lifetime effects. Because of multiple light scattering within the cloud, the cloud albedo tends to increase with increased numbers of CCN. In addition, models have shown that aerosol affects the distribution of liquid throughout the cloud and vertical motion within the cloud, greatly perturbing the cloud's lifetime, precipitation, and extent (Ramanathan et al., 2001). Aerosol can act to increase the lifetime of clouds through delayed collision coalescence, or decrease the lifetime through evaporation-entrainment (Small et al., 2009). The cloud adjustment response depends on the cloud state and a sequence of reactions dictated by the environment (Gryspeerdt et al., 2019). Indeed, observational evidence for fast adjustments is mixed, with observations showing either a reduction or enhancement of precipitation in regions

with high anthropogenic aerosol loading, depending on cloud regime. For example, aerosol-driven fast adjustments are unlikely to influence those clouds whose lifetime is not regulated by precipitation, such as nonprecipitating stratocumulus clouds. At the other end of the precipitation spectrum, clouds where accretion of raindrops dominates over autoconversion (the initial stage of the collision–coalescence process whereby cloud droplets collide and coalesce to form drizzle drops) are also not likely to be influenced by aerosol-driven changes in cloud droplet size distribution. Aerosol fast adjustments would then be limited to specific cloud regimes, or to situations where increases in cloud condensation nuclei forces a change in cloud regime, such as the transition from open to closed-cells cumulus clouds (Bellouin, 2014).

Summary of Effective Radiative Forcing

The quantification of interactions in the cloud-aerosol-radiation system remains elusive and the recent IPCC report stresses that aerosol climate impacts remain the largest uncertainty in driving climate change. The table reported in Figure 1.9 has an overview of the RF agents considered in the previous paragraphs and each of them is given a confidence level for the change in RF over the Industrial Era to 2011. The confidence level is based on the evidence (robust, medium, and limited) and the agreement (high, medium, and low) as given in the table. The basis for the confidence level and change since AR4 is provided. Note that the confidence level for aerosol–cloud interactions includes rapid adjustments. For aerosol–radiation interaction the table provides separate confidence levels for RF due to aerosol–radiation interaction and rapid adjustment associated with aerosol–radiation interaction.

	Evidence	Agreement	Confidence Level	Basis for Uncertainty Estimates (more certain / less certain)	Change in Under-standing Since AR4
Aerosol–radiation interactions	Robust	Medium	*High*	A large set of observations and converging independent estimates of RF/Differences between model estimates of RF	Elevated owing to more robust estimates from independent methods
Aerosol–cloud interactions	Medium	Low	*Low*	Variety of different observational evidence and modelling activities/ Spread in model estimates of ERF and differences between observations and model results	ERF in AR5 has a similar confidence level to RF in AR4
Rapid adjustment aerosol–radiation interactions	Medium	Low	*Low*	Observational evidence combined with results from different types of models/Large spread in model estimates	Elevated owing to increased evidence
Total aerosol effect	Medium	Medium	*Medium*	A large set of observations and model results, independent methods to derive ERF estimates/Aerosol–cloud interaction processes and anthropogenic fraction of CCN still fairly uncertain	Not provided previously

Figure 1.9: Confidence level for the forcing estimate associated with each forcing agent for the 1750–2011 period (Adapted from IPCC 2013.

In the IPCC report of 2013, the ERF due to aerosol–radiation interactions that takes rapid adjustments into account (ERFari) is assessed to be $-0.45 \pm 0.5 Wm^{-2}$. The

uncertainty estimate is wider but more robust, based on multiple lines of evidence from models, remotely sensed data, and ground-based measurements. The total ERF due to aerosols (ERFari+aci, excluding the effect of absorbing aerosol on snow and ice) is assessed to be be $-0.9Wm^{-2}$ with a 5 to 95% uncertainty range of -1.9 to $-0.1Wm^{-2}$ (medium confidence), and a likely range of -1.5 to $-0.4Wm^{-2}$. This range was obtained from expert judgement guided by climate models that include aerosol effects on mixed-phase and convective clouds in addition to liquid clouds, satellite studies and models that allow cloud-scale responses.

1.4.2 Health effects

Numerous epidemiological studies show that fine air particulate matter and traffic-related air pollution are correlated with severe health effects, including enhanced mortality, cardiovascular, respiratory, and allergic diseases (Bernstein et al., 2004). Moreover, toxicological investigations in vivo and in vitro have demonstrated substantial pulmonary toxicity of model and real environmental aerosol particles, but the biochemical mechanisms and molecular processes that cause the toxicological effects such as oxidative stress and inflammatory response have not yet been resolved. Epidemiological studies usually refer to PM mass concentrations, but some health effects may relate to specific constituents such as bioaerosols, polycyclic aromatic compounds, and transition metals (Shiraiwa et al., 2017). Global modeling combined with epidemiological exposure-response functions indicates that ambient air pollution causes about 4.3 million of premature deaths per year, of which 4.04 million due to $PM_{2.5}$ (particulate matter with diameter lower than $2.5 \mu m$). The uncertainty on this estimate is 25% (95% confidence interval) (Chowdhury et al., 2020). The mortality, however, is not equally distributed throughout the globe; people who live in low and middle income countries disproportionately experience the burden of pollution with 91% of premature deaths occurring there, in particular in South-East Asia and Western Pacific regions. The 70% occurs in Asia, and more than 50% in China and India alone. Although the majority of deaths occur in these countries, per capita mortality is higher in Eastern Europe, as can be seen in the Figure 1.10.
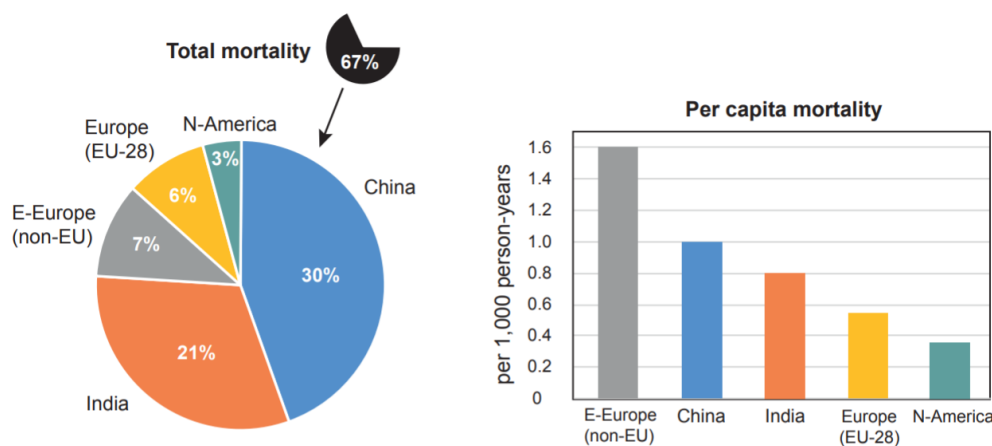
Figure 1.10: About two-thirds of the global mortality attributable to air pollution of 4.3 million/year occur in China, India, Europe and N-America (left). Though China and India lead in terms of total mortality, the per capita mortality is highest in Eastern Europe (right) (Shiraiwa et al., 2017).

1.4.3 Visibility effects

Visibility degradation is the most observable impact of air pollution and considered as a primary and general index of ambient air quality in an urban area (Watson, 2002). The term visibility may be defined as the farthest distance an object can be seen against the sky from the horizon (Seinfeld and Pandis, 2016). This depends on several factors such as optical properties of the atmosphere, amount and distribution of light, characteristics of the objects and properties of the human eye (Seinfeld and Pandis, 2016). Both particles and gases interact with light, and the interactions consist of light absorption and light scattering. These two processes, scattering (changes the direction of photon) and absorption (removes the photon from the beam by conversion to thermal or electronic energy) are collectively known as light extinction and responsible for visibility reduction. According to the mechanisms leading to the attenuation of light, the light extinction coefficient, b_{ext}, is usually conceived as comprising:

$$b_{ext} = b_{sp} + b_{sw} + b_{sg} + b_{ap} + +b_{ag} \tag{1.20}$$

where b_{sp} is the component due to scattering of light by particles, b_{sw} is the component of scattering of light due to moisture in the air; b_{sg} is the Rayleigh scattering by clean air, b_{ap} is the component due to absorption of light by particles and b_{ag} is mainly due to the absorption of light by NO_2 gas (Chan et al., 1999).

Gaseous scattering has minor contribution to visibility reduction in urban areas whereas scattering and absorption by atmospheric particles have been found to be more prominent reason of light extinction in urban areas (Chan et al., 1999). The effect of particulates on visibility is further complicated by the fact that particulates of different sizes are able to scatter light with varying degrees of efficiency (Malm, 1999). It is of interest to investigate the efficiency with which an individual particle can scatter light. The efficiency factor is expressed as a ratio of a particle's effective cross section (sum of scattering and absorption cross sections s^{sca} and s^{abs}) to its geometrical cross section s_g:

$$Q_{ext} = \frac{s^{sca} + s^{abs}}{s_g} \tag{1.21}$$

Figure 1.11 shows how this efficiency varies as a function of particle size parameter (or Mie parameter) defined as

$$x = \frac{2\pi r}{\lambda} \tag{1.22}$$

where r is the radius of the particle and λ is the wavelength under consideration. Very small particles and molecules are very inefficient at scattering light. As a particle increases in size, it becomes a more efficient light scatterer until, at a size that is close to the wavelength of the incident light, it can scatter more light than a particle five

times its size.
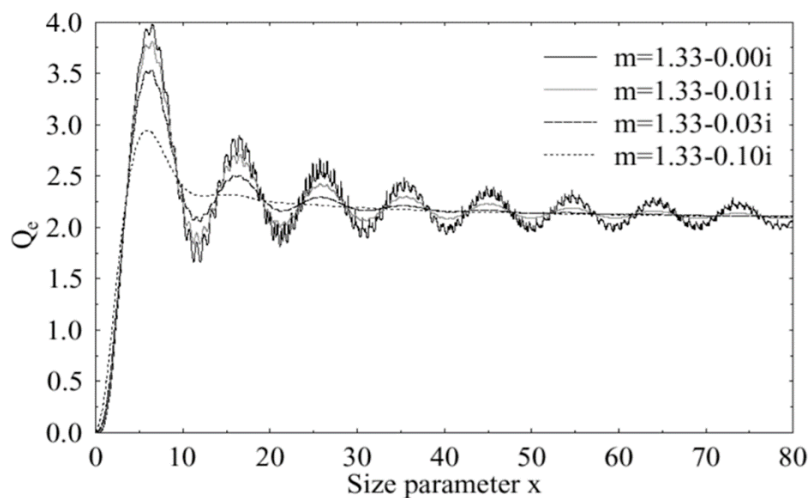
Figure 1.11: Examples of Q_{ext} calculated with the Mie theory for
several refractive indexes.

A further reduction of visibility depends on ambient relative humidity (RH), which has a great impact on aerosol optical properties (Deng et al., 2016). Atmospheric aerosols can be categorized into hygroscopic aerosols and non-hygroscopic aerosols. Hygroscopic aerosols include sulfates, nitrates, ammonium, sea salt and other inorganic components, as well as some water soluble organic compounds (WSOC), whereas, the chemical composition of non-hygroscopic aerosols mainly includes black carbon and some organic compounds. For ambient atmosphere, hygroscopic aerosols take up water as humidity increases (Engelhart et al., 2011). Aerosol water can affect both the size and refractive indices of atmospheric aerosols, thereby influencing the mass concentration, size distribution, and corresponding optical properties (Malm and Day, 2001). Relative humidity in the ambient atmosphere sees significant diurnal and seasonal changes. When RH reaches 70–80%, water content of aerosols can generally contribute 50% or more of the fine particle mass, becoming a controlling factor in aerosol optical properties as light scattering becomes greater with enlarged particular size (Bohren and Huffman, 2008). Hence visibility may be low on days with high aerosol loading and when humidity is high. Since rain scavenges aerosol particles from the atmosphere, some of the best visibility days occur after strong rain events.

1.5 New Particle Formation

Atmospheric new particle formation (NPF) and growth involves the formation of molecular clusters and their subsequent growth to larger sizes, first to a few nm in particle diameter, then to nucleation and Aitken mode particles in the sub-100 nm size range, and possibly up to sizes at which these particles may act as cloud condensation nuclei (CCN) (Kerminen et al., 2018). While the aerosol formation has been observed to take place almost everywhere in the atmosphere (Kulmala et al., 2012), serious gaps in our knowledge regarding to this phenomenon still exist. These gaps include existence and dynamics of atmospheric molecular clusters, vapours participating on atmospheric cluster formation, the effect of those clusters on atmospheric nucleation, the effect of ions on particle formation and also various impacts of the new particle formation on atmospheric chemistry, climate, human health and environment (Sipilä et al., 2008).
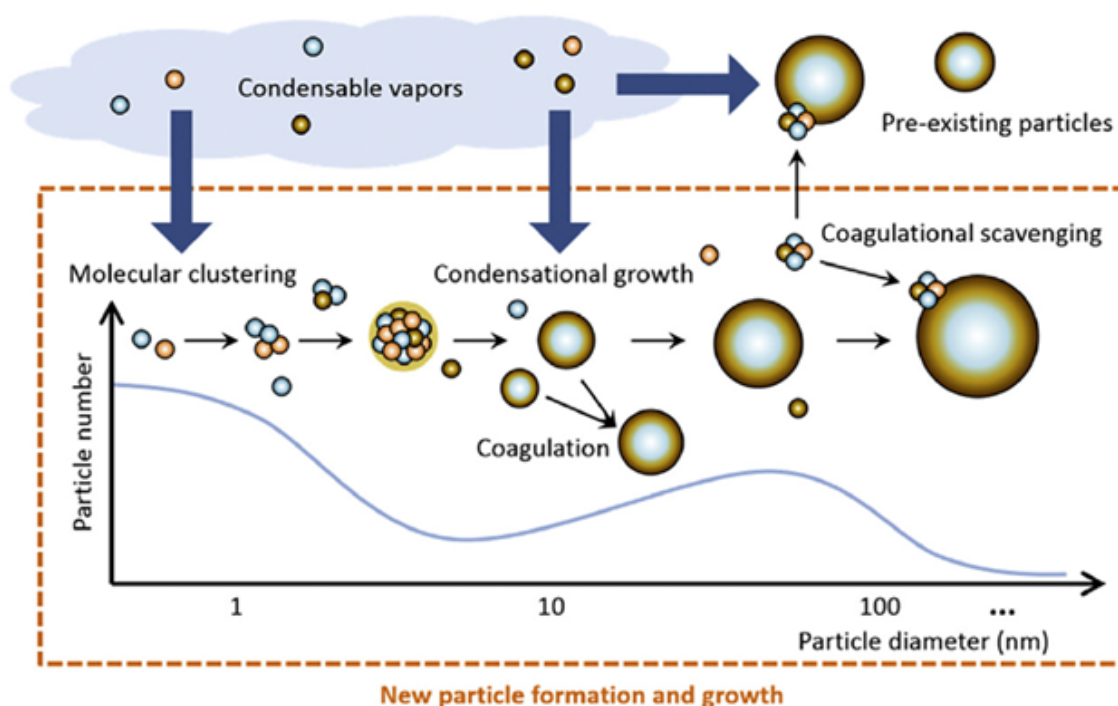
Figure 1.12: Schematic presentation of the main processes affecting atmospheric particle formation and growth (Olenius et al., 2018).

Formation and evolution in time of natural and anthropogenic aerosols are influenced by gas-to-liquid phase transitions. The formation process of a liquid phase from the vapor can usually be divided into three steps. First, a small amount of the new phase is formed spontaneously (nucleation). Secondly, an increasing amount of the new phase accumulates around the initially formed nuclei (condensational growth). Further particle growth is finally caused by collision and coalescence of the droplets

(coagulation). Depending on the actual physical situation, two or even all three of these processes can occur simultaneously. In the following paragraphs the processes of formation and growth, shown in Figure 1.12, are described.

1.5.1 Atmospheric Vapor and Particle Formation

As already mentioned in Chapter 1, secondary aerosols are particles formed via gas to particle conversion in which condensable vapours lead either to growth of preexisting particles by condensation processes or nucleation of new particles (Tomasi, Fuzzi, and Kokhanovsky, 2017). Atmospheric gas-to-particle conversion requires vapors whose ambient concentrations exceed their equilibrium vapor concentration, also referred to as volatility, over the condensed-phase particles. In practice, gas-phase chemical production of condensing vapors or rapid changes in the environmental parameters, such as the temperature, is necessary to initiate NPF. The vapors known to contribute to NPF include sulfuric acid (H_2SO_4) and a variety of oxidized organic species, together with basic compounds and water (Olenius et al., 2018).

Nucleation theory

Nucleation is the transformation of matter from one phase to another phase through the formation of nuclei. It is the initial stage of a first-order phase transition that takes place in various energetically metastable or unstable systems (Colbeck and Lazaridis, 2014). For atmospheric aerosols, nucleation refers to the transformation of gas-phase molecules into a cluster of molecules called an aerosol embryo or an aerosol nucleus (Boucher, 2015). Nucleation is responsible for production of the tiniest particles due to gas-to-particle conversion (Bychkov, Golubkov, and Nikitin, 2010). This process is sometimes called homogeneous nucleation to distinguish it from the process of heterogeneous nucleation where the phase change occurs on a pre-existing surface (Boucher, 2015). Classical nucleation theory to describe aerosol formation still forms the basis for the thermodynamic interpretation of aerosol nucleation processes. The fundamental concepts of the theory are described according to Curtius, 2009. The Gibbs free energy G is studied to characterize the atmospheric nucleation processes as the natural variables pressure and temperature can easily be measured. For a given, fixed pressure and temperature, a closed thermodynamic system will drive towards a state in which G is minimal. Let us start by looking at the nucleation process in the simplest case of a single substance A, for example, pure sulphuric acid. Substance A has a vapour pressure p_A. Its equilibrium vapour pressure over a flat surface of the bulk liquid A is $p_{A\infty}$. If the substance is supersaturated in the gas phase ($p_A > p_{A\infty}$) and far away from any other surfaces on which the gas phase molecules could condense on, the system is meta-stable and the vapour molecules would generally prefer to undergo

a phase transition to the condensed phase as a lower value of G could be obtained due to the lower chemical potential of the bulk liquid.
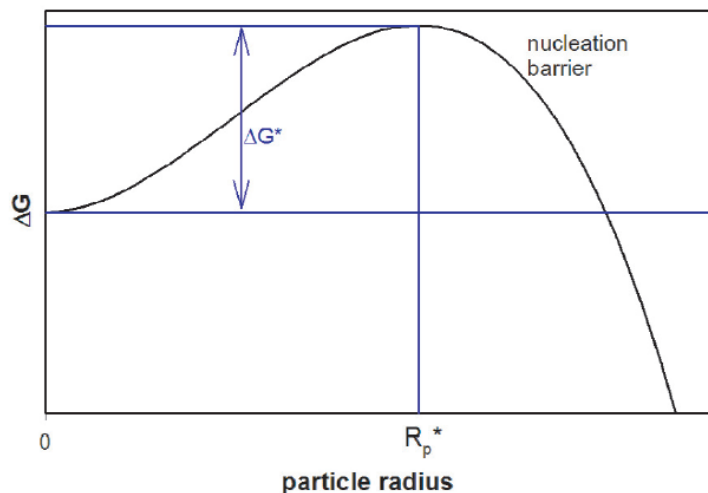
Figure 1.13: Thermodynamic representation of aerosol nucleation for a single chemical compound. A nucleation barrier of height ΔG^* exists. The critical cluster size R_p^* is defined by the maximum of the barrier (Curtius, 2009).

For a single substance the thermodynamics of the nucleation is then given by:

$$\Delta G = -\frac{4}{3}\pi R_p^3 \frac{kT}{v_l} lnS + 4\pi R_p^2 \sigma \tag{1.23}$$

This equation, illustrated in Figure 1.13, gives the change of the free energy G as a function of the nucleating particle's radius R_p. Here S is the saturation ratio, $S = p_A/p_{A\infty}$, k is the Boltzmann constant, T is the temperature, v_l is the volume occupied per molecule, and σ is the surface tension of substance A. As long as the system is supersaturated, S is greater than 1 and the first term of the right hand side of the equation is negative. Generally, this is the driving force for the gas-phase molecules to condense and thereby increase the particle's radius. Just in the beginning, for small R_p, the second term plays an important role. As the particle forms, a new surface, $A_p = 4\pi R_p^2$, has to be build up, costing surface energy. In the beginning this surface energy is bigger than the energy won from changing from gas-phase to particle-phase and therefore for small R_p an effective energy barrier exists (the so-called nucleation barrier) that prevents the gas from nucleation although it is supersaturated in the gas phase with respect to the flat surface equilibrium pressure. The location of the maximum of the barrier marks the critical radius.

Freshly nucleated particles do not all proceed to grow out of critical radius and contribute to new aerosol formation (Kulmala, Lehtinen, and Laaksonen, 2006). A cluster formed by nucleation can disappear before it gets a chance to lead to a new stable particle. Indeed, for small clusters with sizes smaller than the critical size it is

energetically more likely to evaporate off a molecule than another molecule condensing on them. In most cases such clusters will fall apart into separate gas molecules again. A cluster can be considered a stable particle when it has reached the size of the critical cluster, at which collisions begin to dominate over evaporation.

From differentiation of Equation 1.23 the height of the nucleation barrier ΔG^* and the position of the critical radius R_p^* can be determined

$$\Delta G^* = \frac{4\pi}{3}\sigma R_p^{*2} = \frac{4\pi}{3}\sigma \left(\frac{2\sigma v_l}{kTlnS}\right)^2 \tag{1.24}$$

This equation is known as the Kelvin equation. Although the classical nucleation theory has been quite successful in describing the nucleation process in general, it has to be noted that large differences exist between atmospheric observations and predictions by classical theory. There are several factors responsible for these discrepancies. On the one hand side, classical theory is limited and the bulk phase parameters like surface tension and density that enter into the classical equations are not suitable to describe the molecular clusters correctly. By now, some more sophisticated approaches exist, but agreement between atmospheric measurement and theory is usually still not satisfactory. This limited agreement is not only caused by the incomplete theory but also by the fact that the chemical compounds that actually cause the nucleation as well as the concentration, size and composition of the freshly nucleated cluster smaller than $3nm$ are still difficult to be measured.
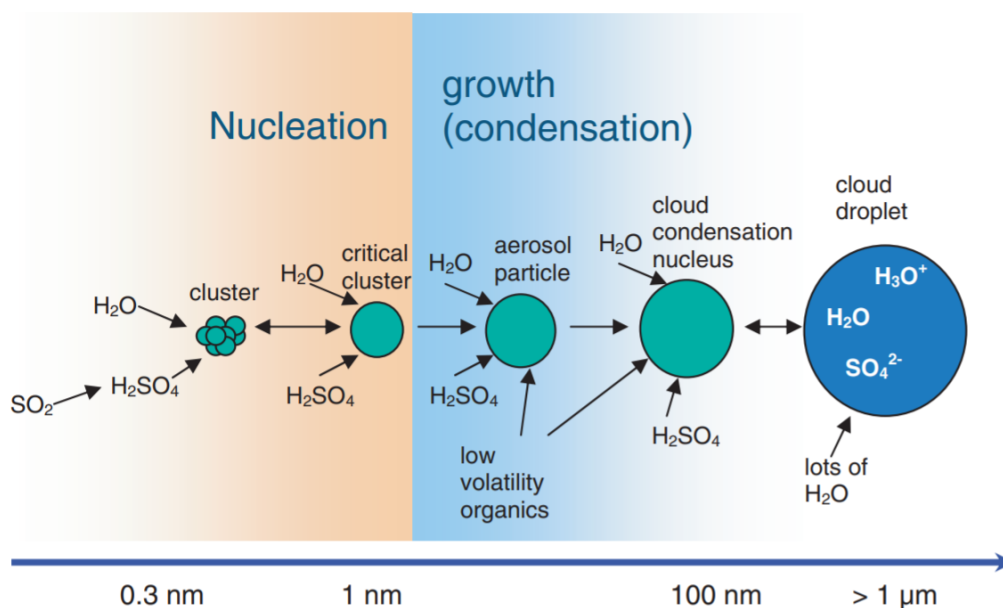
Figure 1.14: Schematic representation of the nucleation and subsequent growth process for atmospheric binary homogeneous nucleation of H_2SO_4 and H_2O (Curtius, 2009).

The formation of new particles from gaseous sulphuric acid and water is thought to be the most important atmospheric nucleation process (Curtius, 2009). A schematic for the formation of new particles from sulphuric acid and water vapour is shown in Figure 1.14. Once formed and thermodynamically stable, other substances such as condensable oxidized organic compounds take part in the growth of the newly formed particles and contribute the largest mass fraction of the particles.

1.5.2 Coalescence and condensational growth

As mentioned above, after initial formation of the aerosol by nucleation, growth takes place by the coalescence and condensation processes.

Coalescence is a process by which aerosol particles agglomerate together to form larger particles. Brownian coalescence takes place when, due to this motion, particles collide and adhere to each other, forming larger particles. This process causes the decrease of the total particle number concentration and an increase in the mean particle size. This is a particularly important process when concentrations are large, as it is the case for small particles in polluted areas, and more so in aerosol plumes themselves.

Condensational growth of aerosol particles is frequently encountered in the atmosphere and this represents a dominant process in terms of how much mass is transferred from the gas phase to the particulate phase (Szymanski and Wagner, 1983). Semi-volatile compounds, preferentially, condense onto the surface of pre-existing aerosol particles. The rate of condensation of these semi-volatile species onto a given aerosol particle is a function of the vapour pressure of the gas phase species, its saturation vapour pressure, the curvature radius of the particle, and the affinity between the gas and the particle (for instance the hydrophilic character of a particle for a gas that is soluble in water). The condensation of a gas phase species is easier onto a plane surface than onto a curved (convex) surface. It is, therefore, easier onto a large aerosol particle than onto a smaller aerosol particle. This is expressed by the Kelvin equation 1.24, which can be written as follows:

$$p(r) = p_\infty(r)exp\frac{2\sigma M}{R_v \rho_L r T} \tag{1.25}$$

where r is the particle radius (in m), σ is the surface tension (in Jm^{-2}), M is the molecular mass of the aerosol (in $kgmol^{-1}$), ρ is the density of the solution (in kgm^{-3}), $R_v = 8.314 Jmol^{-1}K^{-1}$ is the ideal gas constant, and T is the temperature (Boucher, 2015).

In Figure 1.15 a schematic view of a multi-modal particle size distribution illustrates the different growth and shrink processes. The smallest particles form by gas-to-particle conversion (nucleation mode) and grow through condensation of

gases and water vapour, initially relatively fast (Aitken mode) and from size of 50-100 nm diameter (accumulation mode) slower in size by coalescence. Beyond particle sizes of several 100 nm the efficiency of thermodynamic (evaporation, sublimation) and mechanical sink mechanisms (e.g. sedimentation, deposition/impaction) strongly increases.
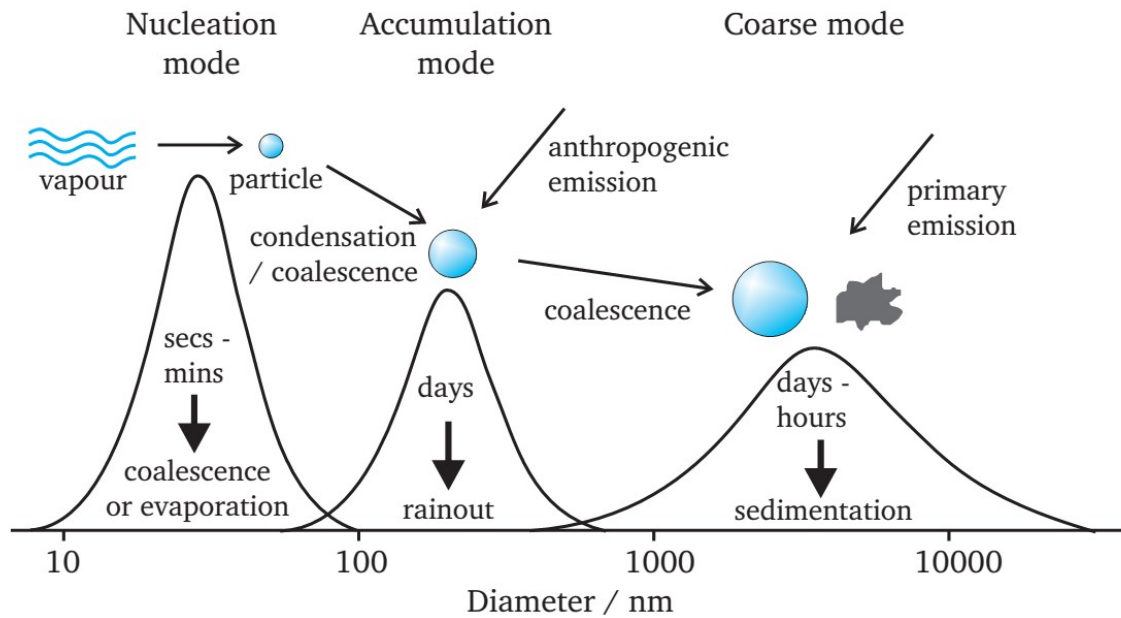
Figure 1.15: Schematic multi-modal particle size distribution with typical growth and shrink processes within each mode (© James Davies, 2014).

Chapter 2

Experimental setup and Methods

In the previous chapter the principal properties of aerosol particles and the important role they play on climate system and health, have been assessed. The principal objectives of this thesis are the long term study of new particle formation and the investigation of the behaviour of ultrafine aerosol particles size distribution measured at the *O. Vittori* observatory on the top of Mt. Cimone. The aerosol number size distribution observation at Mt. Cimone has been implemented in the frame of EUSAAR FP6 program, in November 2005 and continuously carried out also in the frame of ACTRIS-FP7 and ACTRIS-2-H2020 programs. This station represents a strategic platform to study the climatology of the free troposphere in the South Europe and the Mediterranean.

The measurement site of the GAW-WMO Station Mt. Cimone is described in this chapter, which also explains how the Differential Mobility Particle Sizer (DMPS) assembled by Kuopio University (Finland) measured the aerosol size distribution from November 2005 to July 2013. Then, a description of the data preprocessing performed to obtain a homogeneous and clean data set is presented. Finally, the methods and tools used to analyze the number concentrations and to classify the new particle formation events are discussed.

2.1 Measurement site

High mountain areas are sites where background atmospheric compositions and environmental change processes can be studied thanks to continuous monitoring activities that constitute also an important aid for the understanding of global change processes. Mountain regions are representative of wide spatial areas, they are often in "clean" conditions and thus they constitute an extraordinary platform for monitoring climate change and its effects. Climate change may be studied in mountain regions through a wide range of phenomena, including changes of average concentrations, variability, seasonality, the incidence of extreme events of polluted conditions, etc (Bonasoni et al., 2002). Moreover, there is a need to understand

regional to intercontinental transport of aerosols in order to formulate more efficient policies for monitoring of aerosols and their precursors, and for emission abatement strategies (Myhre and Baltensberger, 2012). The vast majority of current information comes from stations located in urban and peri-urban areas and this information is often limited to regulated parameters, such as mass concentration. This is clearly not sufficient to provide the pertinent information of interest to air quality and climate studies. Variability of advanced aerosol variables, such as aerosol size distribution, are more and more required. For these reasons, analysis and investigations of atmospheric components, like particulate matter, are usually carried out in scientific research stations or observatories sited in high mountain areas.

Mt. Cimone (44°12' N, 10°42' E, 2165 m a.s.l.) is the highest mountain peak in the northern Apennines. It has an elevation of 2165 m and it has a completely free horizon at 360° degrees and can therefore be reached freely by air masses from any direction. The nearest industrial areas are at least 40 km away, while the nearest inhabited areas are small towns 15 km away and 1100 m below. The nearest roads are 7 km away and one km lower and the environment surrounding the station is characterized by meadows and rocky areas. The woods, mainly of conifers and beeches stop at an altitude of 1600 m. These characteristics make the measurement site very suitable for investigating the background conditions of the Mediterranean troposphere as well as the direct impact of surface emissions to them (Cristofanelli et al., 2018). On its top, there are several constructions, among them military radar installations and a meteorological station, officially recognized by the world meteorological organization. The latter is called CAMM (Centro Aeronautica Militare di Montagna). It works round the clock regularly since 1946 and it deals with traditional meteorology (aeronautic and synoptic) for air navigation assistance and for weather forecast service and with GAW observations for climate and atmospheric changing monitoring. The Centre is composed by a Gathering and Processing Data Service, a Meteorological Station and a Special Observations Unit.

2.1.1 The *O. Vittori* Observatory at Mt. Cimone

The *Ottavio Vittori* Climate Observatory (Figure 2.1), is part of the GAW-WMO Station Mt. Cimone (GAW id: CMN), the only one among the 31 Global Stations of the Global Atmosphere Watch (GAW) program of the World Meteorological Organization (WMO) present on the Italian territory and in the Mediterranean Basin. The observatory is managed by the National Research Council of Italy (CNR) and is hosted by the buildings of the Italian Air Force operative base. CMN also belongs to ACTRIS RI (Aerosol, Clouds, Trace gases Research Infrastructure), a pan-European research infrastructure producing high-quality data and information on short-lived

climate forcers (SLCFs) and other short-lived atmospheric constituents, as well as on the processes leading to the variability of these constituents in natural and controlled atmospheres.

Figure 2.1: Mt. Cimone peak, with the Observatories of Italian Air Force and CNR (© M. Landi, 2020).

ACTRIS has been recognized by ESFRI (the European Strategy Forum on Research Infrastructures) among the research facilities of pan-European importance that correspond to the long-term needs of the European research communities. As already mentioned, due to the completely free horizon, high altitude, and great distance from major pollution sources, CMN represents a strategic platform to study the chemical–physical characteristics and climatology of the free troposphere in the South Europe and Mediterranean basin (Cristofanelli et al., 2017).

At the Observatory, the research activities began in 1991 while continuous monitoring of climate-altering compounds, trace gases and aerosol, solar radiation as well as meteorological parameters are carried out starting from 1996. Over the years, several

field campaigns have been also hosted at this research infrastructure in the framework of different EU projects.

The measurements activities carried out at the Observatory help to better monitor the changes of atmospheric composition, to investigate the processes influencing climate and to asses the contribution of short and long-range air mass transports to atmospheric variability of different compound concentration. Mt. Cimone observations are also used to calibrate and verify data from satellites and model simulations.

2.1.2 Meteorological description

Colombo et al., 2000, provided a meteorological description of Mt. Cimone weather regime from 1946 to 1999. They showed that Mt. Cimone is the windiest meteorological site in Italy (wind speed higher than 200 km/h is occasionally observed) and the prevailing winds blow from S–SW and N–NE. This was evident also by analyzing the wind observations carried out from 1996 to 2015 at the *O. Vittori* observatory (Figure 2.2).
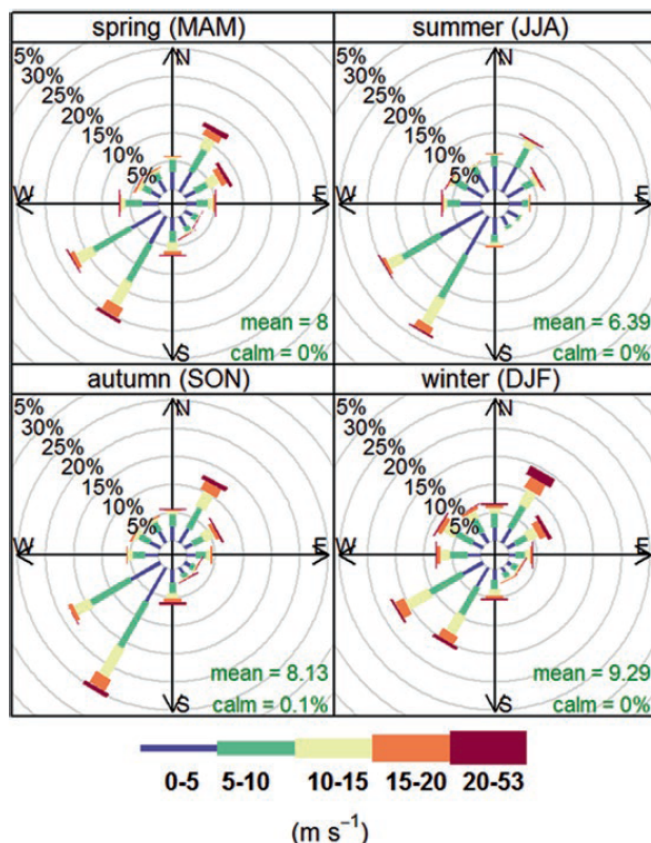
Figure 2.2: Wind speed/direction frequencies by season at CMN (1996–2015). Wind speeds are split into the intervals shown by the scale in each panel. The grey circles show the 5% frequency intervals (Cristofanelli et al., 2017).

In winter and fall, when temperate air masses flow from the Mediterranean Sea, the temperature only occasionally lies above $0°C$. On the other hand, when continental air comes from N and NE, the temperature is usually several degrees below $0°C$. The annual variation and the seasonal diurnal variation of temperature over the last two decades, shown in Figure 2.3, were calculated using hourly average values. In particular, the mean value estimated is around $3.2°C$. The lowest monthly mean temperature was in February 2005 $(-7.9°C)$ and the highest in July 2015 $(14.9°C)$ (Cristofanelli et al., 2017).
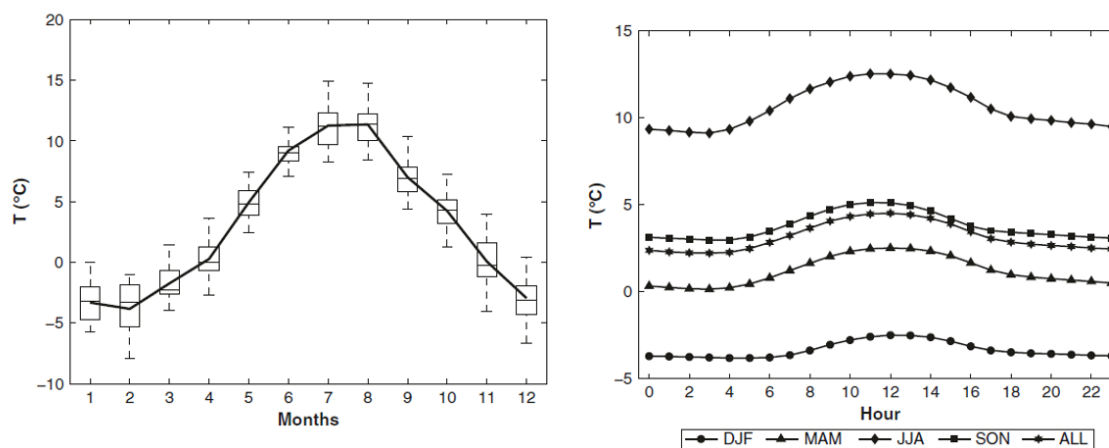
Figure 2.3: The left plot reports the averaged seasonal cycle (continuous line) and monthly 25th, 50th and 75th percentiles; the whiskers extend to the most extreme hourly values not considered outliers. The right panel shows the temperature seasonal diurnal variation (Cristofanelli et al., 2017).

As reported by previous investigations, the atmospheric observations carried out at CMN can be considered representative of the free tropospheric conditions of the Mediterranean basin/South Europe during the cold months as well as during nighttime in the warm season. However, from April to September, the measurement site can be affected by thermal wind circulation and convective vertical transport of air masses. Indeed, during daytime, upslope and valley winds together with diurnal planetary boundary layer (PBL) growth and entrainment processes can favor the vertical transport of polluted PBL air to the measurement site (Colombo et al., 2000; Cristofanelli et al., 2009).

To give an idea of the atmospheric circulation which characterizes Mt. Cimone, some results of the back trajectories cluster analyses conducted by Brattich et al., 2020 are reported. Figure 2.4 shows the representative trajectories of the 8 clusters obtained at 2200 m a.s.l. and the relative percentage frequency of each flow pattern between 1998 and 2011. As it can be clearly seen, westerly flows constitute most of

the trajectories. In particular, all westerly trajectories together represent more than 60% of the flows, and are classified into Northern Atlantic (N Atl), North America (N Am), Atlantic (Atl), Western (W), and North-Western Europe (NW-Eu), according to their region of provenance. The remaining trajectories are classified into Arctic (A), Eastern (E), and Mediterranean-Africa (Me-Af).
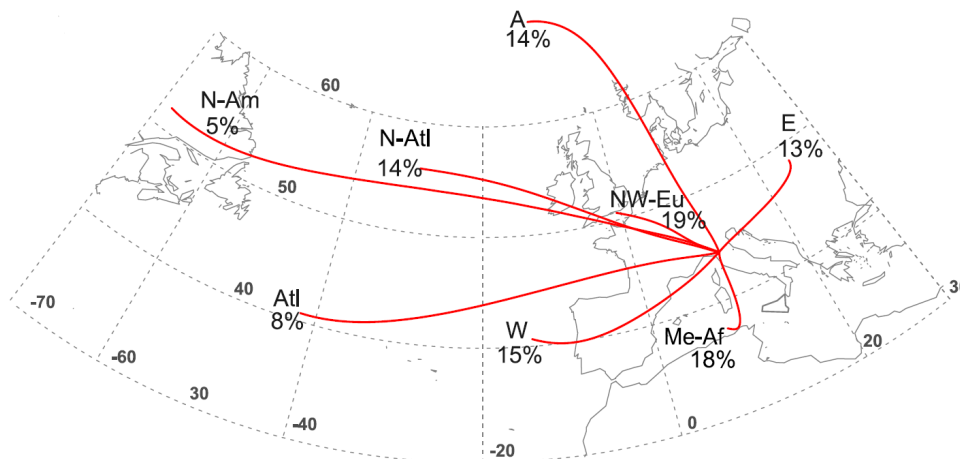
Figure 2.4: Centroids of the trajectory clusters identified for 96-h backtrajectories arriving at 2200 m asl between 1998 and 2011. The flow pathways are identified as follows: Arctic (A), Eastern (E), Mediterranean- Africa (Me-Af), Atlantic (Atl), Northern Atlantic (N-Atl), North America (N Am), North Western-Europe (NW-Eu). The frequency of occurrence of each flow pattern in the whole 12-year study period is represented by the percentage (Brattich et al., 2020).

Brattich et al. found that North-American air masses are related to low pressures and tropopause heights, cold, and dry air masses, and linked to high wind speeds. These flows are negligible during summertime and are related to low concentrations of atmospheric pollutants (BC, CO, O_3, PM_{10}). Artic air masses are typically cold, even though less cold than North American ones. They are more frequent in the cold season and they are associated with low values of atmospheric pollutants (CO, O_3, BC, PM_{10} and $210\,Pb$). NW-Europe, Western and Eastern flows are connected to high levels of CO, BC, O_3 and fine particles number densities, leading to corresponding increases in PM_{10}. In those cases, the local and regional transports can be associated with meteorological conditions characterised by low ventilation that, especially during warm months, can also promote the diurnal-scale transport of PBL air-masses to the receptor site as previously investigated by Cristofanelli et al., 2016. Finally, Mediterranean-Africa flows are associated with Saharan Dust events and bring about high PM_{10} values, both in the fine and coarse fraction of particles.

2.1.3   Aerosol observations

The first aerosol measurements at Mt. Cimone started in 2002, with an Optical Particle Counter (OPC), which is still running, and measures the number size distribution of particles with a diameter between $300nm$ and $20\mu m$. Since June 2005, the aerosol absorption coefficient has been measured, and makes it possible to trace the concentration of black carbon. Afterwards, within the EUSAAR and AEROCLOUDS projects, the measurement of the total scattering coefficient at $520nm$ was added. An upgrade in 2013 makes the scattering coefficients measured at three wavelengths. The coarse mode is better characterized with an Aerosol Particle Sizer (APS) since 2015, measuring the number size distribution of coarse mode, based on aerodynamic diameter.

2.2 Differential Mobility Particle sizer

At the O. Vittori observatory at CMN, a Differential Mobility Particle Sizer (DMPS) built by Kuopio University (Finland) which measures the aerosol size distribution from 10 to 500 nm since November 2005. The principle of a differential mobility particle sizer is based on the electrical particle mobility. It consists of a sequential setup composed by a bipolar diffusion charger, traditionally named neutralizer, a Differential Mobility Analyzer (DMA), and a Condensation Particle Counter (CPC), as shown in the schematic sketch reported in Figure 2.5. The set-up also includes dryers for aerosol flow and sheath air, heat exchanger, particle filters, as well as sensors for aerosol and sheath air flow rate, relative humidity and temperature of aerosol flow and sheath air, and absolute pressure. After electrical charge balance in the neutralizer, aerosol particles are classified by their electrical particle mobility in the electric field of a cylindrical capacitor, the DMA. The electrical mobility has a unique match with the particle diameter. Afterwards, a particle counter, the CPC, counts the aerosol particles selected by DMA. In the following paragraphs the operating principle of the main components is explained in detail. Most of the information of this section comes from the DMPS user manual, from Wiedensohler et al., 2012, and from Knutson and Whitby, 1975.
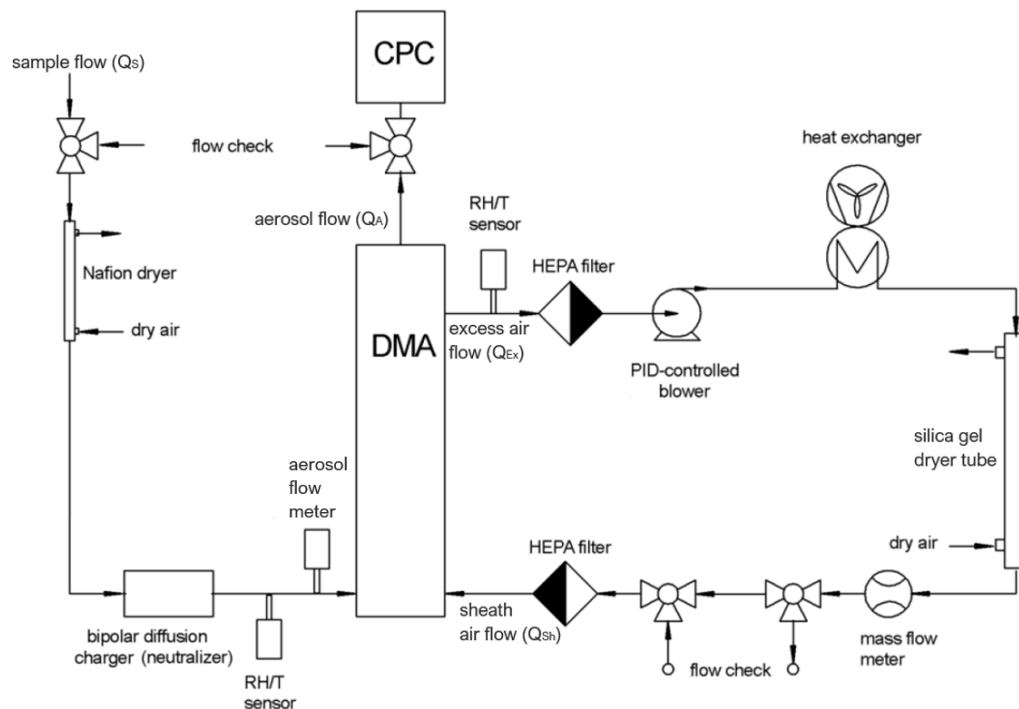
Figure 2.5: Schematic sketch of the closed-loop DMPS.

2.2.1   Relative humidity (RH) control

Due to the hygroscopic growth of atmospheric aerosol particles at RH well below the saturation, it is essential to control or limit RH in the DMPS. The philosophy is to obtain comparable data sets and therefore to measure the dry particle number size distribution. The RH is limited below 40% so changes in particle diameter as a result of RH are expected to be below 5% (Wiedensohler et al., 2012). A dry aerosol sample is needed to ensure the correct bipolar charge equilibrium and thus sizing downstream of the bipolar diffusion charger in the DMA, so a Nafion dryer tube is placed before the neutralizer. Moreover, a dry sheath air is needed to ensure particle sizing inside the DMA with a minimum fluctuation in RH and for this purpose a Silica Gel Dryer Tube is incorporated in the DMA sheath flow system, which is a closed loop. RH in both the aerosol and sheath air flows are monitored continuously by RH/T sensors.

2.2.2   Bipolar Diffusion Charger (Neutralizer)

A typical bipolar diffusion charger comprises a radioactive source such ^{85}Kr, ^{210}Po, ^{241}Am, ^{63}Ni or ^{14}C. In the charger, the radioactive alpha or beta particles, the gamma radiation or the bremsstrahlung ionize the aerosol carrier gas. The Mt. Cimone DMPS charger is based on a ^{63}Ni source, producing beta particles. The positive and negative ions are transported to the particles by diffusion and electrostatic forces. Bipolar diffusion charging is also referred as neutralization, as the total charge across all aerosol particles may approach a near neutral state. This means that the neutralizer does not neutralize charges, but rather brings the particles into a well-known charge distribution. The result is a Boltzmann distribution of negative and positive charged particles as the one already described in Equation 1.11.

2.2.3   DMA

A Differential Mobility Analyzer separates electrically charged particles according to their electrical mobility by making use of a radial electric field established between two coaxial cylinders and a particle-free gas stream (called sheath flow) which flows through the annular gap between the cylinders. Charged particles are continuously injected at a given axial position through an annular slit in the outer cylinder, they drift in the radial field towards the inner cylinder, as they are carried axially downstream by the sheath gas. Only particles with certain electrical mobility are collected by the annular monodisperse slit in the inner cylinder. A schematic sketch of the DMA is shown in Figure 2.6.
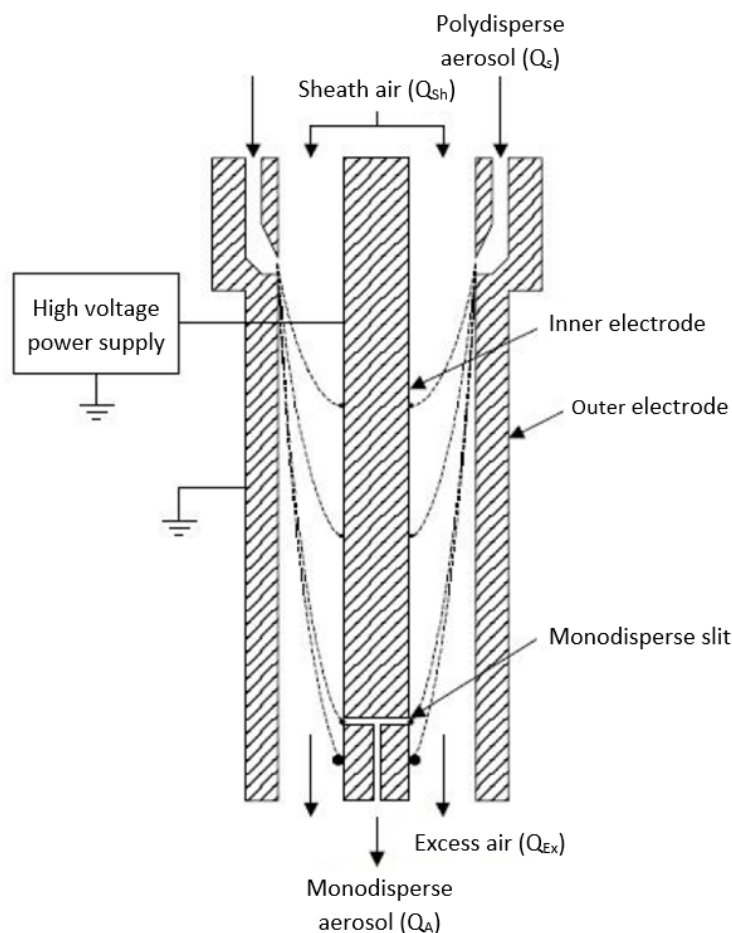
Figure 2.6: Schematic sketch of a DMA showing trajectories of particles with different electrical mobility.

The DMA installed at Mt.Cimone is built as a cylindrical capacitor. A high voltage is employed between the inner center electrode (positive potential) and the outer-grounded electrode. The incoming sample flow containing the polydisperse aerosol Q_S, constant at a rate of $1 l/min$, is injected through an annular slit closed to the outer electrode into the DMA and then merged with the particle-free sheath air flow Q_{Sh}, with a rate of $5 l/min$. All flows should be strictly laminar. Due to the electric field, only negatively charged aerosols of a specific size are selected to be counted downstream by the CPC, while positively charged and larger particles precipitate onto the outer electrode, while neutral and smaller particles leave the DMA as excess air Q_{Ex}. As shown in the sketch of the DMPS in Figure 2.5, the DMA sheath flow system is a closed loop. Air is sucked by a blower from the lower exit of the DMA (Q_{Ex}) and passes a filter. A mass flow controller upstream of the blower regulates the flows and, after passing all the other components placed in the loop, the particle free air enters the DMA again (Q_{Sh}). If there are no leaks, $Q_{Sh} = Q_{Ex}$. Charged particles are separated according to their electrical particle mobility, corresponding

to the selected particle diameter. By knowing the dimensions of the DMA (length and diameters of the inner and outer electrode), it is possible to calculate the voltage between the electrodes needed to transport charged particles with a certain electrical particle mobility from the entrance to the annular monodisperse slit in the center rod of the capacitor. Indeed, according to Knutson and Whitby, 1975, electric mobility in a DMA for a certain deposition location can be described by the following equation

$$Z_p = \frac{Q_{Sh} + Q_{Ex}}{4\pi V \Lambda} \tag{2.1}$$

where Q_{Sh} is the sheath air flow at the DMA entry and Q_{Ex} is the sheath air flow at the DMA exit, V is the voltage applied between inner and outer electrode and Λ is an instrument constant given by

$$\Lambda = \frac{L}{ln\left(\frac{r_{in}}{r_{out}}\right)} \tag{2.2}$$

where L is the DMA length, r_{in} the radius of the inner electrode from the DMA capacitor and r_{out} the radius of the outer electrode from the DMA capacitor, i.e. the inner radius of the DMA cover. The trasmitted particles, carried by the aerosol flow Q_A, that pass through the monodisperse slit must satisfy the following mobility-voltage relationship, derived from equations 1.1 and 2.1:

$$V = \frac{3\eta Q_{Sh}}{2ne\Lambda}\frac{Dp}{C_c} \tag{2.3}$$

By ramping the DMA voltage, the selected particle diameter can be changed, so the electrical particle mobility distribution is determined by scanning the voltage through the entire electrical particle mobility range to be investigated. In ideal conditions, if there are no lacks, $Q_A = Q_S$, so the scope of the DMA for the continuity equation is

$$Q_A + Q_{Sh} = Q_S + Q_{Ex} = 6l/min \tag{2.4}$$

Finally, the particle number concentration in the sample flow is measured in the CPC.

2.2.4 CPC

The Condensation Particle Counter (CPC) is based on the physical property of condensation of butanol vapor on particles, which grow to several micrometers to be optically detectable. A schematic sketch is shown in Figure 2.7.
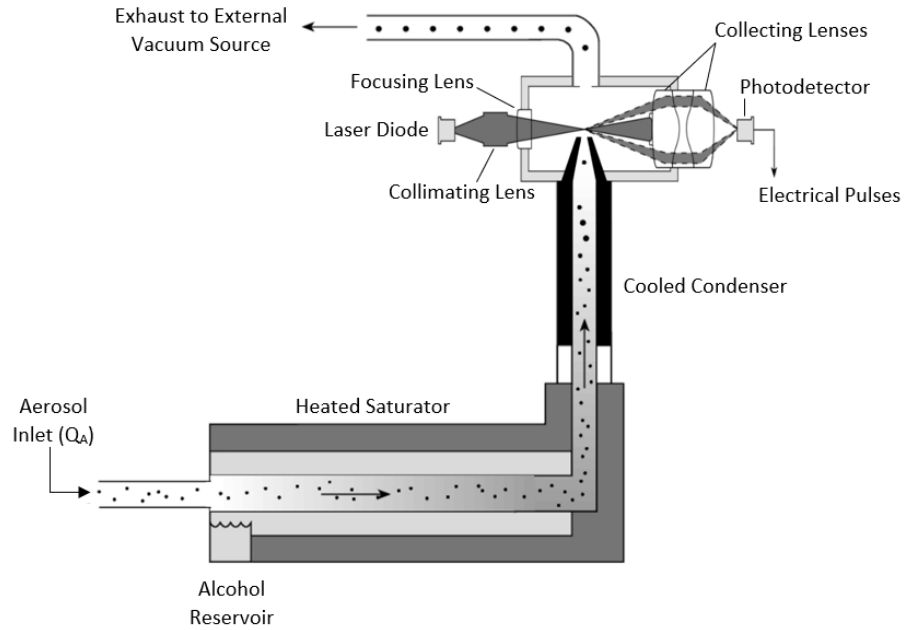
Figure 2.7: Schematic sketch of a Condensation Particle Counter.

The sample flow Q_A is sucked through the CPC with a constant flow at a rate of $1l/min$. First, the aerosol flow is saturated with butanol vapor in a slightly heated saturator. Afterwards, the aerosol is led through a condenser to reduce the temperature by approximately 17K. The butanol vapor becomes supersaturated, condenses onto the particles, and the aerosol particles grow to micrometer sized droplets. Since the equilibrium saturation ratio of a droplet is a function of droplet size, particles smaller than a certain size are not activated to a droplet. For this reason, the efficiency of the counter gradually decreases at smaller sizes, and the lower cut-off size is defined as the size at which 50% of particles are counted. The CPC TSI model 3010 is able to detect 50% of particles at a size of 10 nm. As droplets exit the condenser, they pass through a thin ribbon of laser light. Light scattered by these droplets is collected by optics and focused onto a photodetector. The photodetector converts the light signal to an electrical pulse, which is recorded as a particle count.

2.3   Data Preprocessing

From November 2005 to July 2013, CMN DMPS collected data of aerosol size distributions with a temporal resolution of 10 minutes, which is the time required by the instrument to measure a complete particle number size distribution. Indeed, by keeping the flows Q_S and Q_{Sh} constant, the DMPS scans over a discrete (13 to 39) number of DMA voltages in order to select particles of different electrical mobilities, according to Equation 2.3. At each of these voltages, a measurement is performed with the CPC during 10 s, while 5 s are needed to change voltage step; a PC, which is part of the measuring system, menages the hardware settings, collects, inverts and stores data. During the measurement period, the maintenance operations, such as flows calibrations, were regularly carried out. Small adjustments in flows ratios lead a change in balancing the channel and than the number and limits of size bins. All these complications generated a non-homogeneous data set in which either the number of electrical mobility diameters (number of channels), and the actual bin sizes of the instrument have changed slightly over the years. Indeed, this variation occurred 33 times, ranging from 13 to 39 channels in a random manner. Therefore, in order to obtain a new homogeneous data set, all data have been harmonized to a fixed logarithmic equidistant size grid distributed over 37 bins between 9nm and 500nm.

In this section all the necessary steps to create the homogeneous and clean data set are illustrated, starting from a fitting procedure. The latter provides the modal parameters necessary to calculate the new harmonized size distributions. All size distributions retrieved are then analyzed in terms of total number concentration, nucleation, Aitken and accumulation mode. Finally, inconsistent data are removed during the filtering procedure.

2.3.1   Data fitting

The starting data provided by the DMPS acquisition is a collection of daily tables, each one organized as shown in Figure 2.8. In the first column sampling time is recorded in a day-of-the-year format. This format is converted in date YYYY-MM-DD and time hh:mm:ss [1]. The second column contains the total number concentration N_{tot}, namely the calculated particles concentration per cubic centimeter. The following columns report the acquired size distributions for each sampling time. The first row, since the third column, displays the values of each size bin in meters, identifying the dimensional classes of particle diameters.

---

[1]From now on, all times are expressed in terms of local time (UTC+1)
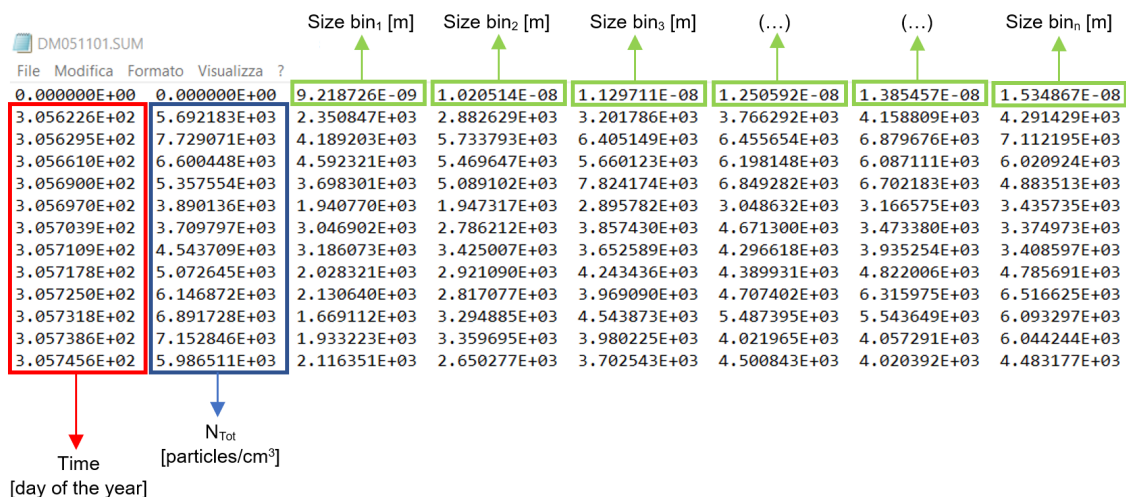
Figure 2.8: Structure of daily files available from the raw data set.

The first step in order to achieve a coherent data set is the application of an automated fitting method that has been developed at the University of Helsinki (Hussein et al., 2005), previously adopted by other studies, including Järvinen et al., 2013 and Dal Maso et al., 2005. The algorithm, which was developed using Matlab, has been converted to Octave syntax, which is largely compatible with Matlab. This algorithm parameterizes aerosol particle number size distributions with the multi log-normal distribution function. It does not need a user control for initial assumptions of the log-normal parameters. The only required input parameter is the maximum number of log-normal modes. It works by analyzing the measured size distributions to decide the number of modes to fit, then it makes a starting guess of the modal parameters and it uses a least-square minimization method to fit 2-3 modes according to the measured size distribution. It then returns parameters of the log-normal modes found (Dal Maso et al., 2005). These parameters are organized according to Jaenicke, 1993, which means they are listed as follows: geometric particle diameters, $Dp_{g,i}[m]$, geometric standard deviation, $\sigma_{g,i}[m]$ and total number concentration, $N_{0,i}[\#/cm^3]$. If only 2 modes are recognized, than the parameters related to the missing mode are automatically recorded as not a number (NaN). The tables provided by the fitting method also contain in the last two columns the least square of fitting and the number of modes for each log-normal distribution. Since these tables are split in daily files, and the data contained will be useful for the calculation of the new size distributions, they are merged into annual tables.

2.3.2 Size distribution

The following step to the fitting procedure is the development of a code in R programming language necessary to calculate the particle size distribution starting

from the parameters of the log-normal modes previously retrieved. The script I developed consists of several steps. Firstly, it calculates the following equation for each mode:

$$n_{N,i}(logDp) = \frac{dN_i}{dlogDp} = \frac{N_{0,i}}{\sqrt{2\pi}log\sigma_{g,i}}exp\left(-\frac{1}{2}\frac{(logDp - logDp_{g,i})^2}{log^2\sigma_{g,i}}\right). \tag{2.5}$$

The calculation is performed for each Dp which is the electric mobility diameter settled in the new fixed set of 37 size bins, and for every sampling time. Then, in order to obtain the total log-normal distribution for each sampling time, particle size distribution of each mode are added together:

$$n_{N,tot} = \sum_{i=1}^{3} \frac{dN_i}{dlogDp}. \tag{2.6}$$

By doing so, new annual tables containing the particle size distribution are created starting from the modal log-normal fit parameters and the new unique set of size bins. These tables are the basis for all the analyses that will follow in the next paragraphs. In Figure 2.9 two examples of both measured size distributions and calculated ones are plotted together.
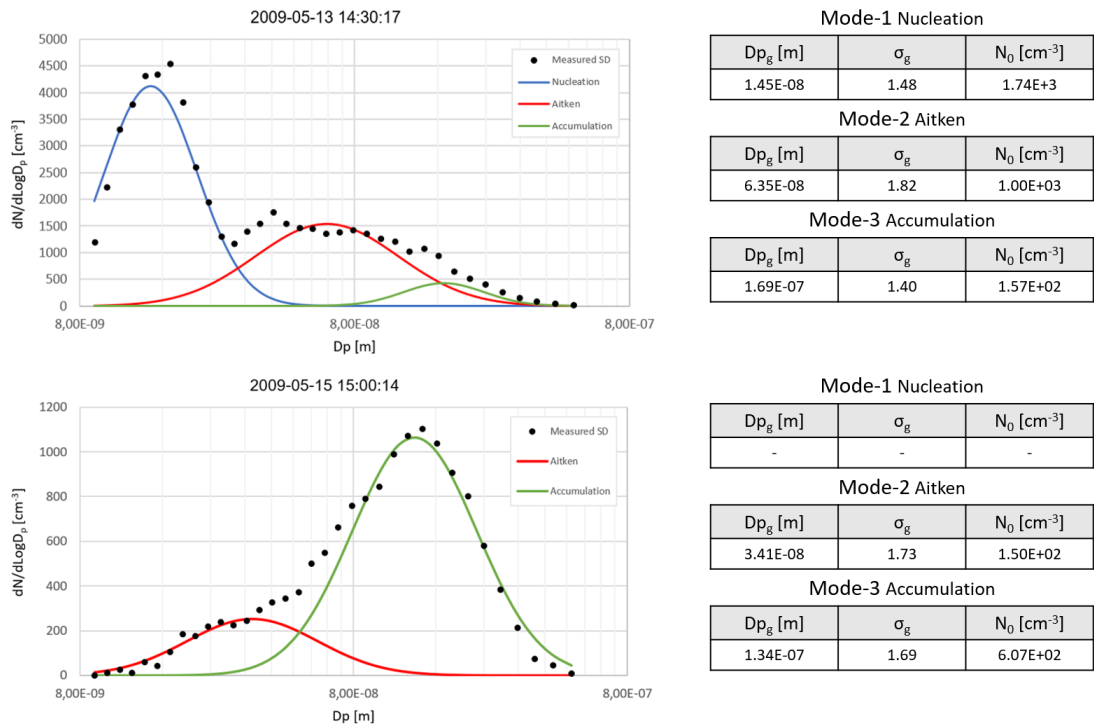
Figure 2.9: Examples of measured size distributions (black points) with the corresponding log-normal fit parameters used to calculate the new log-normal distributions for each mode (coloured lines).

The upper panel of Figure 2.9 shows a size distribution with three modes, the nucleation ($9 - 25nm$), Aitken ($25 - 100nm$) and accumulation ($> 100nm$) modes. The markers represent measured data points and the solid lines show the modes which are obtained by running the script. The lower panel shows a bimodal size distribution with no nucleation mode particles.

Moreover, the script provides two other new data set. The first one is a collection of annual tables of aerosol surface area distributions for each sampling time, which are calculated by applying the formula:

$$n_{S,tot} = \sum_{i=1}^{3} \pi Dp^2 n_{N,i}(Dp) \tag{2.7}$$

Finally, the second database is a collection of annual tables of aerosol volume distributions for each sampling time, which are calculated by applying the following equation:

$$n_{V,tot} = \sum_{i=1}^{3} \frac{\pi}{6} Dp^3 n_{N,i}(Dp) \tag{2.8}$$

2.3.3 Number concentration

Through the new homogeneous data set of aerosol size distributions, it is now possible to obtain the total number concentration and the number concentration for each mode: nucleation, Aitken and accumulation. Indeed, using a R script I made, the value of dN_k for each bin size was calculated by applying the equation:

$$dN_k = \frac{dN_k}{dlogDp_k} \cdot (logDp_{j+1} - logDp_j). \tag{2.9}$$

In this equation Dp_k refers to the size bin, while Dp_{j+1} and Dp_j are the diameters which identify the range boundaries of the k-th size bin. The next step is to find the total number concentration, by simply adding up dN_k for each size bin:

$$N_{tot} = \sum_{Dp=9,05nm}^{600nm} dN_i(Dp_t); \tag{2.10}$$

where $9.05nm$ is the lower size limit detectable by the DMPS, while $600nm$ is chosen as upper size limit of the accumulation mode. This choice is mainly driven by the fact that this value represents the maximum size value adopted even by instrument situated in other acquisition sites as it allows easy comparison with data acquired by other structures. The number concentration of every mode is obtained just by adding

up the size bins included in a certain diameter range, depending on the mode:

$$N_{nuc} = \sum_{Dp=9,05nm}^{24,7nm} dN_i(Dp_t); \quad N_{Ait} = \sum_{Dp=24,7nm}^{96,4nm} dN_i(Dp_t); \quad N_{acc} = \sum_{Dp=96,4nm}^{600nm} dN_i(Dp_t).$$

(2.11)

Once the number concentrations have been derived, they are recorded in annual tables for each sampling time. To provide the most effective data visualization, a set of annual html based files, which plot the number concentration trend for each mode is obtained through a R script. Indeed, by opening the html file on a browser, it is possible to zoom in on different time periods such as months, days or a single hour. An example of the rendered html file for 2009 is reported in Figure 2.10, where it is performed a zoom in on September (Figure 2.10b). With this kind of plot it is possible to scroll every single sample and display the respective number concentrations for each mode. These values for September 21st, 2009 at 7:00:46 A.M. are reported in Figure 2.10b, as an instance.
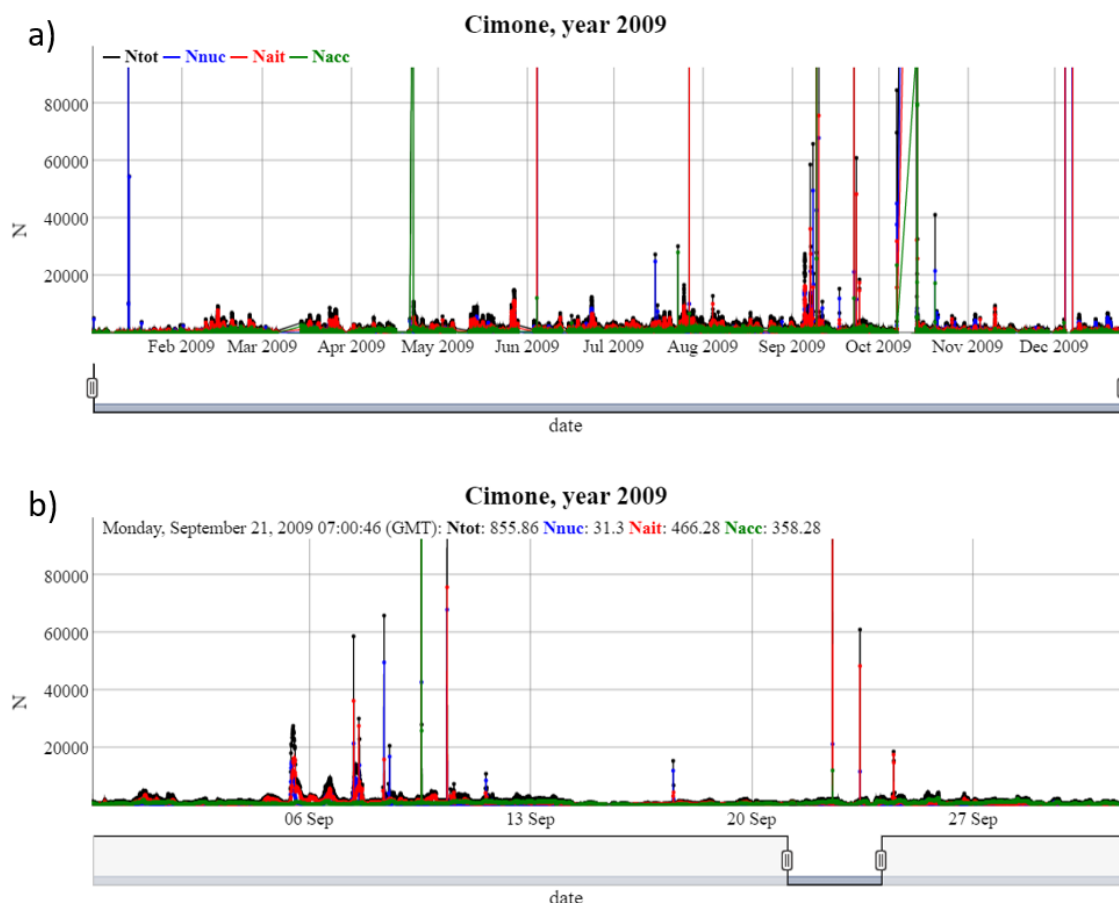
Figure 2.10: a) Time trend of the total particle number concentration and of the number concentrations of each particle mode for 2009. b) Zoom in on September, 2009, with values of number concentrations reported for September 21st, at time 07:00:46 A.M.

Examining these plots, data visualization shows the need to filter the data set due to both the presence of numerous spikes and of time intervals in which particle numbers reach unlikely high values. The next step is therefore the filtering of the data set which will be described in the following paragraph.

2.3.4 Data filtering

A series of attempts were made to figure out the best way to filter the data, the most relevant ones are outlined below.

At first, the ratio between the measured number concentration $N_{tot,mes}$ and the calculated number concentration $N_{tot,cal}$ for each sampling time was calculated. $N_{tot,mes}$ is reported in the second column of the starting data set as shown in Figure 2.8, while $N_{tot,cal}$ was found through the application of Equation 2.11. Only samples featuring a calculated number concentration which satisfies the following equation were maintained:

$$0.9 < \frac{N_{tot,meas}}{N_{tot,calc}} < 1.1 \tag{2.12}$$

This filter removed the 2.7% of data, but the comparison between new trends and those prior to the filter application showed a loss of valuable data, especially for particle numbers smaller than $10^4 cm^{-3}$. For future applications, this filter could be weighted by the order of magnitude of the measurements.

Another method to eliminate bad data consisted in discarding all samples featuring a number of particles exceeding the 99-th monthly percentile of each mode. By applying this filter, the 2.6% of data were removed. However, by doing so, months with no bad data lost valuable information, while months with a large amount of bad data were not completely cleaned up. Figure 2.11 shows an example of boxplots which give indications about the monthly statistics of number concentrations for 2006 for each particle mode.
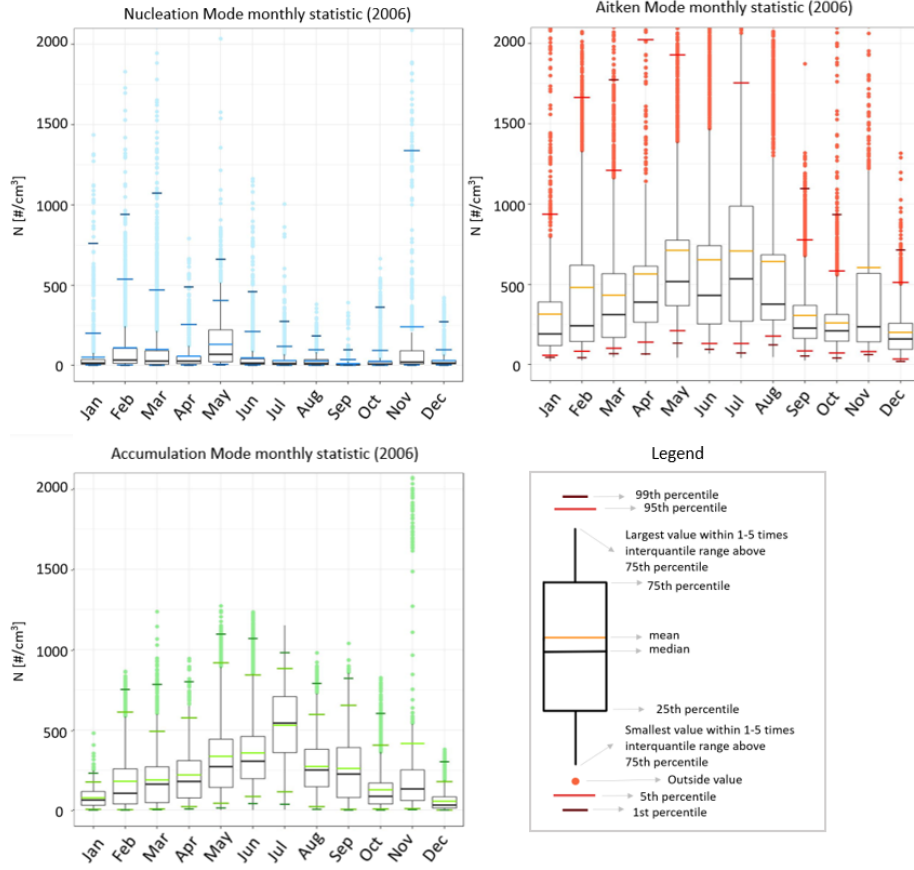
Figure 2.11: Monthly boxplot of number concentrations $[\#/cm^3]$ for every mode for 2006.

Finally, the decision to check data visually with the help of some graphs specially created was taken, so only corrupted samples were rejected. In order to plot the graphs useful for the bad data visualization, firstly the difference between size distribution measured by the DMPS and calculated through the fitting parameters was performed. Since the difference between matrices requires that they have the same size, several R scripts were developed in order to divide the starting heterogeneous data set on the basis of the number of channels and to calculate the size distributions by using the size bins adopted by the instrument, instead of the unique set of 37 size bins.

$$\text{Difference} = \left(\frac{dN_k}{dlogDp_k}\right)_{meas} - \left(\frac{dN_k}{dlogDp_k}\right)_{calc} \tag{2.13}$$

After these operations, I developed a bash script able to generate heatmaps of the daily trend of the differences between size distributions, together with the daily trend of the number concentrations for each mode. Through these graphs it is possible to assess the presence of both a sample for which the difference between measured and calculated size distributions is greater than $10^4 cm^{-3}$ and the corresponding spike in the number concentrations trend. I visually inspected these daily plots one by one

51

checking every sampling time of a bad acquisition in order to later remove it from the raw data. An example of these kind of plots is shown in Figure 2.12.
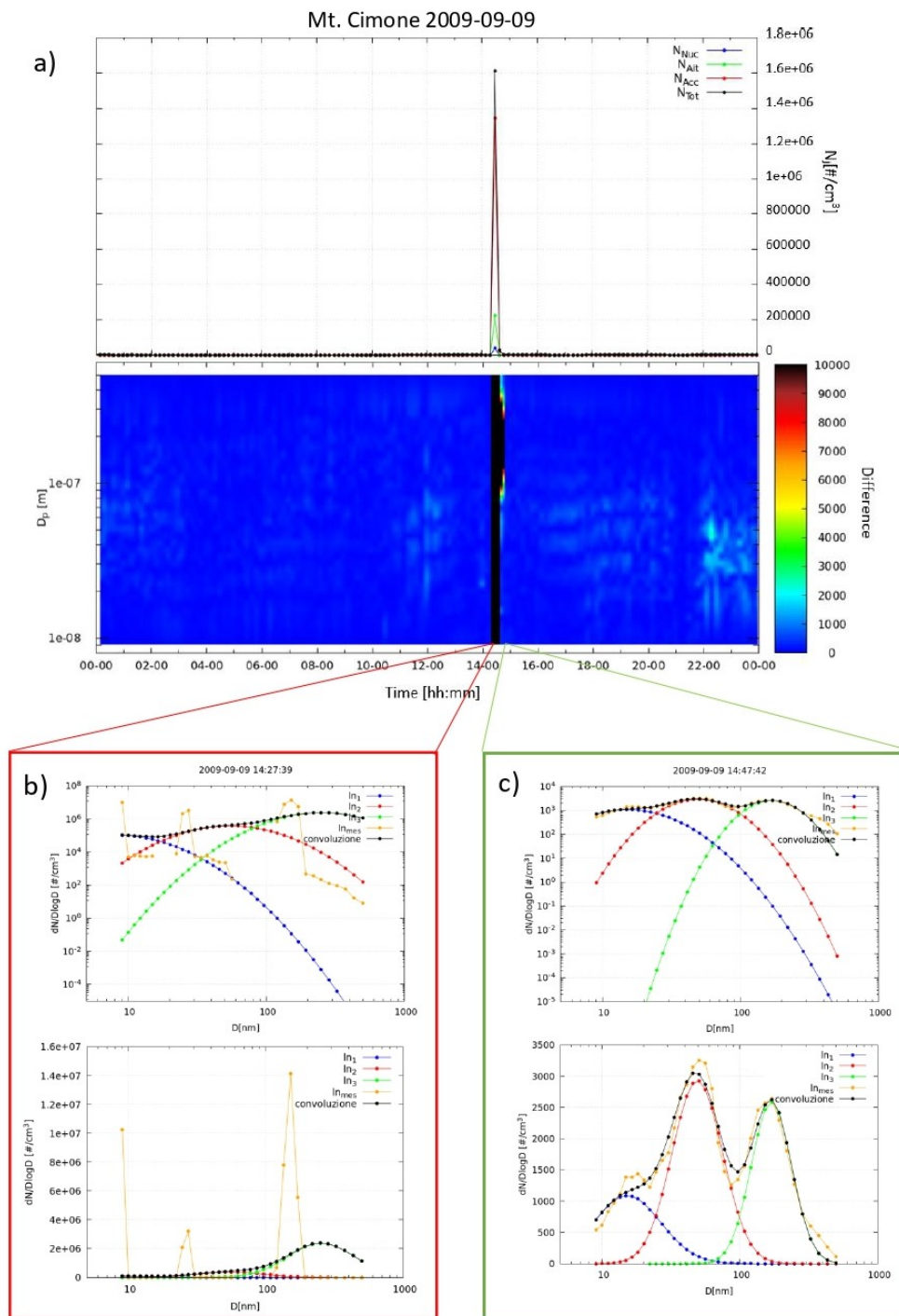
Figure 2.12: a) The upper plot shows the time trend of particle number concentrations for September 9th, 2009. The lower plot shows a heatmap of the time trend of the difference between measured and calculated size distributions. b) Log-log and semi-logarithmic graphs of size distributions for sampling time 14:27:39. c) Log-log and semi-logarithmic graphs of size distributions for sampling time 14:47:42.

In Figure 2.12a, the temporal trends of number concentrations and of the difference between measured and calculated size distributions are plotted together for September 9th, 2009. The red and green markers outline two specific sampling times (14:27:39 and 14:47:42), which measured and calculated size distributions are respectively shown in Figure 2.12b and 2.12c, both in semi-logarithmic and log-log scales. At time 14:27:39, DMPS performed a bad acquisition (the orange dotted line in Figure 2.12b), so the fitting method tried to fit an unreal log-normal size distribution (the black dotted line in Figure 2.12b) and the difference between them is greater than $10^4 cm^{-3}$, while the number concentration reaches an unrealistic value of $1.6 \cdot 10^6 cm^{-3}$. At time 14:47:42, the difference between measured and calculated size distributions assume values of few hundreds and the total number concentration is around 2900 particles per cubic centimeter.

This filtering process removed 1.1% of raw data, leading to an efficient and complete data cleaning. After the removal of outliers, the new homogeneous data set will be the basis of all the studies conducted in this thesis.

2.4   Data Analysis

Once data preprocessing is completed, converting raw data into a clean data set, a series of analyzes are conducted. Firstly, both the particle number trends over the years and the variability of the distributions are studied to figure out whether any periodicity exists. Then, the aim is to identify new particle formation events and to classify them according to Dal Maso et al., 2005. Finally, the new particle formation events featuring a good confidence level are studied by determining some dynamic properties, namely the growth rate, the temporal variation of N_{nuc} and the condensation sink. In the following paragraphs the methods adopted to perform these kind of analyzes are illustrated.

2.4.1   Characterization of atmospheric particle at Mt. Cimone

The analyzes for the characterization of the aerosol population measured at Mt. Cimone are conducted on the basis of several scientific papers found through targeted literature searches. An example is the investigation conducted by Lupi et al., 2016, of the different modal behavior of ultrafine aerosol particles collected at the Gruvebadet observatory located in the island archipelago of Svalbard. An other work which inspired the investigation of both aerosol number concentration and size distribution trends is the long-term characterization of submicron atmospheric particles in an urban background site done by Dinoi et al., 2020, at the Institute of Atmospheric Sciences near Lecce. One last example of approach which influenced my work is the observation made by Tunved, Ström, and Krejci, 2013, of qualitative and quantitative assessment of more than 10 years of aerosol number size distribution data observed in the Artic environment at the Mt. Zeppelin observatory (Ny Ålesund, Svalbard).

In the present thesis, R programming language is used to divide data according to specific periodicities. In particular, all the scripts developed are based on the usage of *openair* and *lubridate* libraries. The first one is an R package developed for the purpose of analysing air quality data, or, more generally, atmospheric composition data, while *lubridate* is an R package that makes it easier to work with dates and times. Finally, all the plots which are reported and described in Chapter 3 are realized by using R scripts, GNUPLOT and Excel.

2.4.2   New Particle Formation events classification

Currently, the most reliable way to classify measurement days into NPF event or non-event days is a visual inspection method proposed by Dal Maso et al., (2005). This method consists in plotting a 1-D time series of the size distributions as flat surface plots. In these plots, the *x axis* represents time, the *y axis* shows the particle

diameter on a logarithmically spaced scale and the *z axis*, which is usually identified by different colors, represents the particle number concentration density. An example of this kind of plots found in literature is reported in Figure 2.13, showing a typical long lasting nucleation event registered in the boreal forest at Hyyttiälä, Finland, for May 19th, 1999.
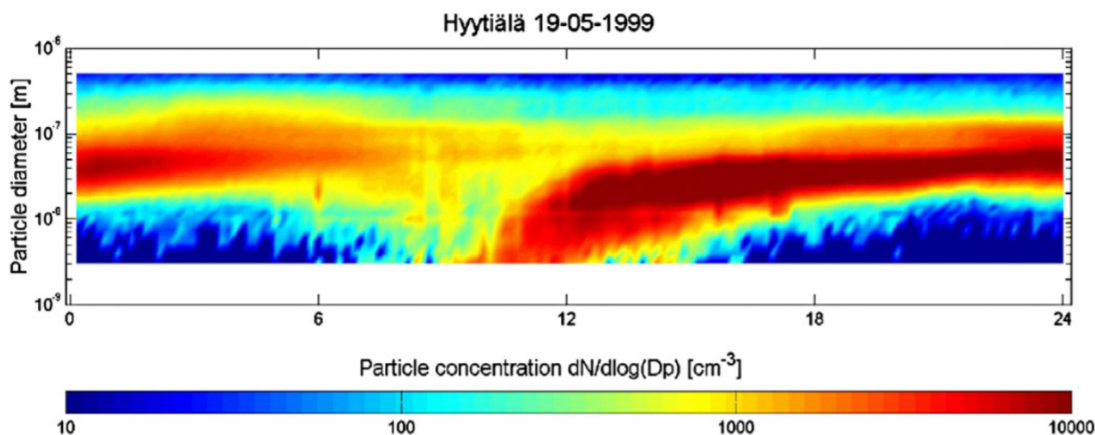
Figure 2.13: Contour plot of the particle concentration as a function of time and particle size for a nucleation event observed in a boreal forest at Hyyttiälä, Finland; 24 hours measurement for May 19th, 1999. Between 9:00 and 12:30 numerous freshly nucleated particles appear at the smallest measurable sizes ($> 3nm$) and grow within hours to sizes of around $50nm$ (Boy and Kulmala, 2002).

The identification of (NPF) events is then conducted using the criteria set by Dal Maso et al., 2005, and later refined by Hirsikko et al., 2007. According to these, a NPF event is considered to occur when:

- a distinctly new mode of particles appears in the nucleation range;

- this new mode prevails for some hours;

- the new mode shows signs of growth.

As well as events, also days with no particle formation, called non-events, are of interest for comparison and control purposes. They are characterized by an absence of particles in the nucleation mode size range, mostly displaying a bimodal size distribution. However, a large number of days did not fulfill the criteria to be classified as either events or non-events. These included days with some sporadic occurrence of particles in the nucleation mode range, or days when we can see the later phase of a mode growing in the Aitken-mode size range. These days were classified as undefined; the purpose of this was to remove them from any analysis comparing event and non-event days. A further classification of NPF events consisted in the distinction between classes I or II events depending on the level of confidence. The good confidence level of class

I events is related to the possibility of retrieving the dynamic properties, such as the particle growth rate (GR) and formation rate (J), of the nucleation mode particles, which will be described in the following paragraphs. Class I (high confidence) is further classified as Ia and Ib, with class Ia containing the events that both present a clear formation of a new mode as well as a distinct growth of this mode, while Ib includes those with a less distinct formation and development.

Class	Description
Ia	Very clear and strong particle formation events, with little or no pre-existing particles obscuring the new formed mode, making them suitable for modelling case studies of NPF events.
Ib	Events with signs of growth from the cluster size, but either the growth is suppressed at a certain size or it presents a gap in the size distribution between smaller particles from the nucleation range, and medium-size particles, which lie into the Aitken range.
II	Less representative events, where the derivation of parameters is not possible, or the accuracy is questionable because of unclear shape.
Non-events	Days with no particle formation, characterized by an absence of particles at the nucleation mode range, showing a bimodal size distribution.
Undefined	Days that did not fulfil the criteria to be classified as either event days or non-event days.

Table 2.1: Data classification of events, non-events, or undefined days, according to Dal Maso et al., 2005, and Hirsikko et al., 2007.

In this work, the daily 1-D time series of the size distributions were plotted by using GNUPLOT. The code was adapted in order to print the heatmaps together with the daily temporal variation of number concentrations and the temporal evolution of the geometric mean diameters for each mode, making the classification easier. The latter was made conducing a triple blind method following the criteria described above and summarized in Table 2.1. We analyzed the data visually on a day-to-day basis: each 24-hour period, from midnight to midnight, was classified according to whether it contained a new particle formation event. The purpose of triple-blinding procedures is to reduce assessment bias and to increase the accuracy and objectivity of outcomes. Finally, the three classifications were compared and the uncertain days were set by mutual agreement.

2.4.3 Growth rate calculation

The particle growth rate is defined as the rate of change in the diameter, Dp, that represents the growing particle population:

$$GR = \frac{dDp}{dt} \tag{2.14}$$

While investigating through literature researches, I found several detailed ways of deriving the growth and formation rates. For instance, Arneth et al., 2016, suggested to calculate GRs from log-normal modes fitted to the measured particle size distribution following Hussein et al., 2005. The modal geometric mean diameter Dp_g obtained as a result of the fitting procedure, is a good choice for growth rate analysis. In a log-normally distributed population Dp_g is also the median diameter (Seinfeld and Pandis, 2016), meaning that the majority of the particles are of a size close to Dp_g. The time evolution of Dp_g was inspected visually, and the GR was determined with linear least squares fitting to these peak diameters whenever a continuous increase in diameter was observed. An example of application of this method is shown in Figure 2.14, where the size distribution measured at the research station Spasskaya Pad (Yakutia) over the course of a day is shown. The temporal change of these diameters is represented with black lines from which the growth rate is calculated.
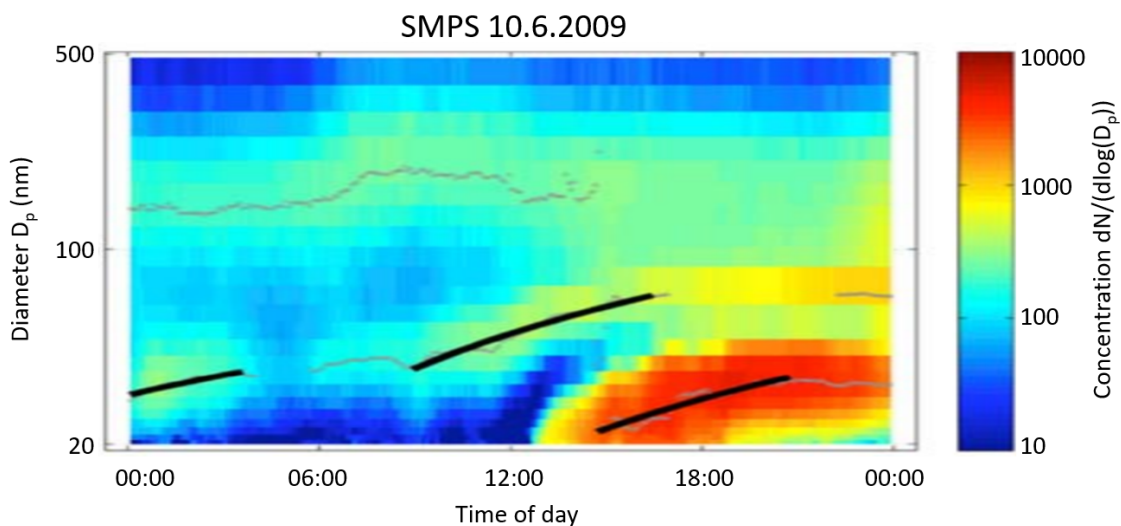
Figure 2.14: Particle growth rates obtained from particle number size distribution measured at the research station Spasskaya Pad (Yakutia), example from 10 June 2009 (Arneth et al., 2016).

The method adopted in this thesis to derive the newly formed aerosol population growth dDp_{nuc}/dt is inspired by the one described above, except for the visual inspection, which was replaced by an automated process performed by a new algorithm.

The latter was implemented with a script developed in R language, and first of all it performs a smoothing of both the nucleation number concentration N_{nuc} daily trend and the mean geometric diameter Dp_{nuc} daily trend through a moving median algorithm in order to reduce the fluctuations. Then, it is able to automatically identify the time interval in which the growth of both N_{nuc} and Dp_{nuc} occurs. Moreover, by calculating the slope of a regression line performed over the growth intervals, the value of grow rate $GR = dDp_{nuc}/dt$ and the time evolution of nucleation particle number concentration dN_{nuc}/dt can be found in a reproducible manner.

An example of plot resulting from the application of the algorithm is shown in Figure 2.15. In the upper panel the time evolution of nucleation number concentration is smoothed through the moving median algorithm. The green vertical lines mark the initial time and the final time of N_{nuc} growth. The red line is the linear regression, the slope of which represents dN_{nuc}/dt. In the central panel the original and smoothed temporal evolution of the modal geometric mean diameter Dp_g are reported. The black line shows the $Dp = 25nm$ limit. The growth range is identified by the green lines and the linear regression is red. The slope of the latter represents the growth rate, $GR = dDp_{nuc}/dt$.
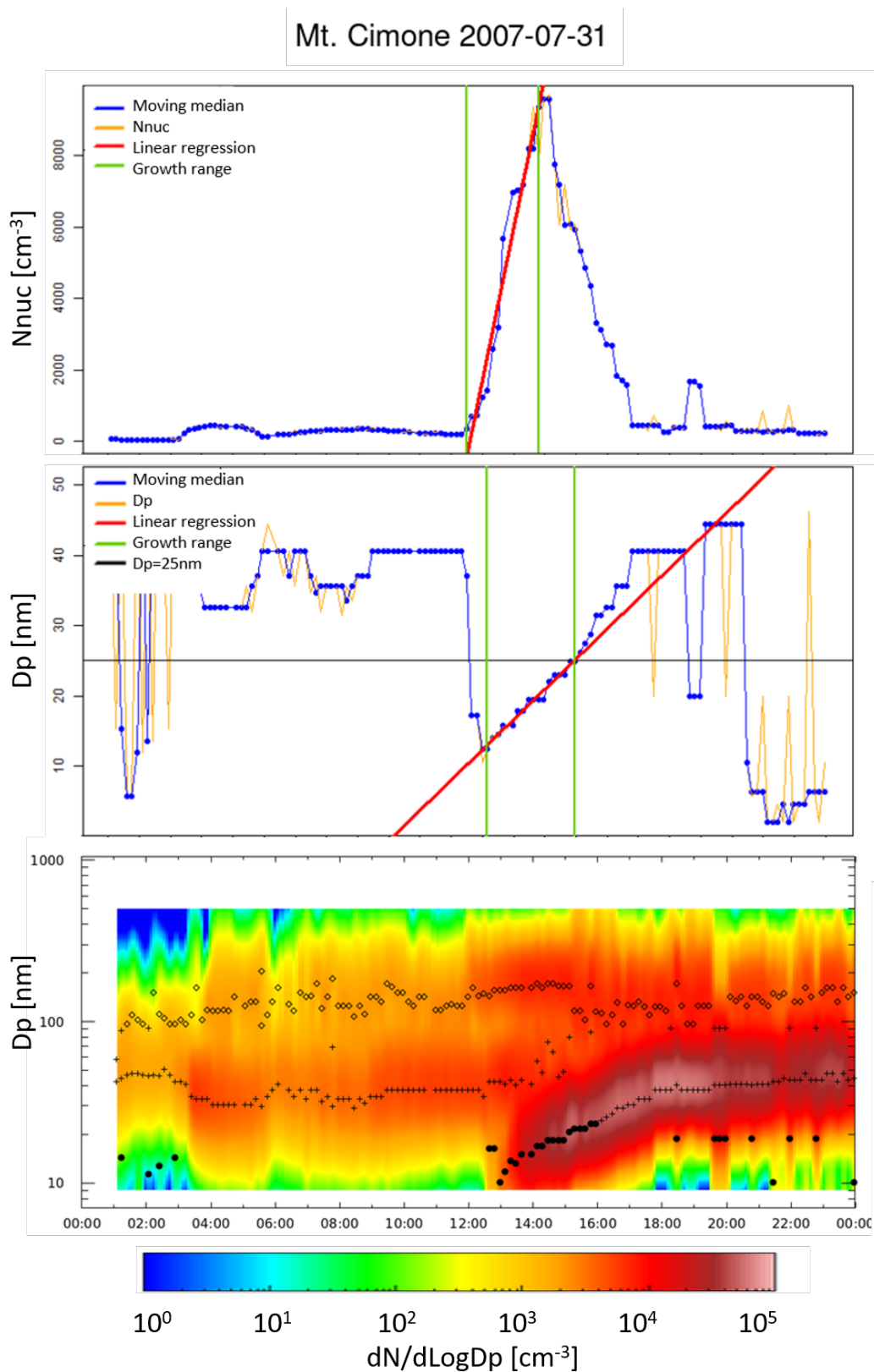
Figure 2.15: Plot resulting from the application of the algorithm developed in order to find $GR = dDp_{nuc}/dt$, dN_{nuc}/dt, and the beginning and ending times of both the growths.

2.4.4 Formation rate

The definition of formation rate by Kulmala et al., 2012 is derived from the equation of the time evolution of particle number concentration, N_{Dp}, in the size range $[Dp, Dp + \Delta Dp]$, which is described in general terms as:

$$\frac{dN_{Dp}}{dt} = \text{production} - \text{losses} = J_{Dp} - losses \tag{2.15}$$

where the new particle formation rate at size Dp is the production term, denoted by J_{Dp}. The loss terms include coagulation losses due to larger aerosol particles and condensational growth out of the considered size range. Wall and other surface losses need to be considered when analyzing, for example, chamber measurement data, but in atmospheric observations such losses can usually be neglected. By reorganizing Equation 2.15, and by including the loss terms, the neutral particle formation rate is defined as:

$$J_{Dp} = \frac{dN_{Dp}}{dt} + F_{coag} + F_{growth} \tag{2.16}$$

where F_{coag} is the flux due to coagulation losses, and F_{growth} is the flux of particles growing out of the nucleation mode size range according to Dal Maso et al., 2005, which also calculated the as:

$$F_{growth} = \frac{GR}{\Delta Dp} \cdot N_{nuc} \tag{2.17}$$

$$F_{coag} = CoagS \cdot N_{nuc} \tag{2.18}$$

where N_{nuc} is the number concentration of nucleation mode particles, while the sum $\sum_j K_{ij} N_j$ is the coagulation sink $CoagS$. According to Kulmala et al., 2012, $CoagS$ for particles with diameter Dp can be calculated from the measured size distribution:

$$CoagS_{Dp} = \int K(Dp, Dp')n(Dp')dDp' \simeq \sum_{Dp'=Dp}^{Dp'=max} K(Dp, Dp')N_{Dp'} \tag{2.19}$$

where K(Dp,Dp') is the coagulation coefficient of particle sizes Dp and Dp'. The $CoagS$ is related to the condensation sink CS (Kulmala et al., 2001), defined as the rate at which condensable vapors condense on existing particles, through the following equation:

$$CoagS_{Dp} = CS \cdot \left(\frac{Dp}{0.71}\right)^m \tag{2.20}$$

where Dp is the diameter expressed in *nm*; *m*, according to Lehtinen et al., 2007, has a value, depending on the background distribution, between -1 and -2, and 0.71 is

the diameter of sulphuric acid hydrate, since CS is typically estimated by using H_2SO_4 as the condensing molecule. Indeed, by assuming that the condensable vapor is solely H_2SO_4, the condensation sink can be estimated as:

$$CS = 2\pi D \sum_i \beta_{m,i} N_i Dp_i \tag{2.21}$$

where D is the diffusion coefficient of H_2SO_4 equal to $0.104 cm^2 s^{-1}$, while β_m represents a transition-regime correction (Kulmala et al., 2012):

$$\beta_m = \frac{1 + Kn}{1 + 1.667 Kn + 1.333 Kn^2} \tag{2.22}$$

defined as a function of the Knudsen number, $Kn = 2\lambda/Dp$, where $\lambda = 123nm$ is the gas vapour molecule mean free path (Erupe et al., 2010).

In the present work the condensation sink was computed starting from the number particle size distribution for each sampling time from November 2005 to July 2013. This values will be the basis for the future calculation of the formation rate for new particle formation events observed at Mt. Cimone.

Chapter 3

Results

In this chapter, the main results of the studies conducted following the procedures previously described are illustrated.

First of all, a description of the data set obtained through the preprocessing is reported in order to understand the quantity of data available for the analyses. Then, the properties of the aerosol population measured at Mt. Cimone are investigated by outlining the diurnal, monthly, seasonal, and interannual differences in size distributions and number concentrations. This long-term characterization at CMN meets the clear need to document the variability of climate-relevant in situ aerosol properties from all sites connected to the GAW network. For this reason, the total aerosol number concentration recorded at CMN is compared with that observed at other stations in a global context. This is possible thanks to the paper published by Laj et al., 2020, where a great effort was made to define a fully traceable ground-based aerosol measurements network.

Finally, the observations of new particle formation events are studied. In particular, after some examples of days that have been classified by visual inspection, the frequency of events is assessed on a seasonal and annual basis. Then, some characteristics of class Ia events, namely growth rate, nucleation number concentration time evolution, and condensation sink are analyzed. To conclude, CMN characteristics of new particle formation events are compared to those observed at other high altitude ground-based sites thanks to the paper published by Sellegri et al., 2019, where gathered information from experimental NPF studies performed at high altitude provided an overall picture of the frequency of occurrence of the process and of some events features.

3.1 Dataset properties

Although the aim was to keep the measurements continuous, some gaps in the dataset inevitably occurred due to instrument failure, maintenance operations of the DMPS, and other unforeseen events. Based on 281 574 samples of aerosol size distribution every 10 minutes, the hourly averaged dataset covers 71.6% of the time from November 2005 to July 2013. The total sampled days are 2 174. Figure 3.1 displays the acquisitions performed every year from 2005 to 2013, and a table illustrating the percentage of available months, days and hourly averaged samples. Those percentages are reported for every year and for the whole acquisition period of almost 8 years.

	Months (% per year)	Days (% per year)	Hourly averaged samples (% per year)
2005	16.7	8.8	7.7
2006	100	69.9	63.8
2007	91.7	82.2	77.3
2008	83.4	60.0	51.0
2009	100	86.8	80.2
2010	100	80.5	72.9
2011	100	86.8	81.9
2012	100	87.4	80.5
2013	58.4	40.5	37.8
Total (% per 8 years)	93.8	75.4	69.1
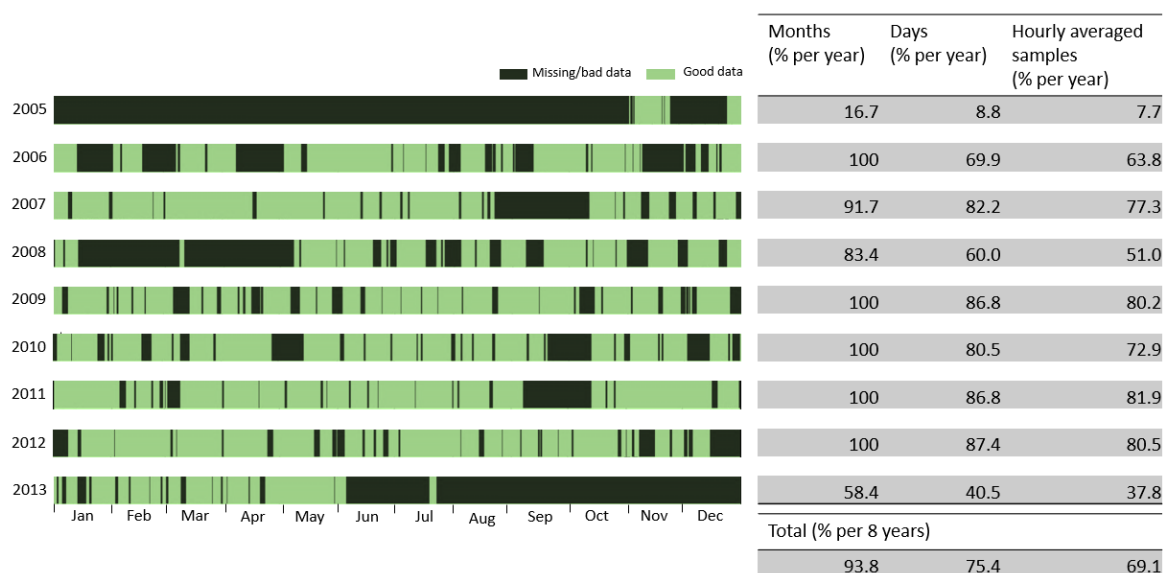
Figure 3.1: On the left a timeline shows lack of data due to missing measurements or removed outliers (black) and good measurements (light green) for every year from 2005-2013 at CMN. On the right a table reports the percentage of available months, days, and hourly averaged samples for every year over the whole acquisition period.

From Figure 3.1, the observation started in November 2005 and ended in July 2013. Moreover, large parts of data for 2007 and 2008 are missing due to problems and need of maintenance on the instrument. Nevertheless the data availability allows to strongly characterize the whole period, investigating the annual, seasonal and diurnal variations of the aerosol number size distributions at CMN.

A complete visualization of the data available to conduct climatological and new particle formations studies, is reported in Figure 3.2. The latter shows a 1-D plot with hourly averaged aerosol number size distributions as a function of time, from November 2005 to July 2013.
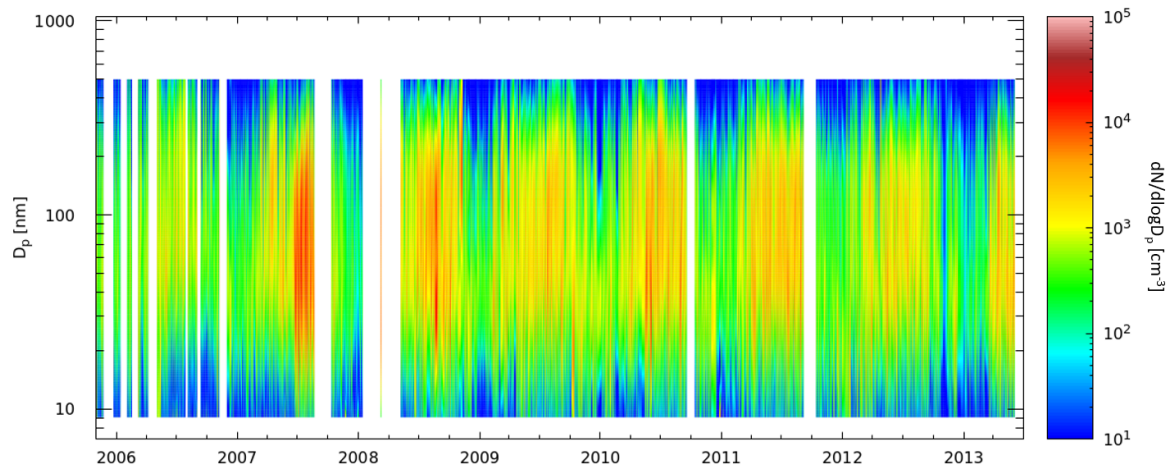
Figure 3.2: Spectral plot of hourly averaged aerosol number size distributions measured at CMN, from November 2005 to July 2013.

3.2 Long-term characterization of Aerosol population at Mt. Cimone

3.2.1 Average size distribution properties

Figure 3.3 shows the median aerosol number, surface and volume size distributions for the studied period of November 2005-July 2013.
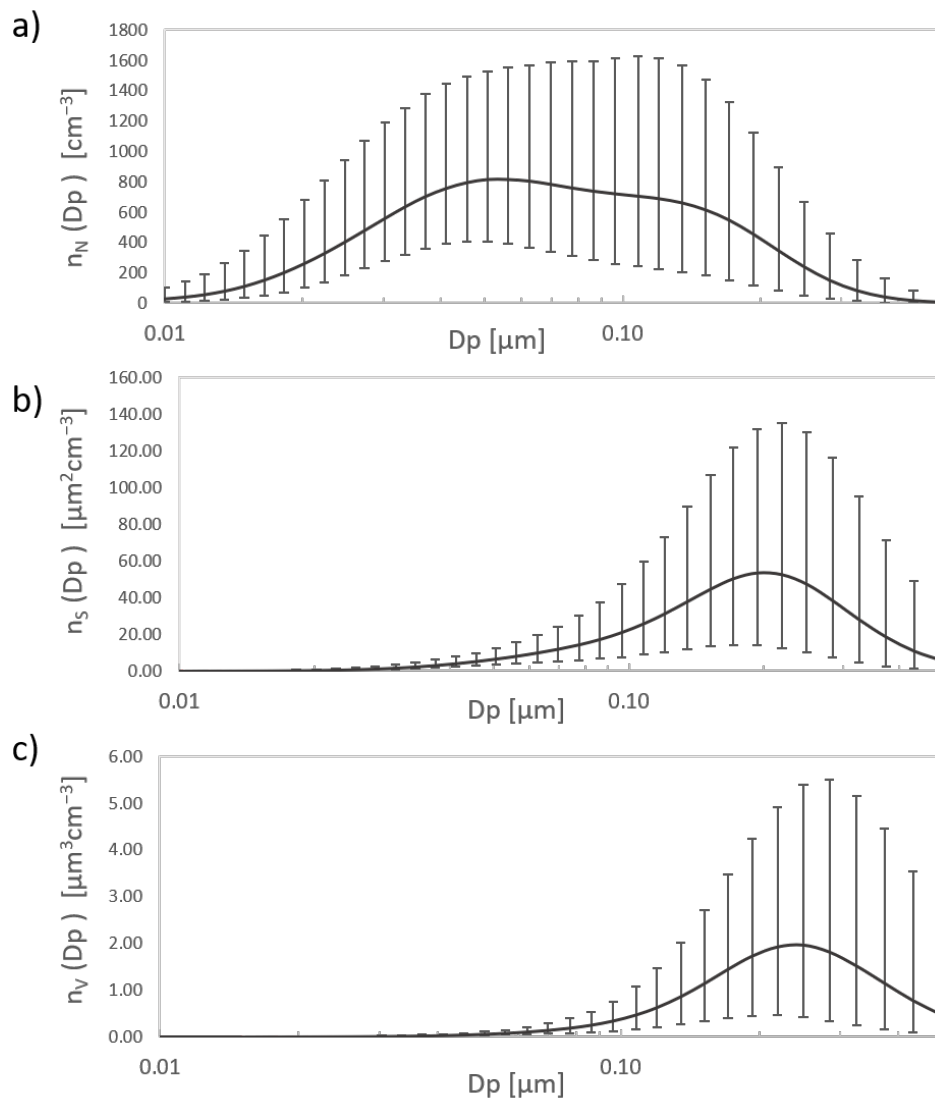
Figure 3.3: Typical median aerosol size distributions of CMN, from November 2005 to July 2013. a) Number size distribution, b) Surface size distribution, c) Volume size distribution. 25-75th percentile ranges indicated by vertical bars.

The typical median number size distribution (Figure 3.3a) is bimodal with the occurrence of one mode in the Aitken range and one mode in the accumulation size range. On average, the Aitken mode number concentration dominates the number

size distribution, and peaks around $66nm$. The median aerosol surface distribution (Figure 3.3b) is defined by roughly a single mode in the accumulation size range with the maximum peak located around $193nm$. Even the median volume size distribution (Figure 3.3c) can be described by a mono modal shape that peaks at around $249nm$. It is known that the number distributions are important for microphysical processes, for which, typically, both Aitken and accumulation range contributes at CMN, while volume size distribution (important for air quality issues and linked to the mass concentration) as well as the surface size distribution (crucial for optical properties and light attenuation) are mainly linked to accumulation particles.

The statistic of aerosol number size distribution fitted modal parameters is summarized in Table 3.1. First of all, it is important to point out that the mean value of N_0, which is reported within brackets, for the nucleation mode is extremely high due to the mathematical algorithm performing the best fit of measured data. Sometimes, the algorithm tries to best fit the measured data by locating a nucleation mode outside the measurable range of the instrument and setting an extremely high value for the mode number concentration. It is also the reason why the nucleation mode size between $7nm$ and $20nm$, while the instrument measures only particles greater than $9nm$. The Aitken mode, instead, is well identified and it is the most dominating mode, typically located between $37nm$ and $61nm$, with a median modal concentration of $443cm^{-3}$. The accumulation mode has a typical median concentration of $270cm^{-3}$ and modal size between $127nm$ and $181nm$. Episodically, high particle concentrations in the different modes do occur, causing high mean values compared to the median. These events are likely caused by either new-particle formation events, indicated by the comparably high concentration of nucleation mode particles, or episodes of long-range transport in the case of high concentration of accumulation mode.

	N_0 (cm^{-3})	σ_g	Dp_g (nm)
Nuc	117 [1.5E12] {33-470}	1.75 [1.70] {1.50-1.89}	16 [14] {7-20}
Ait	443 [790] {215-883}	1.63 [1.64] {1.51-1.75}	47 [51] {37-61}
Acc	268 [735] {84-663}	1.50 [1.53] {1.40-1.62}	148 [163] {127-181}

Table 3.1: Median modal properties of the aerosol number size distribution as observed at CMN, from November 2005 to July 2013. Mean values within square brackets, 25–75th percentile range within curly brackets. (N_0, cm^{-3}) is the modal number concentration, (σ_g) is the modal geometrical standard deviation, and (Dp_g, nm) is the modal geometrical mean diameter.

3.2.2   Seasonal variation of the aerosol size distribution properties

The typical annual trend of hourly averaged size distribution in Figure 3.4 is derived by the 7.5 years of data observation at CMN.
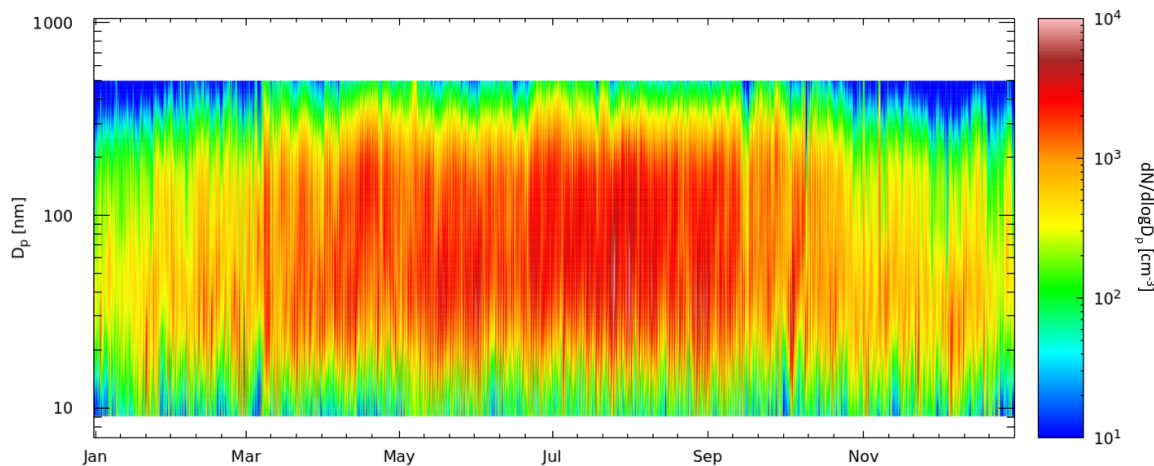
Figure 3.4: The typical year of hourly averaged size distribution at CMN, from November 2005 to July 2013.

In this plot a clear difference between fall/winter and spring/summer is evident, with a general increment of the number concentration for each mode during the warmer seasons. Indeed, the lowest number concentration is found in January and December whilst the highest number concentration is found in July and August. Moreover, we can observe quite negligible fraction of larger accumulation sizes in winter months, with maxima at lower diameters, with respect to other seasons. It is also evident that the changes of aerosol number size distribution occur gradually and the transitions between the seasons are smooth, quite opposite to the seasonal characteristics of, for instance, the Arctic site Zeppelin (Tunved, Ström, and Krejci, 2013). In order to better highlight this differences, firstly the month by month variation is analyzed, and finally, the comparison between seasons is investigated.

Figure 3.5 shows monthly median and mean number, surface and volume size distributions emphasizing a strong seasonality. The surface and volume size distributions are both characterized by mono-modal curves. The averaged number size distribution, instead, is bimodal for every month, with one mode in Aitken and one in the accumulation size range, as shown in Figure 3.5b.
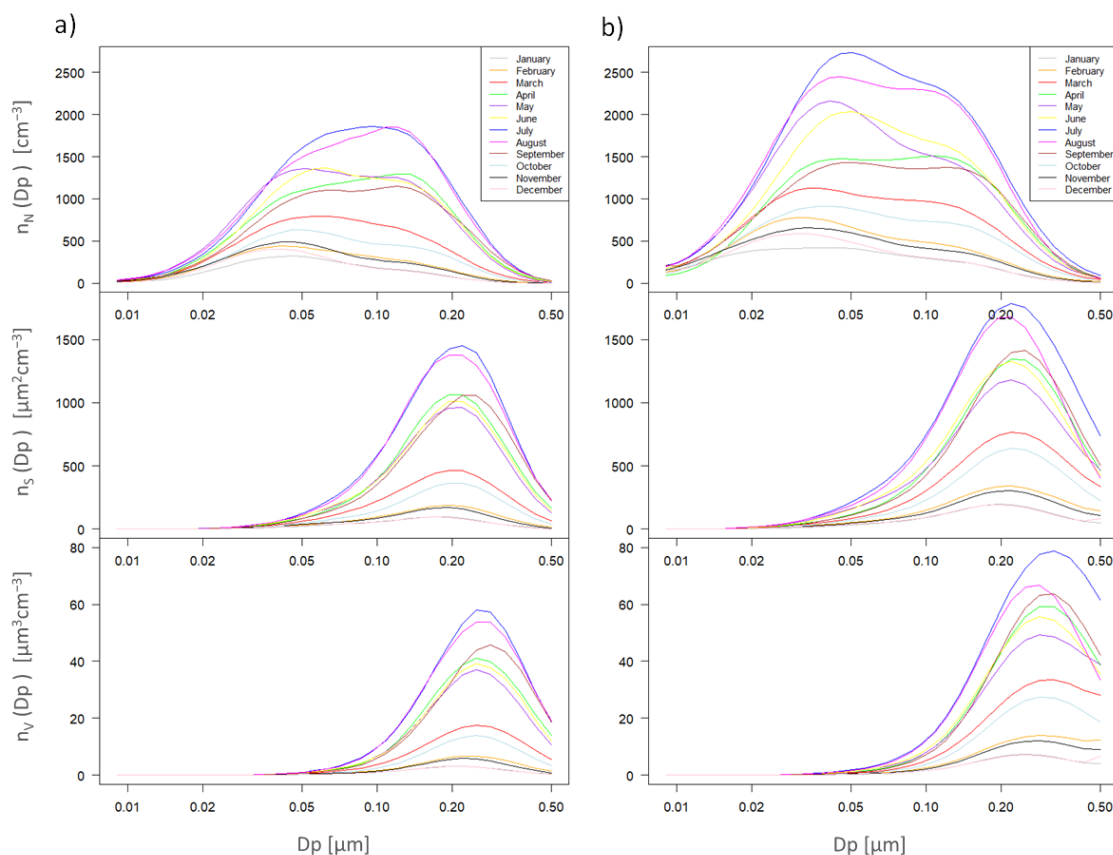
Figure 3.5: Monthly median a) and mean b) number ASD, surface ASD and volume ASD at CMN over the whole period from November 2005 to July 2013.

The greatest variability in monthly and seasonal number size distribution concerns the Aitken particles mode, which increases distinctively from winter months (DJF) to summer months (JJA) (Figure 3.6). Moreover, during the transition from cold to warm season, Aitken peaks swipe from $30nm$ to a larger size of $50nm$. Even the accumulation number concentration increases in the same way, suggesting a possible contribution of aged polluted particles from the underlying Po Valley while the average particles diameters of accumulation peaks decrease from around $150nm$ to $120nm$.
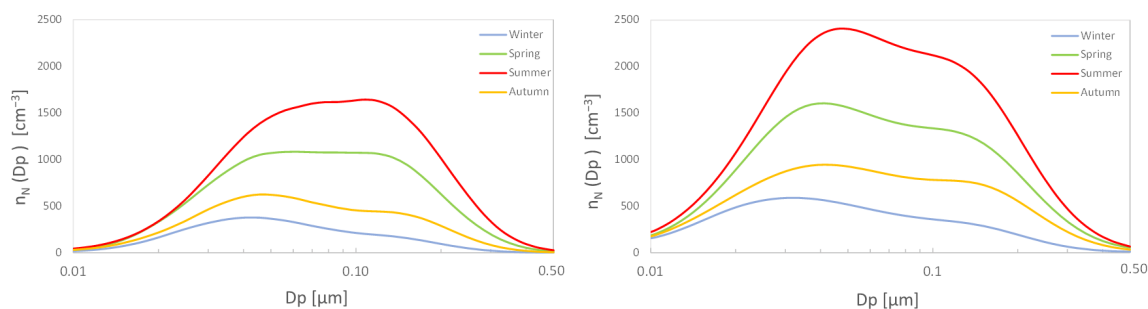
Figure 3.6: Median and mean number ASD during different seasons at CMN, from November 2005 to July 2013.

The spring period is fairly similar compared to the summer period, although the number concentration is slightly smaller and the same similarity can be found comparing autumn and winter months respectively.

Moving on, since the log-normal distribution is asymmetric, median values differ from mean ones. In particular, by comparing Figure 3.5a and Figure 3.5b, or the two graphs in Figure 3.6, the main difference is that median values are always smaller than mean ones. This is valid especially for the Aitken mode, because mean values are influenced by new particle formation events and growth of nucleation particles.

3.2.3 Overview of number particle concentration

To investigate the contribution of the different size fractions to the total particle number concentrations, we consider three different groups of DMPS's channels: nucleation $9.05nm < N_{nuc} < 24.7nm$, Aitken $24.7nm < N_{Ait} < 96.4nm$ and accumulation $96.4nm < N_{acc} < 600nm$. The total number concentration, N_{tot} is the sum of the three modes. During the years of NPSD observation, number concentrations exhibit a quite regular increase during the warm seasons and a decrease in the cold periods, as expected for high altitude background conditions. The monthly variability of N_{nuc}, N_{Ait}, N_{acc} and N_{tot} is reported in Figure 3.7.
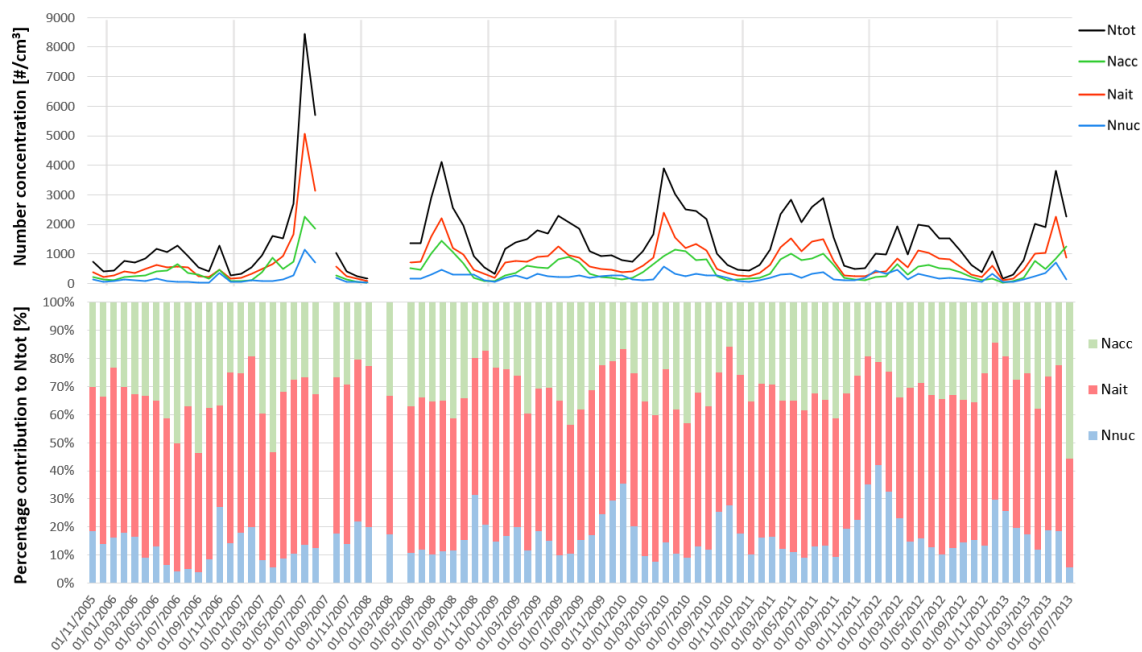
Figure 3.7: Upper panel shows monthly variation of particle number concentrations at CMN, form November 2005 to July 2013. The blue, red and green lines represents nucleation, Aitken and accumulation modes respectively. Lower panel represents the monthly percentage contribution of each mode to total number concentration.

In this study the particles in the Aitken mode are, on average, the main contributor to

N_{tot}, with the 53% (36-62%), followed by particles in the accumulation and nucleation modes with 31% (14-56%) and 16% (4-42%), respectively, throughout the observation period. The monthly percentage contributions to total number concentration of each mode are represented by the coloured columns in the lower panel of Figure 3.7. The percentage contributions vary greatly over a typical year. The accumulation mode undergoes a great seasonal variation since its number concentration strongly decreases during winter months, when the measurement site is representative of free troposphere conditions.

Absolute values of monthly averaged number concentration, from which percentages are calculated, are represented by coloured lines in the upper panel of Figure 3.7. The descriptive statistics for each mode is illustrated in Table 3.2. High values of N_{tot} occurred especially in the summer, i.e. July 2007, when it was reached the longest and most significant peak, with a monthly average of $N_{tot} = 8461 cm^{-3}$. During this specific month, every mode reached the maximum averaged values over the entire period. The minimum number concentrations were recorded during winter, i.e. January 2008 with an average of $N_{tot} = 147 cm^{-3}$.

	N_{tot} $[cm^{-3}]$	N_{nuc} $[cm^{-3}]$	N_{Ait} $[cm^{-3}]$	N_{acc} $[cm^{-3}]$
Mean	1535	221	811	502
SD	1332	193	753	437
Median	1120	177	591	381
75th percentile	1988	287	1007	733
25th percentile	653	103	360	182
Min	147	22	84	33
Max	8461	1146	5058	2257

Table 3.2: Descriptive statistics of the monthly averaged number concentrations at CMN (November 2005-July 2013).

3.2.4   Seasonal variation of the number concentration

A deeper analysis of the seasonal pattern is represented in Figure 3.8, where the seasonality of the three modes is shown. Clearly, the total number of particles annual variation is driven by Aitken particles, followed by the accumulation particles, showing very similar behavior. Both N_{Ait} and N_{acc} show an increase starting in early spring, reaching a relative maximum in April and the main maximum in July; a rapid decrease is than observed between August and September. Nucleation particles do not show typical seasonal variation in the median value. The mean value is above the 75-th centile almost every month. This means that some occasional bursts of small particles influence the average number concentration. A sudden burst of high concentrations of

nucleation particles identifies a new particle formation event (NPF). The most intense NPFs take place in summer, as denoted by large upper percentiles. May seems to be a very active month for NPF, since a second maximum is observed. The mean and median trends of the accumulation mode, on the contrary, are very similar, meaning that there are no significant bursts of aged particles.
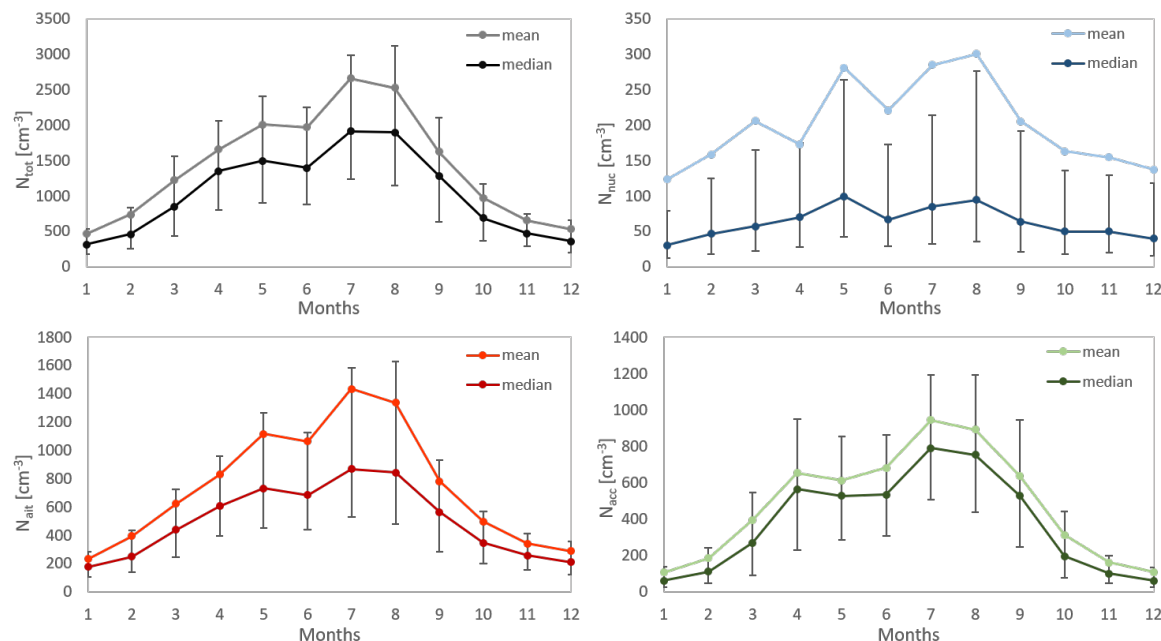
Figure 3.8: Annual average variation of median and mean integrated number concentrations per month at CMN (November 2005–July 2013). 25-75th percentile ranges indicated by vertical bars. For each mode a different scale of number concentration is adopted.

Seasonal averages ±1 standard deviation and medians with 25th and 75th percentiles are also calculated starting from the hourly averaged size distributions. They are summarized in Table 3.3 for each size range. The average total concentration is smallest during winter, with 582 particles per cubic centimeter, then it increases during spring of around 1000 particles per cubic centimeter, reaching the maximum in summer with 2400 particles per cubic centimeter. After the warmer months, the total concentration starts to decrease with a difference of around 1300 particles per cubic centimeter between summer and autumn. Every mode presents the same seasonal trend of the total concentration, although nucleation mode shows, on average, a smaller variability. The difference between the averaged nucleation particles concentration during winter and summer is only 70 particles per cubic centimeters. Accumulation concentration, instead, shows a great variability reaching an average value of 840 particles per cubic centimeter in summer and only 133 particles per cubic centimeter during winter, smaller than nucleation mode. The large upper percentiles of nucleation mode and the very high mean trend with respect to the median one testify the presence

of NPF events which take place over the whole typical year, especially during May, July and August.

	Spring	Summer	Autumn	Winter
N_{tot} $[cm^{-3}]$	(1606±746)	(2400±1147)	(1092±720)	(582±361)
	1503 (1092-1959)	2154 (1652-2858)	876 (595-1365)	482 (365-681)
N_{nuc} $[cm^{-3}]$	(216±213)	(273±355)	(176±223)	(145±195)
	139 (80-274)	159(88-314)	112 (68-195)	83 (47-158)
N_{Ait} $[cm^{-3}]$	(837±458)	(1287±747)	(546±379)	(303±170)
	734 (541-1010)	1091 (817-1490)	434 (311-646)	258 (194-358)
N_{acc} $[cm^{-3}]$	(554±247)	(840±247)	(370±269)	(133±79)
	536 (373-711)	818 (629-1029)	283 (152-532)	116 (76-172)

Table 3.3: Seasonal average ± 1 standard deviation and median (25th-75th) percentiles of the total, nucleation, Aitken, and accumulation number concentrations at CMN (November 2005-July2013).

3.2.5   Diurnal cycle of the number concentration

The daily patterns of particle number concentrations is shown in Figure 3.9, for every season. For each mode, a different scale of number concentration is used.
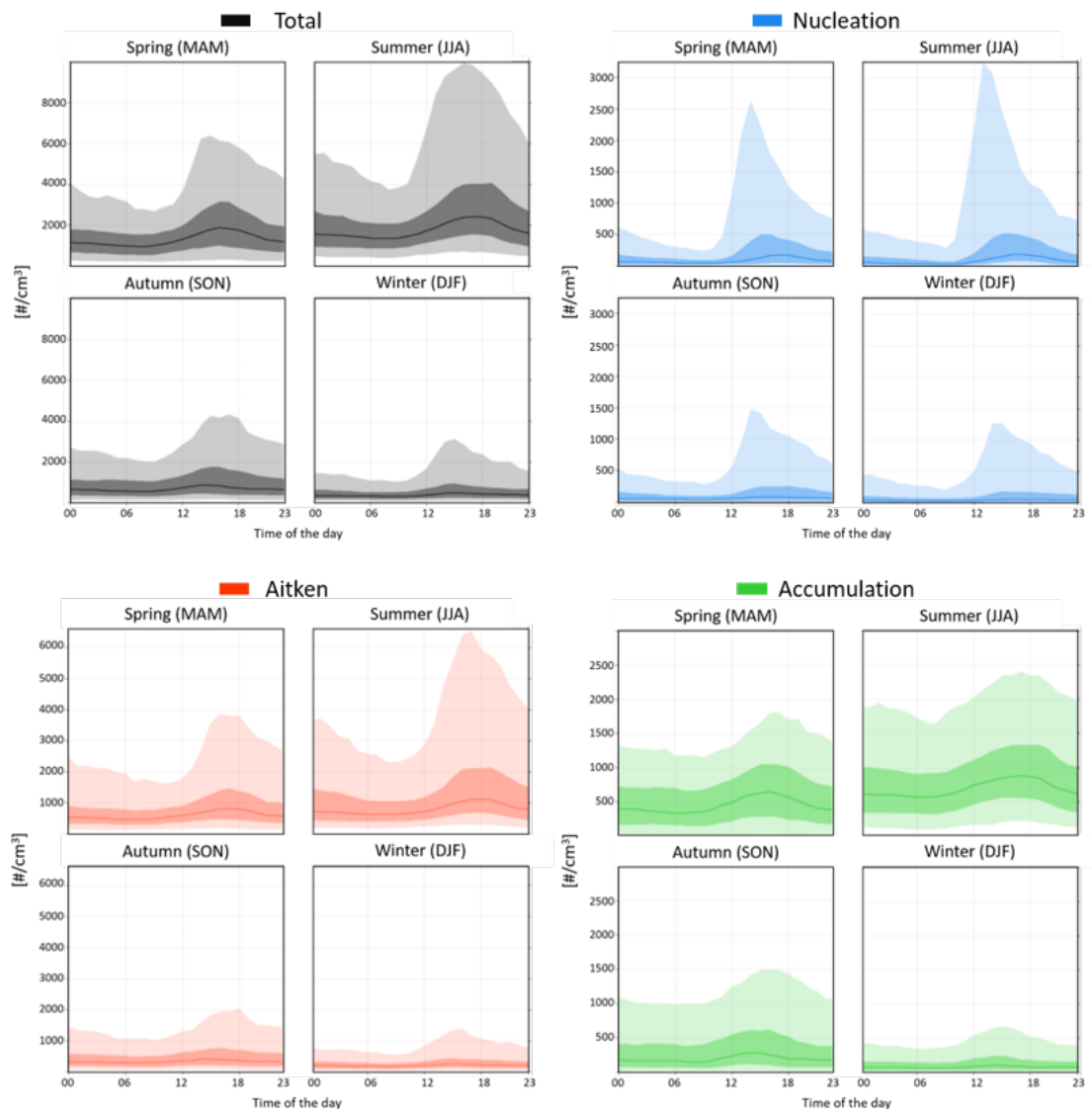
Figure 3.9: The typical diurnal behaviour for different seasons of nucleation, Aitken and accumulation mode number concentration $[\#/cm^3]$ at CMN (November 2005-July 2013). The curve represents median values with the 25-75th (dark colors) and 5-95th (pale colors) percentiles. For each mode a different scale of number concentration is adopted.

Each size range shows a different daily pattern with some changes between the cold and warm seasons. The maximum of total particles occurring in the afternoon is associated with the increase of both Aitken and accumulation fractions, generally observed between 17:00 and 18:00. On the other hand, nucleation concentrations get to maximum value around midday (i.e. 13:00-14:00). During wintertime, the

accumulation and Aitken afternoon peaks are negligible, but the typical behavior at 75th centile shows a weak peak earlier than in summer (15:00-16:00). The nucleation mode testifies the presence of NPF with a frequency that is relatively high in spring and summer. However NPF occurs also during autumn and winter, even if less frequent and less intense with respect to spring and summer.

3.2.6 Diurnal characteristics of aerosol number size distribution

The 1-hour averaged data set including all the data from November 2005 to July 2013 was split into 12 monthly subsets, in order to reveal any systematic variation of the size distribution as a whole, over a 24h cycle. This is reported in Figure 3.10, together with the fitted geometric diameters, superimposed as little black squares; the fitted geometric diameters are evaluated with the same algorithm as described in paragraph 2.3.1.
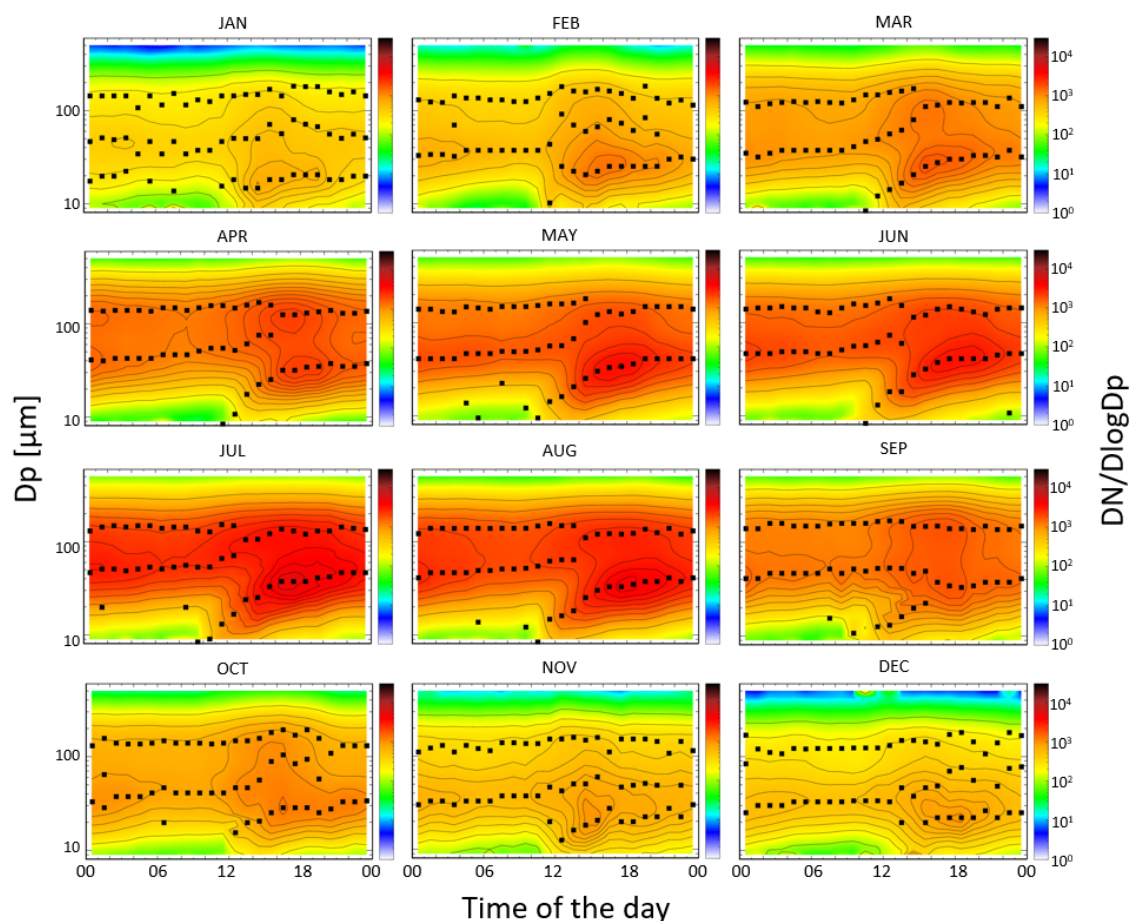
Figure 3.10: Monthly diurnal variation of the averaged NPSD together with the fitted geometrical diameters at CMN (November 2005-July 2013).

During January the average day is characterized by a persistent accumulation mode, while Aitken and nucleation modes show a certain variation having a maximum number concentration around noon. In February and March the behavior of Aitken and nucleation modes starts to be more pronounced. In March, in particular, the new particle formation pattern becomes clearly evident starting around midday, when the solar radiation is maximum, followed by growth which is visible also during the following day. These evidences are preserved and enhanced during the following months of April-May-June, when the averaged data show typical signs of new particle formation and growth. Newly formed particles are able to grow into a size range large enough to allow survival of particles and, therefore, any diurnal variation in Aitken mode particles is masked. The growth of new formed particles allows them to reach the size of cloud condensation nuclei, being a source of lasting particles able to impact climate. The colours representing the density concentration gradually darken through yellow in winter to orange in spring before bright red in summer months (see Figure 3.10). This is due to the seasonal variability of number concentration of each mode, which is maximum during warm months, as already seen in the previous paragraphs. Entering September, the signs of nucleation are diminished. This continues to be the case during the rest of the autumn/winter months, when the nucleation mode grows without exceeding $25nm$, so that diurnal Aitken mode variation is again recognizable.

3.2.7 Number concentration at Mt. Cimone towards a global context

Laj et al. published in 2020 a paper entitled *A global analysis of climate-relevant aerosol properties retrivered from the network of Global Atmosphere Watch (GAW) near-suface observatorie*, in which high-quality data from almost 90 stations worldwide (Figure 3.11) have been collected and controlled for quality and are reported for a reference year. The scope of the paper was to provide a very extended and robust view of the variability of climate relevant in-situ aerosol properties (namely wavelength dependent particle light scattering and absorption coefficients, particle number concentration and particle number size distribution) from all sites connected to the Global Atmosphere Watch network.
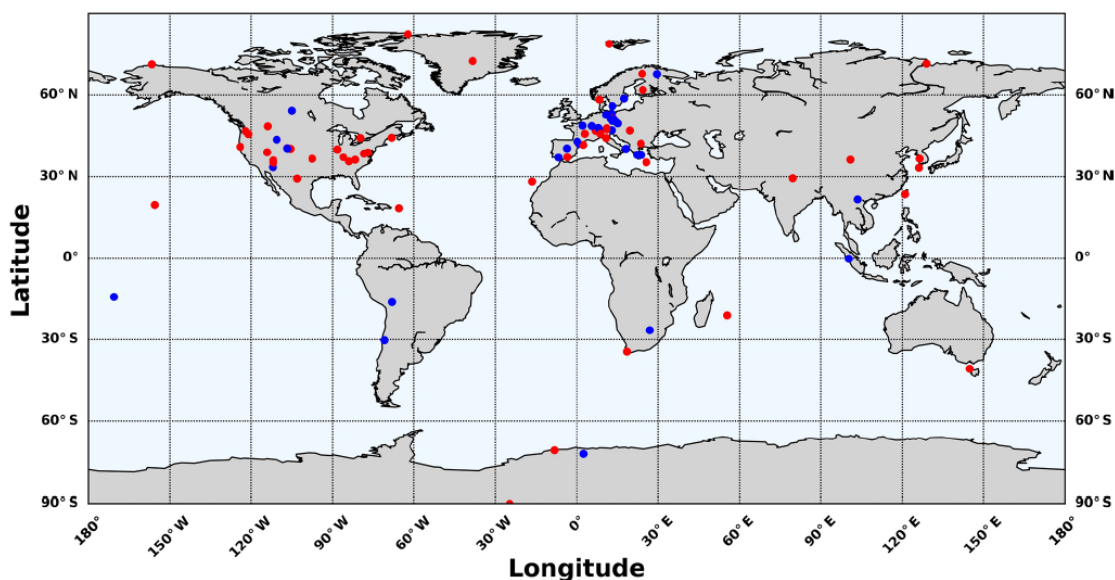
Figure 3.11: Location of sites contributing to Laj et al., 2020. In blue, sites which provided information for a reference year and in red, sites that in addition, provided > 10-year time series for optical properties (Laj et al., 2020).

Mt. Cimone, as already mentioned in Section 2.1, is a global station in the frame of the GAW network and was one of the 90 stations which contributed to the provision of at least one core aerosol variables by Laj et al. Due to the lack of a sufficient data coverage in the selected year (2017), the total particle number concentration measured at Mt. Cimone wasn't compared with others. With the analyses carried out in this thesis, Mt. Cimone can contribute to the global variability of the physical properties. Figure 3.12 shows the yearly median of the total particle number concentration N_{tot} obtained by data provided by sites with an annual coverage of at least 75%. Data by CMN were retrospectively added to the original plot reported in the article.
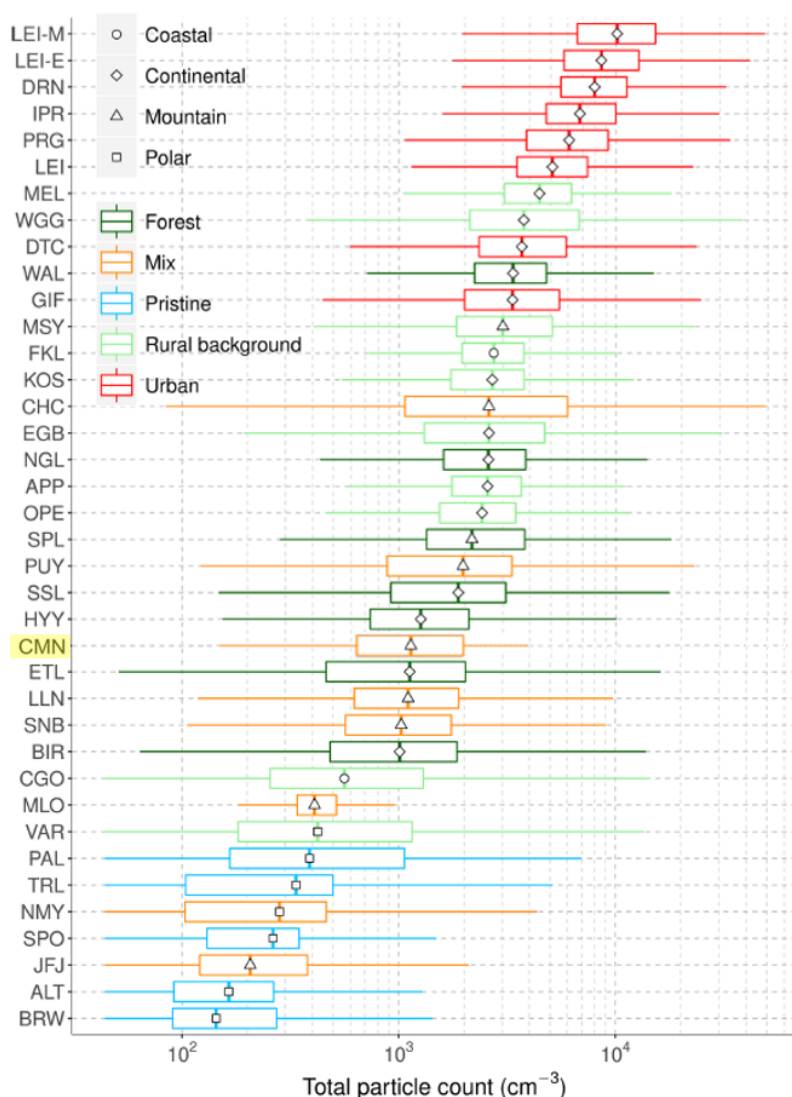
Figure 3.12: Yearly median of the total particle number concentration (N_{tot}). The markers represent the median of the data and the lower and upper edges of the box indicate the 25th and 75th percentiles, respectively. The length of the whiskers represents the 1.5 interquartile range. Different markers and box colours indicate geographical categories and footprint. (Adapted from Laj et al., 2020).

Mt. Cimone is characterized by Laj et al. as a *mountain site* for its geographical setting, and *mixed* because no dominant air mass foot-print criterion is identified. In fact, during wintertime the site receive longe transported airmasses travelling in free troposphere, while in summertime it can receive direct influence of PBL air masses from the polluted Po Valley. From figure 3.12, there is a clear distinction between the lowest particle concentration typically observed at polar sites (classified as pristine), where yearly median are of the order of $10^2 cm^{-3}$, and the highest N_{tot} exhibited by stations located at urban sites, with yearly medians in the range of $10^3 - 10^4 cm^{-3}$. Remaining sites, including CMN, contain mountain and non-urban continental and

costal stations which dispaly, on average, intermediate N_{tot}, with yearly medians of the order of $10^2 - 10^3 cm^{-3}$. Going deeper into detail, CMN is set between East Trout Lake (ETL) and Hyyttiälä (HYY). The East Trout Lake observatory is located in Canada, 150 km North of Prince Albert close to the southern edge of a boreal forest region in central Saskatchewan at an elevation of 492m above sea level, while Hyyttiälä is located in Finland and it is a rural area, mainly forest, 181m above sea level. Considering only mixed mountain sites, a median number concentration very close to the value measured at CMN is recorded at Lulin (LLN) and Sonnblick (SNB). Lulin sits in Yushan National Park, mid-Taiwan on the top of Lulin Front Mountain, 2862 m above sea level. Sonnblick Observatory is located in the Austrian Central Alps at an elevation of 3106 m a.s.l. at top of the mountain Hoher Sonnblick.

The seasonal variation of number concentration is shown in Figure 3.13.
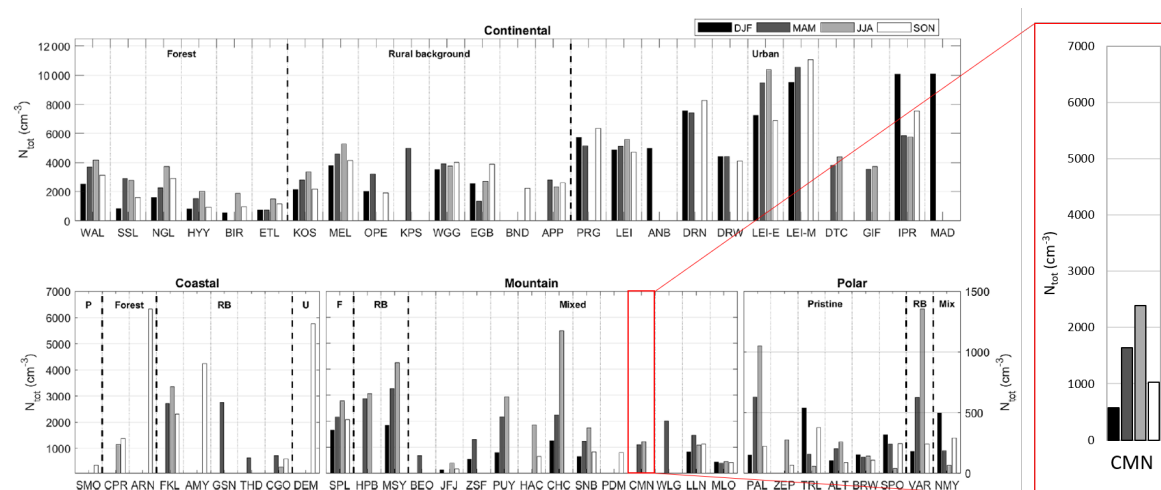
Figure 3.13: Seasonal medians of the total particle number concentration (Ntot). Stations are grouped according to their geographical category and are further sorted based on their dominant footprint. The same scale is used for coastal and mountain sites. (Adapted from Laj et al., 2020).

The polar stations display a very clear seasonal cycle compared to other geographical categories. In contrast, station located in urban areas exhibit a weak seasonality, likely related to the contribution of very local sources (e.g. traffic, domestic heating, ...). All the remaining sites do not exhibit a common behaviour as the sites located at high latitudes or in urban areas. However, mountain sites like Mt.Cimone, exhibit more pronounced seasonality relative to lowland stations. The seasonality of Monte Cimone number concentration updated with the retrieved data is shown in the red box of Figure 3.13, and replaces the previous values only concerning winter and spring, that where related to year 2017. The actual values are more robust, as representative of 7.5 years averaged seasonality.

3.3 New Particle Formation at Mt. Cimone

3.3.1 Classification

Before analysing the statistics of the events of new particle formation,it is useful to show some examples of days that have been classified by visual inspection according to the instructions set by Dal Maso et al., 2005 and Hirsikko et al., 2007, reported in paragraph 2.4.2. Some typical particle size distribution patterns over time as well as their number particle concentrations trend, highlighting the shape of each class of events, undefined days, and non-event are shown below.

Class Ia

Figure 3.14 shows a typical example of class Ia event and was registered at Mt. Cimone on 30 May 2007. Scientists call these type of new particle formation *banana-event* because of the characteristic banana shape in the plots of size distributions as a function of time. The formation of new particles, which begins at 10:00, and their subsequent growth to larger particle sizes can be clearly observed for several hours.
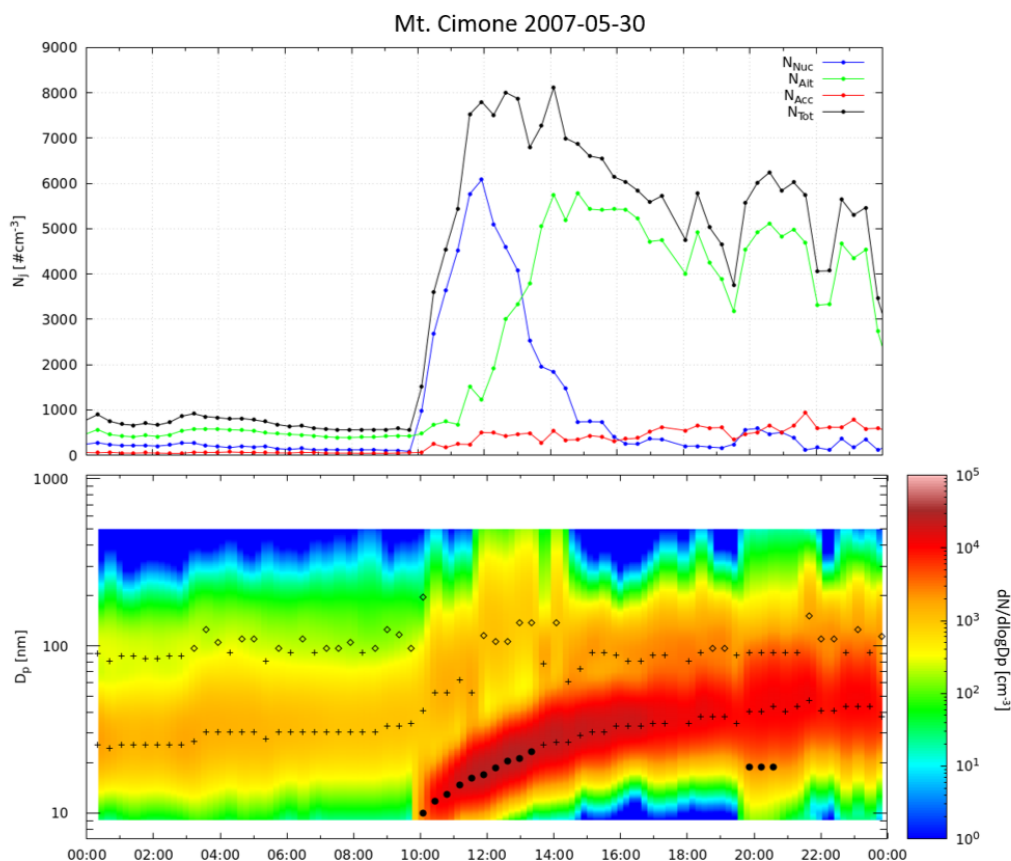
Figure 3.14: Class Ia event observed at CMN on 30 May 2007.

Class Ib

In Figure 3.15 an example of class Ib event is reported. This event was registered at Mt. Cimone on 23 June 2010. In this kind of event, the formation of the nucleation mode happens around 13:00, and, even if the new particle formation is clear, this event is not as strong (lower concentration) as class-Ia. In this example, indeed, the number concentration of Nucleation particles growth to a maximum value of around 1000 particle per cubic centimeters, while in the previous example of class Ia event (Figure 3.14) N_{nuc} reaches a value of around 6000 particles per cubic centimeter. Moreover, after the appearance of nucleation mode, the growth is not continuous, but several interruptions are evident.
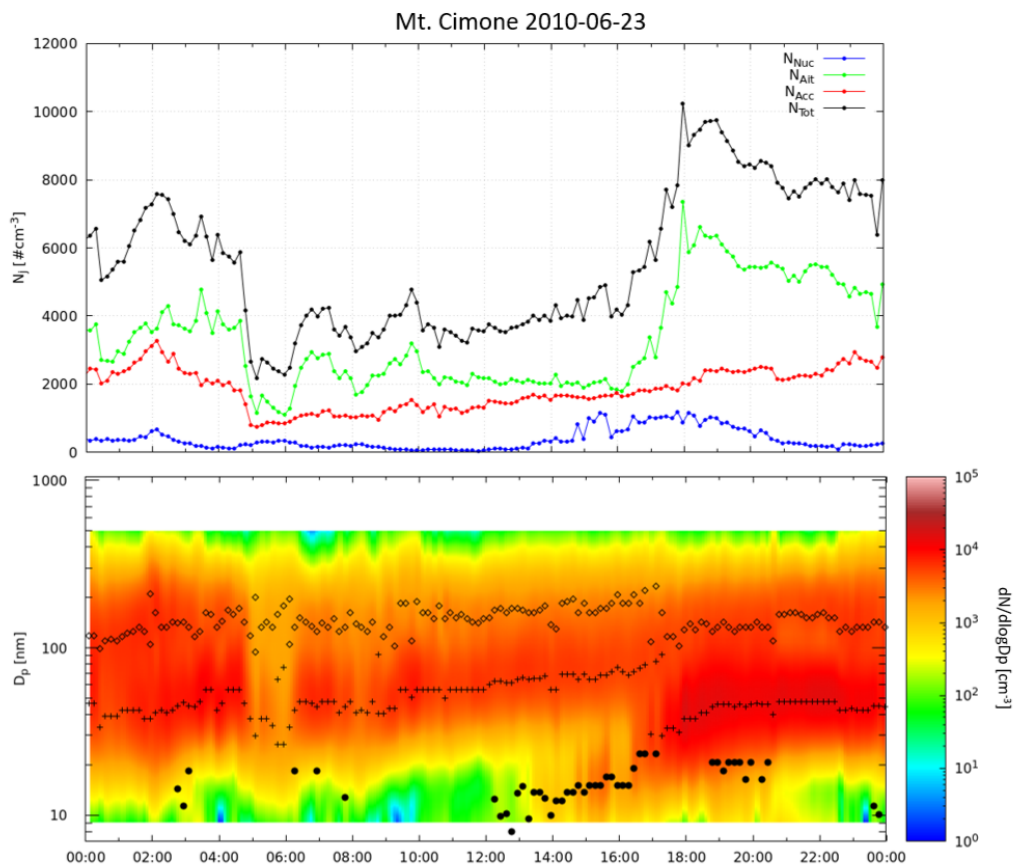
Figure 3.15: Class Ib event observed at CMN on 23 June 2010.

Class II

Figure 3.16 shows a typical example of class II event of new particle formation. As already mentioned in paragraph 2.4.2, the dynamic properties (i.e., formation and growth rates) of the nucleation mode particles can be retrieved in class I events, whereas in class II this is not possible since the growth occurs very fast and thus are very limited in time duration. Indeed, in the day taken as an example for this kind of event (26 February 2012), the growth occurs in a very short temporal range of around 1 hour, from 12:30 to 13:30. Hence, according to Dal Maso et al., 2005, the dynamic characteristics cannot be retrieved with accuracy.
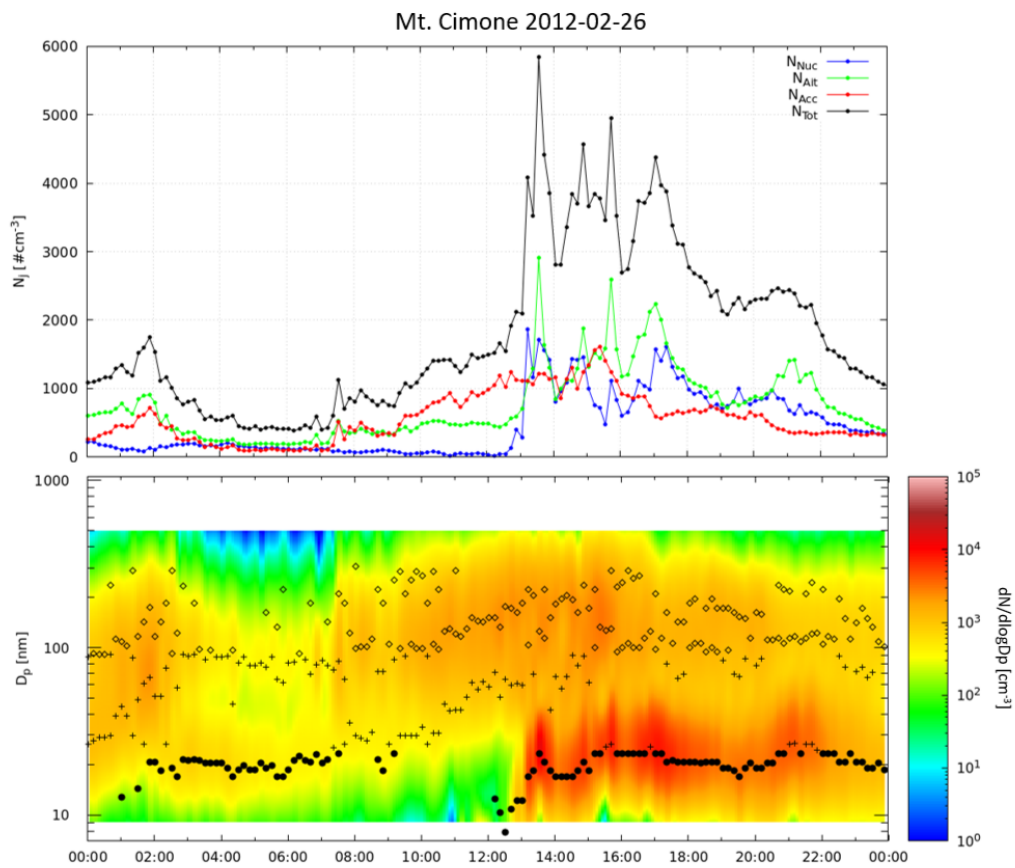
Figure 3.16: Class II event observed at CMN on 26 February 2012.

Undefined

Undefined days are those for which determining whether NPF had been taken place or not is ambiguous. An example for this kid of plot is the 16 June 2006 at Mt. Cimone, reported in Figure 3.17. For this day it is quite difficult to determine if a distinct new mode appears within the nucleation-mode size range. Even if particles were measured at the smallest sizes, size distributions presented an unclear shape.
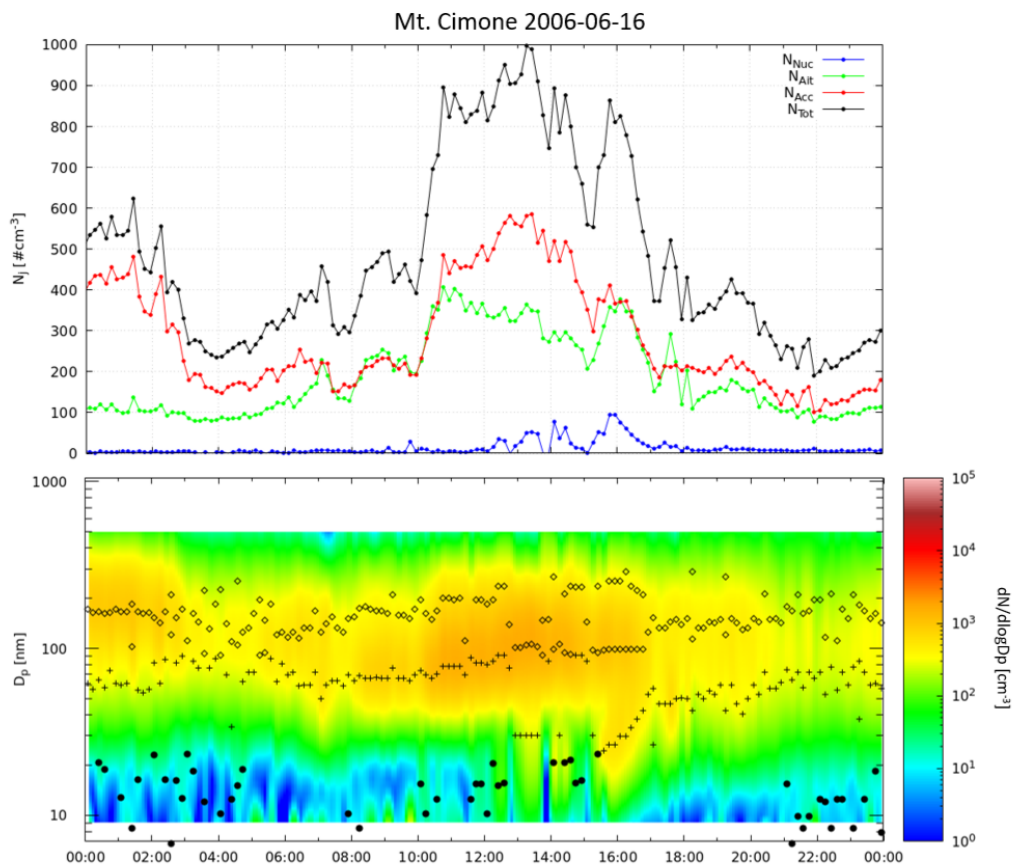
Figure 3.17: Undefined day observed at CMN on 16 June 2006.

Non-Event

A plot like the one shown in Figure 3.18, which displays the 14 January 2008, is unambiguously classified as non-event day. Non-event days are simple to classify because there is a clear evidence that no new particles are formed in the size range below $25nm$. The larger particles dominate throughout the day and their concentration doesn't exhibit significant variations over the whole day.
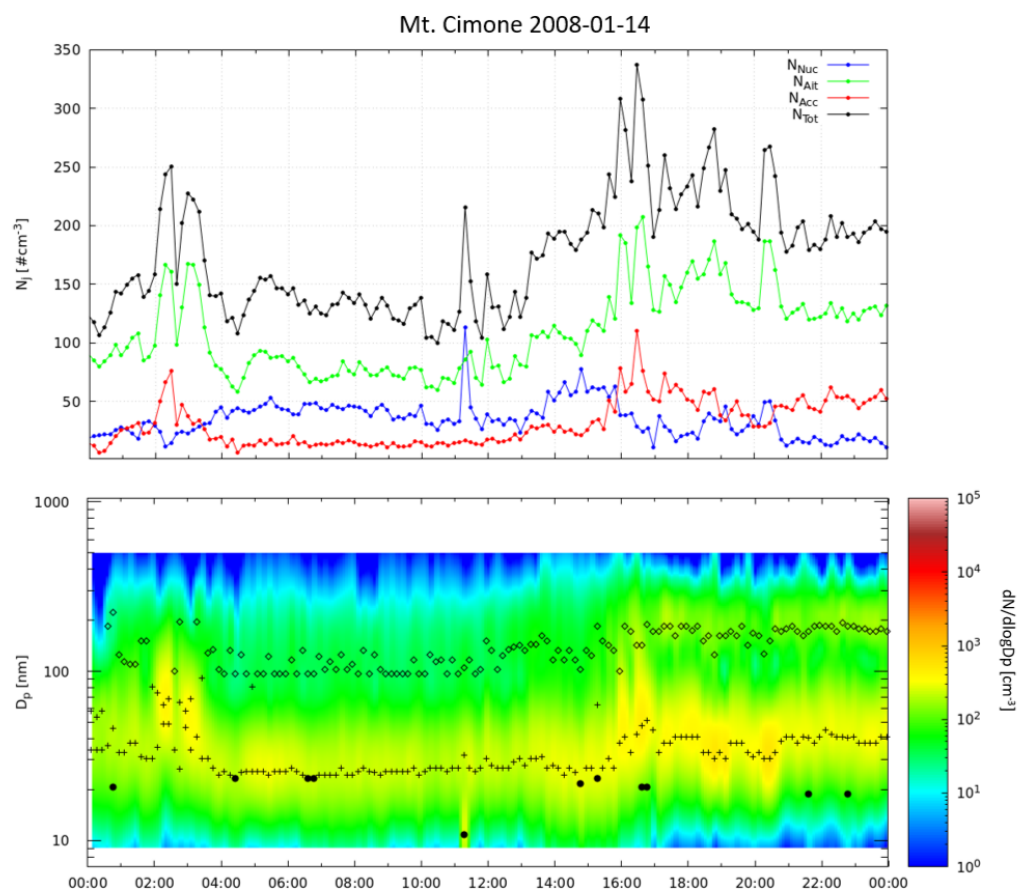
Figure 3.18: Non-event observed at CMN on 14 January 2008.

3.3.2   Event frequency

Our dataset includes 2 174 days. After the visual inspection, performed by three people as mentioned in paragraph 2.4.2, 36 days (1.7%) are classified as *bad data*, because of data not recorded for most of the day. This means that they could not be classified. Over the seven and half years of observation, a total of 570 days (26.7%) are recognized as *events* and could be further divided according to the instructions by Hirsikko et al., 2007. Class Ia represents the 32.1% of total events with 183 days, class Ib is the 19.3% with 110 days, and class II covers the largest percentage of 48.6% with 277 days. Non-events amount to 29.6% of classifiable days, and the rest of the days (43.7%) are classified as undefined. The overall statistic of the days classification is reported in Table 3.4.

	Days	Percentage of all days	Percentage of classified days
Total days	2174		
Classifiable	2138	98.3	
Not classifiable	36	1.7	
Total events	570	26.2	26.7
Class Ia	183	8.4	8.6
Class Ib	110	5.1	5.1
Class II	277	12.7	13.0
Non-event	633	29.1	29.6
Undefined	935	43.0	43.7

Table 3.4: Event statistics at CMN, from November 2005 to July 2013.

3.3.3   Interannual variability

The event occurrence from November 2005 to July 2013 is reported in Figure 3.19. The annual average of classes Ia, Ib and II events, taking into account only years with an annual coverage greater than 75% (i.e. 2007, 2009, 2010, 2011 and 2012), is around 26, 17 and 43 days respectively. Adding up the days in each of the three classes the annual average occurrence of total events recorded at Mt. Cimone is around 86 days. The non-event occurrence is around 84 days, with a minimum of 59 classified days in 2012 and a maximum of 111 in 2009. Undefined days occur on average 132 times over a typical year. Average, minimum and maximum days classified according to Hirsikko et al., 2007 and Dal Maso et al., 2005 only for the years with annual coverage greater than 75% are reported in Table 3.5.
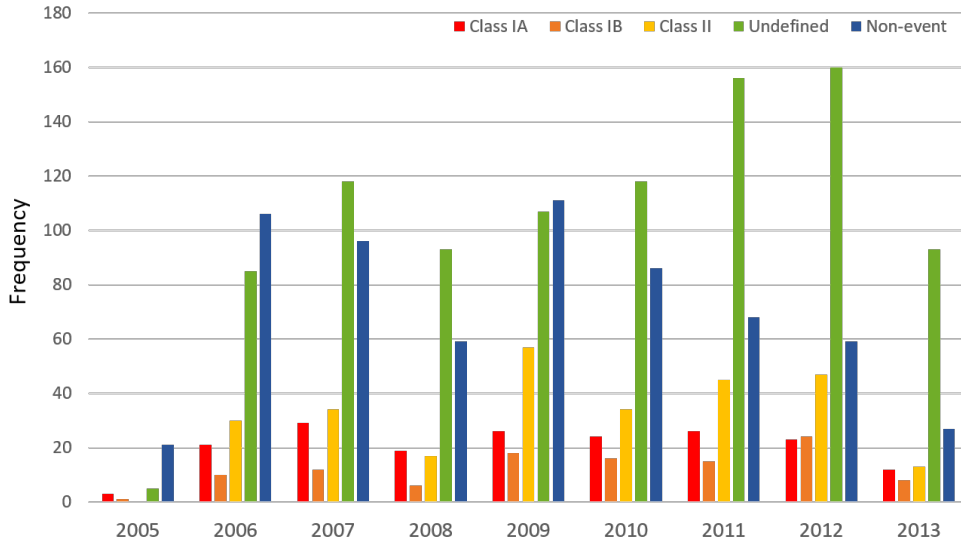
Figure 3.19: Total number of event days, non-event days and undefined days during each year at CMN (November 2005-July 2013).

	Class Ia	Class Ib	Class II	Undefined	Non-Event
Mean	26	17	43	132	84
Min	23	12	34	107	59
Max	29	24	57	160	111

Table 3.5: Average, minimum and maximum days observed at CMN classified according to Hirsikko et al., 2007 and Dal Maso et al., 2005. Only years featuring annual coverage greater than 75% are presented.

The annual percentage contributions of class Ia, Ib, II, undefined and non-events of the total annual classifiable days for years with an annual coverage greater than 75% are plotted in Figure 3.20.
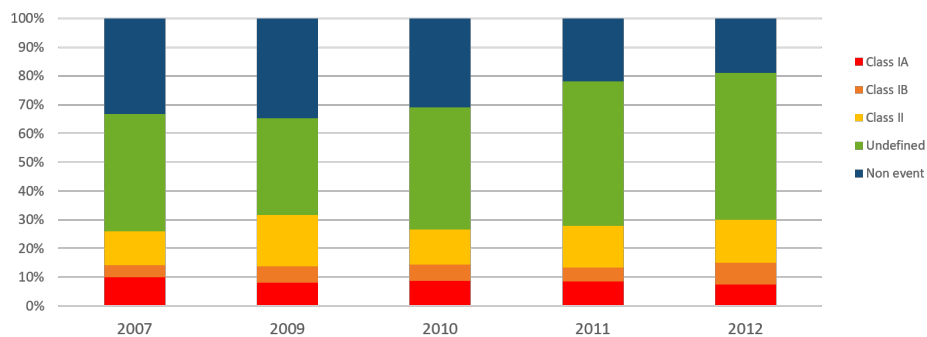
Figure 3.20: Annual percentage contributions of class Ia, Ib, II, undefined and non-events of the total annual classifiable days observed at CMN. Only years featuring annual coverage greater than 75% are presented.

It can be noticed that the quantity of total event days is quite constant every year. Even if it is not possible to define a clear trend, it is evident that non-events days, contrariwise, decrease of around 15% in 5 years, while the undefined days increase about the same quantity. In general, however, the amount of years featuring a good annual coverage is not sufficient to figure out whether any long-term interannual variability exists.

3.3.4 Seasonal variability

The typical annual variation of event occurrence at Mt. Cimone is shown in Figure 3.21. The highest count of class Ia events is registered in May, with the 19.6% of the days. In May, also the occurrence of total events is greater than any other month, reaching the 43.5% of days. A second maximum is observed in August, when the total number of events is 38.2%. The month with the lowest number of total events is January, featuring only the 11.3% of the days; class Ia events occur only for the 1.6% of the days. Moreover, January presents the highest concentration of non-event, with a percentage of 48.9%.
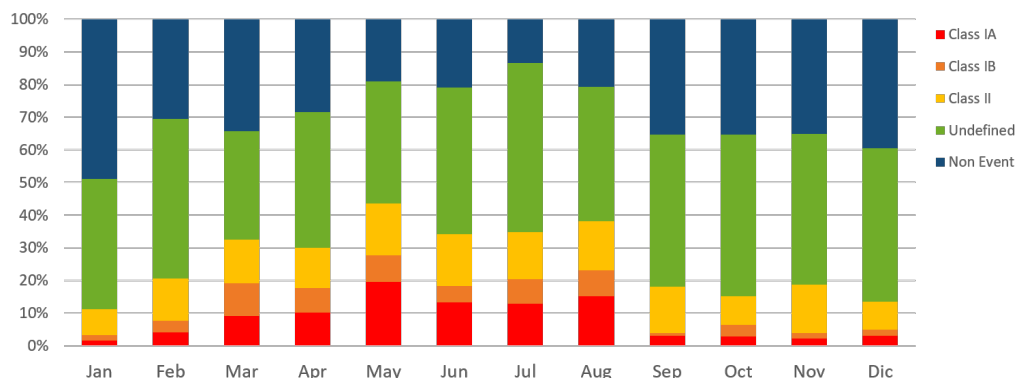
Figure 3.21: Monthly percentage contributions of class Ia, Ib, II, undefined and non-events of the total monthly classifiable days observed at CMN (November 2005-July 2013).

The seasonal average count of days per year classifiable as class Ia, Ib, II, undefined and non-events is reported in Table 3.6. Spring and summer present on average the same number of total events days, which is 33. Winter exhibits the lowest number of days featuring the occurrence of an event, only 13. Undefined days are on average around the same (~ 42) for winter, autumn and summer, while they are a bit less during spring (34). Non-event days are quite few days during summer, only 17. The greater number of non-event days is during winter with 36, followed by autumn with 32. In general, an average year at Mt. Cimone features 95 days in which events of class

Ia, Ib, or II are recorded, 160 days undefined, and 110 days without the occurrence of any event.

	Spring	Summer	Autumn	Winter	Year
Total Event	33	33	16	13	95
Class Ia	12	13	3	3	30
Class Ib	8	6	2	2	18
Class II	13	14	11	9	47
Undefined	34	42	43	41	160
Non-Event	25	17	32	36	110

Table 3.6: Average count of days per year classifiable as class Ia, Ib, II, undefined and non-events observed at CMN (November 2005-July 2013).

3.3.5   Growth rate

The growth rates of nucleation mode particles in our class Ia events are obtained as described in paragraph 2.4.3. The mean value which results by averaging all the growth rates is $4.65 \pm 1.97 nm/h$, while the median is $4.28\,[3.18 - 5.80]nm/h$. The typical annual variation is shown in Figure 3.22, where the blue points are all the single values retrieved while the orange squares show the monthly median values.
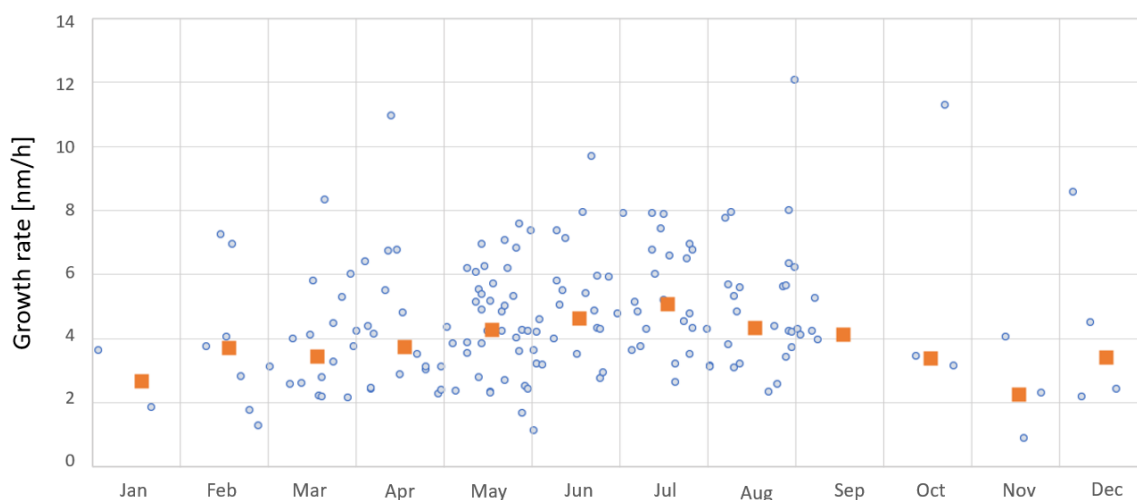
Figure 3.22: New particle diameter growth rates as a function of the day of the year at CMN (November 2005-July 2013). The orange squares represent the monthly median growth rate.

The graph exhibits an increase of nucleation mode growth rate towards summer, when the values are generally over the mean and the NPF events more intense. The maximum value is registered in July, with a mean growth rate of $5.42 \pm 1.60 nm/h$ and a median growth rate of $5.13[4.30 - 6.76]nm/h$. Despite the high variability of values, the monthly average shows a quite regular increase of the growth rate during spring, while in autumn it decreases reaching a minimum value in November, with a mean growth rate of $2.41 \pm 1.29 nm/h$ and a median growth rate of $2.31[1.59 - 3.17]nm/h$. The monthly mean and median values of the growth rate are reported in Table 3.7.

Month	Mean GR ± SD [nm/h]	Median GR [25-75th percentile] [nm/h]
Jan	2.72±0.88	2.73 [2.29-3.17]
Feb	3.98±2.17	3.75 [2.28-5.49]
Mar	3.91±1.66	3.51 [2.59-4.68]
Apr	4.39±2.16	3.82 [2.92-5.33]
May	4.61±1.57	4.33 [3.59-5.71]
Jun	4.87±1.83	4.69 [3.60-5.83]
Jul	5.42±1.60	5.13 [4.30-6.76]
Aug	5.05±2.14	4.39 [3.40-5.68]
Sep	4.39±0.51	4.17 [4.07-4.49]
Oct	5.31±3.44	3.42 [3.33-5.40]
Nov	2.41±1.29	2.31 [1.59-3.17]
Dec	4.42±2.56	3.47 [2.37-5.53]

Table 3.7: Monthly average ± 1 standard deviation and median [25th and 75th percentiles] of GR [nm/h] of a typical year at CMN (November 2005-July 2013). Statics are calculated on class Ia events.

By applying the algorithm used to derive the growth rate, it is also possible to identify the instants at which the growth of the modal geometric mean diameter of nucleation particles begins, starting from $9nm$, and ending, i.e. when it reaches $25nm$. The frequencies of the temporal distribution of the beginning and the end of Dp growth are reported in Figure 3.23.
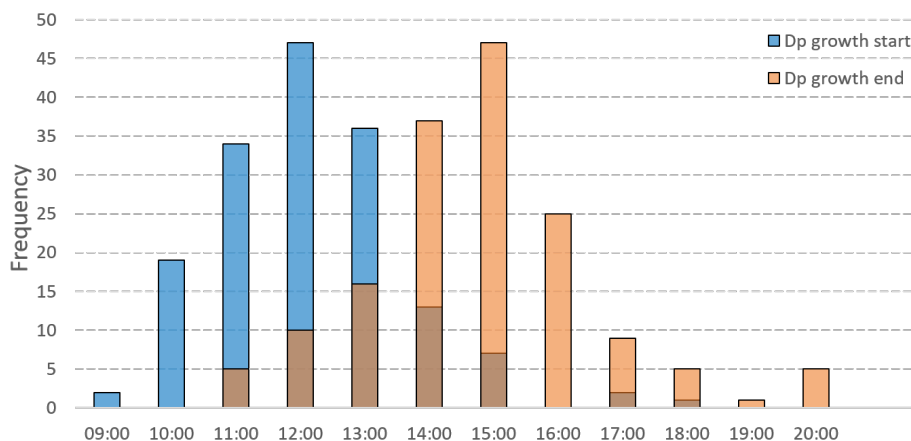
Figure 3.23: Frequency histograms showing the temporal distribution of the beginning and the end of Dp growth for all the class Ia events occurred at CMN, from November 2005 to July 2013.

By averaging all the beginning and final times recorded of *Dp* growth for the class Ia events observed at Mt.Cimone from November 2005 to July 2013, it results that the mean time at which *Dp* starts growing is 12:33, while the growth stops on average at 15:18. So, the nucleation particles growth lasts 2:45 hours, on average ranging from 12:33 to 15:18. The seasonal average lengths of *Dp* growth time are reported in Table 3.8 together with the averages of the initial and final instants of the growth.

Seasons	Mean start time	Mean end time	Mean duration [h]
Spring	12:49	15:39	2:50
Summer	12:11	14:38	2:27
Aumtun	12:31	16:08	3:37
Winter	13:07	16:20	3:13

Table 3.8: Seasonal averages of the start time, end time and duration of *Dp* growth for class Ia events occurred at CMN, from November 2005 to July 2013.

From the seasonal averages reported in Table 3.8 it's clear that new particle growth starts earlier during summer, around 12:11, and lasts less (only 2:27 hours) than other seasons. In contrast, winter growth of nucleation particles begins on average at 13:07 and finishes at 16:20. During autumn, the longest lasting Dp growth are observed, taking one hour more than in summer.

3.3.6 Time evolution of N_{nuc}

The same studies conducted for the growth rate can be done also for the time evolution of nucleation particle number concentration during class Ia events. The mean rate at which nucleation concentration increases, dN_{nuc}/dt, is $0.50 \pm 0.56 cm^{-3}s^{-1}$, while the median is $0.34[0.14 - 0.67]cm^{-3}s^{-1}$. The typical annual variation is shown in Figure 3.24, where the green points are all the values retrieved while the red squares are the monthly median values.
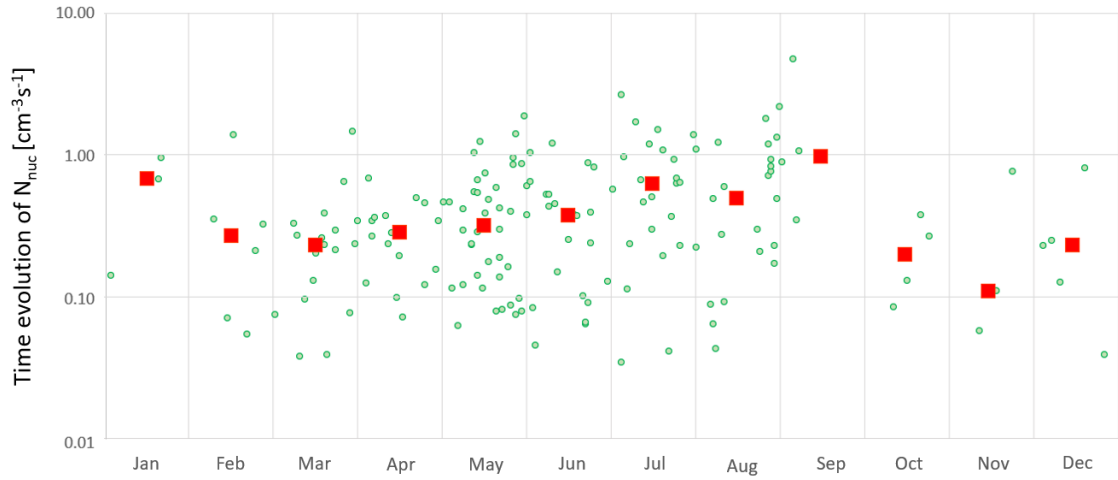
Figure 3.24: Nucleation number concentration time evolution as a function of the day of the year at CMN (November 2005-July 2013). The red squares represent the monthly median time evolution. The plot is in semi-log scale.

The graph exhibits an increase of nucleation concentration growth rate towards summer, reaching a maximum value at the beginning of autumn, in September. During this month the median value for dN_{nuc}/dt is $0.98[0.76 - 2.00]cm^{-3}s^{-1}$, while the mean is $1.77 \pm 1.76 cm^{-3}s^{-1}$. A smaller maximum can be observed in January with a median dN_{nuc}/dt of $0.68[0.41 - 0.82]cm^{-3}s^{-1}$. The monthly mean and median values of the dN_{nuc}/dt are reported in Table 3.9.

Month	Mean $dN_{nuc}/dt \pm$SD $[cm^{-3}s^{-1}]$	Median dN_{nuc}/dt [25-75th percentile] $[cm^{-3}s^{-1}]$
Jan	0.59±0.34	0.68 [0.41-0.82]
Feb	0.40±0.46	0.27 [0.11-0.35]
Mar	0.30±0.33	0.23 [0.10-0.30]
Apr	0.29±0.16	0.29 [0.16-0.37]
May	0.45±0.41	0.32 [0.13-0.56]
Jun	0.41±0.32	0.38 [0.12-0.55]
Jul	0.75±0.62	0.63 [0.27-1.02]
Aug	0.67±0.58	0.49 [0.22-1.02]
Sep	1.77±1.76	0.98 [0.76-2.00]
Oct	0.22±0.12	0.20 [0.12-0.30]
Nov	0.31±0.32	0.11 [0.08-0.44]
Dec	0.29±0.27	0.23 [0.13-0.25]

Table 3.9: Monthly average ± 1 standard deviation and median [25th and 75th percentiles] of dN_{nuc}/dt $[cm^{-3}s^{-1}]$ of a typical year at CMN (November 2005-July 2013).

The instant when nucleation number concentration starts increasing and the instant when it stops are identified applying the algorithm presented in paragraph 2.15. The frequencies of the temporal distribution of the beginning and the end of N_{nuc} growth are reported in Figure 3.25.
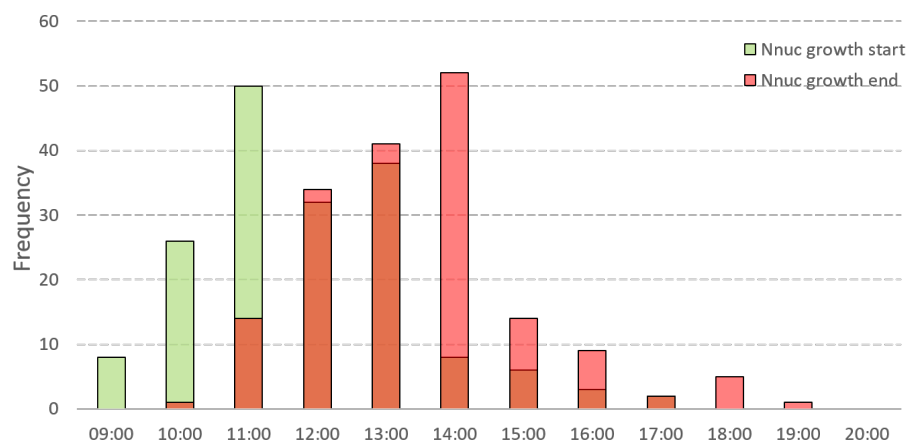
Figure 3.25: Frequency histograms showing the temporal distribution of the beginning and the end of N_{nuc} growth for all the class Ia events occurred at CMN, from November 2005 to July 2013.

By averaging all the beginning and final times of N_{nuc} growth recorded for the class Ia events observed at Mt.Cimone from November 2005 to July 2013, it results that the

mean time at which N_{nuc} starts growing is 12:12, while the growth stops on average at 13:50. So, the mean duration of the nucleation particle concentrations growth lasts 1:38 hours. The seasonal average lengths of N_{nuc} growth time are reported in Table 3.10 together with the averages of the initial and final instants of the growth.

Seasons	Mean start time	Mean end time	Mean duration [h]
Spring	12:29	14:06	1:36
Summer	11:44	13:25	1:41
Autumn	12:10	13:53	1:43
Winter	13:10	14:36	1:25

Table 3.10: Seasonal averages of the start time, end time and duration of N_{nuc} growth for class Ia events occurred at CMN, from November 2005 to July 2013.

From Table 3.10, it's clear that nucleation number concentration starts increasing earlier during summer, around 11:44, while in winter the growth begins at 13:10. During autumn and spring it begins on average at 12:10 and 12:29, respectively. The seasonal average time lengths are all close to the mean annual value of 1:38 hours, lasting a bit longer ($\sim$ 3 and 6 minutes) during summer and autumn and a bit less ($\sim$ 2 and 13 minutes) during spring and winter.

3.3.7 Daily variation of condensation sink

As already mentioned in paragraph 2.4.4, the aerosol condensation sink (CS) determines how rapidly vapour molecules condense onto pre-existing aerosols and it depends strongly on the shape of the size distribution (Equation 2.21). In theory, high CS is thus expected to have an inhibiting effect on NPF, that are conversely favoured by a low CS. Figures 3.26 and 3.27 provide the daily variation of the mean and median condensation sink values retrieved maintaining the original time-resolution of 10 minutes during typical non-event and class Ia event days, respectively. During the typical non-event day, CS is characterized by a flat curve (Figure 3.26), where the mean condensation sink has an average value of $0.280 \cdot 10^{-3} s^{-1}$ and ranges between 0.237 and $0.341 \cdot 10^{-3} s^{-1}$. All the values from 10:30 in the morning to 20:00 in the evening are slightly larger than the average, while they are smaller during night.
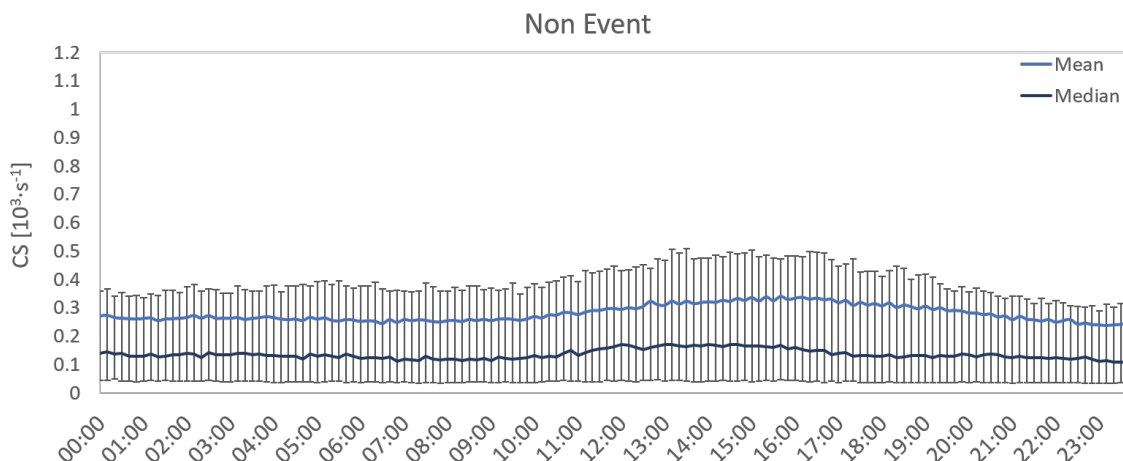
Figure 3.26: Typical daily variation of the mean and median CS $[s^{-1}]$ values during a typical non-event day retrieved from NPSD measured at CMN (November 2005-July 2013). 25-75th percentile ranges indicated by vertical bars.

The typical event day shows a more variable curve, as can be seen in Figure 3.27. On average, the mean condensation sink has a value of $0.483 \cdot 10^{-3} s^{-1}$, higher than non-event median value. From midnight to 4:00 in the morning, it presents a quite constant value around $0.400 \cdot 10^{-3} s^{-1}$, then it starts decreasing, reaching a minimum of $0.330 \cdot 10^{-3} s^{-1}$ at 9:00 in the morning. From 9:00 in the morning, the condensation sink increases reaching the maximum value of $0.702 \cdot 10^{-3} s^{-1}$ at 17:20 in the afternoon.
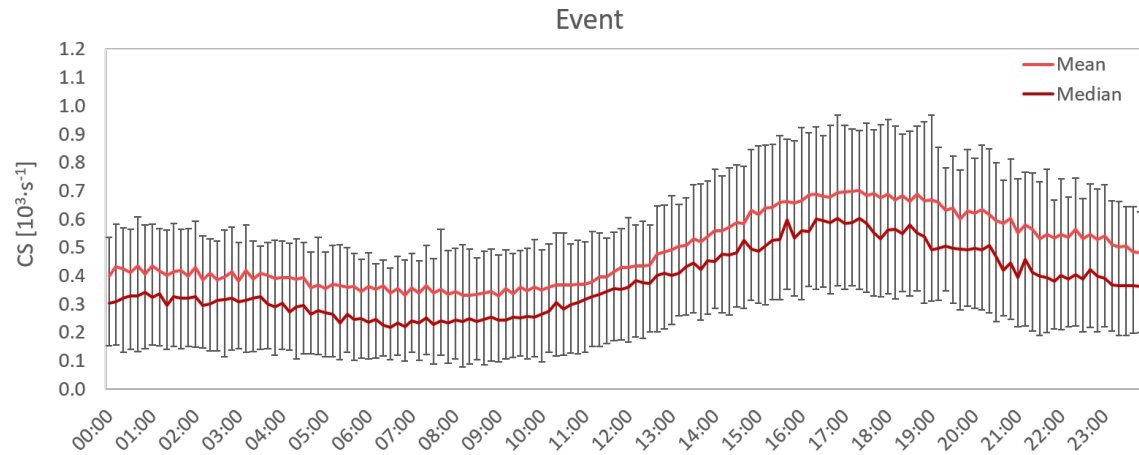
Figure 3.27: Typical daily variation of the mean and median CS $[s^{-1}]$ values during a typical class Ia event day retrieved from NPSD measured at CMN (November 2005-July 2013). 25-75th percentile ranges indicated by vertical bars.

The behavior of the averaged curve of Ia events, which exhibits a decrease of CS during morning hours, is consistent with the fact that low condensation sink has been found to trigger new particle formation (Kulmala et al., 2005). The maximum value reached in the afternoon is easily explainable by the increase of surface area available as a result of new particle formation, which offer new surface to vapours to condense on rather than forming new ones.

3.3.8   Seasonal variation of condensation sink

The seasonal variability of CS during class Ia events and non-events day at Mt. Cimone is reported in Figure 3.28. The boxplot shows that both event and non-event days present the same seasonal trend, with higher values during summertime and lower condensation sink in winter. This behaviour reflects the influence of anthropogenic sources in a mountain sites, that is very clean in winter (low particle concentration) and affected by pollution transport from PBL in warmer seasons.
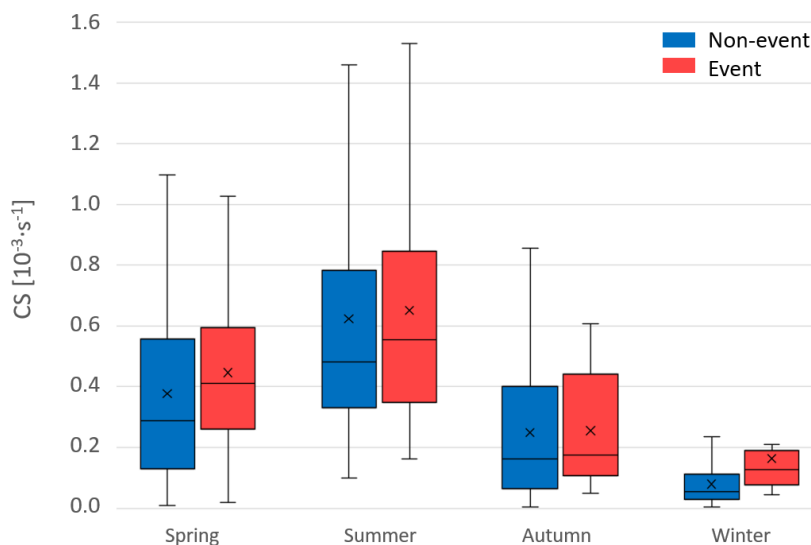
Figure 3.28: Box plot representing the mean, median, and 25- 75th percentile of CS $[10^3 s^{-1}]$ values for typical seasonal class Ia event and non-event days retrieved from NPSD measured at CMN (November 2005-July 2013).

As can be seen from Table 3.11, mean and median CS values are always greater for event days, with respect to non-event, due to the the increase of surface area generated by new particle formations.

	Non event	
Season	**Mean CS $\pm$ SD** $[10^{-3}s^{-1}]$	**Median CS [25-75th percentile]** $[10^{-3}s^{-1}]$
Spring	0.377±0.318	0.289 [0.130-0.549]
Summer	0.623±0.459	0.481 [0.347-0.761]
Autumn	0.249±0.248	0.162 [0.065-0.389]
Winter	0.079±0.083	0.054 [0.028-0.111]

	Event	
Season	**Mean CS $\pm$ SD** $[10^{-3}s^{-1}]$	**Median CS [25-75th percentile]** $[10^{-3}s^{-1}]$
Spring	0.446±0.241	0.411 [0.267-0.582]
Summer	0.650±0.383	0.554 [0.349-0.833]
Autumn	0.255±0.177	0.174 [0.124-0.407]
Winter	0.163±0.124	0.126 [0.080-0.170]

Table 3.11: Seasonal average $\pm$ 1 standard deviation and median [25th and 75th percentiles] of condensation sink values for both typical non-event and class Ia event days, retrieved from NPSD measured at CMN (November 2005-July 2013).

The diurnal variation in condensation sink during non-event and class Ia event days is reported for every season to better understand its variability. Starting from a typical spring day, Figure 3.29 displays the daily evolution of CS for both non-event and class Ia event. The curves are almost overlapping over the first half of the day around values between $0.300 \cdot 10^{-3}s^{-1}$ and $0.400 \cdot 10^{-3}s^{-1}$. Then, around half past noon, the condensation sink for class Ia event increases more than that for non-event does, reaching the maximum around 17:30. The non-event increase probably reflect only the rise of aerosol concentration due to PBL oscillation and valley breezes transport, while the fraction of afternoon increase is due to the NPF contribution.
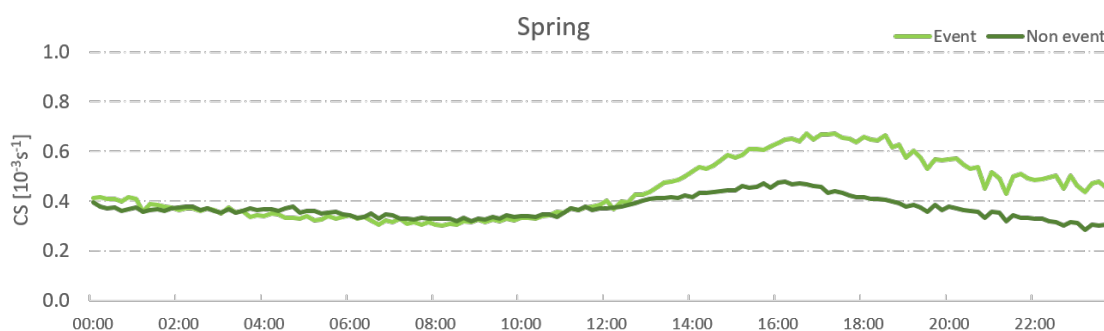
Figure 3.29: Daily variation of CS retrieved from NPSD measured at CMN over a typicial non-event and event spring day (November 2005-July 2013).

Some differences are observed (Figure 3.30) during summertime, when each curve shows a different daily behaviour. Only at the very beginning of the day (from midnight to around 3:00 in the morning) they share similar values of CS. Then, during the typical event day, CS assumes lower values than that retrieved for a typical

non-event day, remaining quite constant around $0.450 \cdot 10^{-3} s^{-1}$ from 4:00 to 11:00, when it begins to grow up quickly. Around 14:00 the situation is inverted: the event curve grows reaching values of around $0.900 \cdot 10^{-3} s^{-1}$ while CS values retrieved for non-event day remain quite constant around $0.750 \cdot 10^{-3} s^{-1}$.

This could be explained by the fact that, during summertime, Mt. Cimone is more often receptor of the transport of precursor vapors by lower altitudes with respect springtime. When the availability of condensable species in high mountain environment increases, a low CS is a favorable condition for nucleation (Sellegri et al., 2019), while a high CS can inhibit new particle formation occurrence.
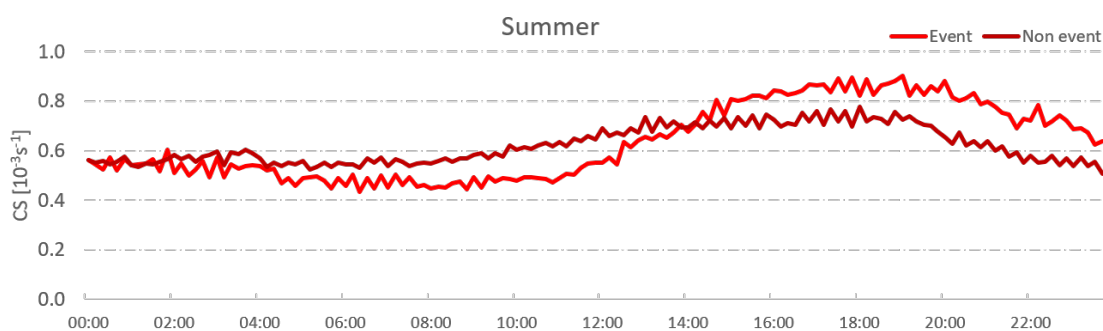
Figure 3.30: Daily variation of CS retrieved from NPSD measured at CMN over a typicial non-event and event summer day (November 2005-July 2013).

The typical autumn day reflects quite well the daily trend of CS already observed during summertime, except for the fact that CS curves are shifted to lower values, as can be seen in Figure 3.31. Condensation sink retrived for the typical event day clearly diminishes, reaching a minimum value of around $0.100 \cdot 10^{-3} s^{-1}$ which is maintained from 4:00 to 10:30 in the morning. Then, the curve starts growing until 16:10 reaching the maximum of $0.572 \cdot 10^{-3} s^{-1}$. The values of CS retrieved during the typical non-event autumn day remain quite constant ranging between $0.195 \cdot 10^{-3} s^{-1}$ an $0.308 \cdot 10^{-3} s^{-1}$ over the whole day.
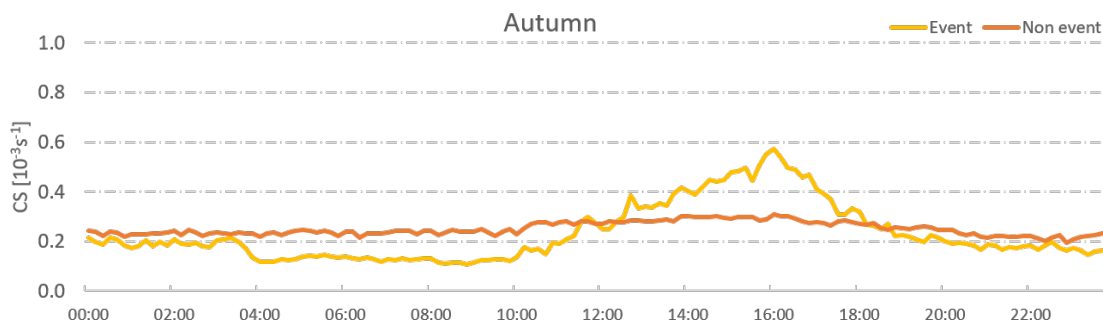
Figure 3.31: Daily variation of CS retrieved from NPSD measured at
CMN over a typicial non-event and 1a event autumn day (November
2005-July 2013).

As shown in Figure 3.32, winter days present on average very low values of CS for both event and non-event cases. Especially over wintertime Mt. Cimone is representative of the background conditions of the free troposphere, so it is completely decoupled from the polluted PBL and air masses from the ground surface. This means that very low concentrations of precoursors are available to trigger the nucleation.
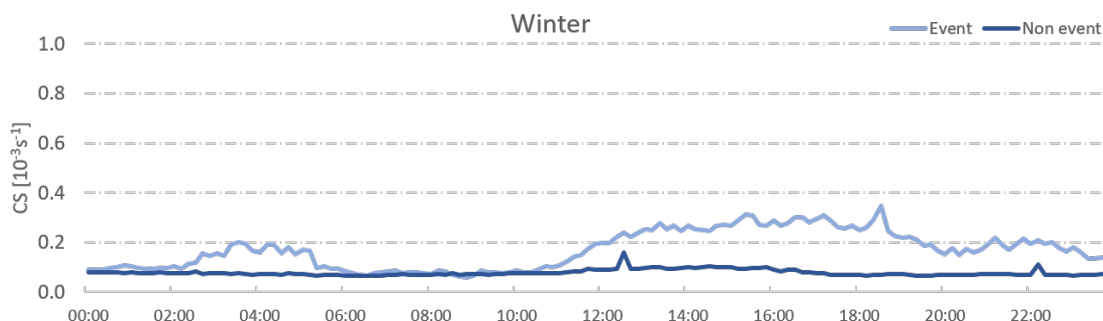
Figure 3.32: Daily variation of CS retrieved from NPSD measured at
CMN over a typicial non-event and event winter day (November
2005-July 2013).

From the observation of the daily trends, we decided to highlight the differences between the condensation sink computed over a non-event day, and the value it assumes within a time interval before the nucleation onset over an event day. We considered the condensation sink computed between 5:00 and 10:00. This time interval was selected by looking at the CS diurnal variation over the typical summer and autumn days. In this way, if in the previous boxplot reported in Figure 3.28 the CS computed for an event day are larger due to the greater number of particles following new particle

formation, now higher CS values are those retrieved over the non-event day (Figure 3.33). The only exception is during wintertime, when the mean CS for an event day is $0.087 \cdot 10^{-3}s^{-1}$, while that for the non event winter day is $0.079 \cdot 10^{-3}s^{-1}$. Table 3.12 reports mean and median CS values for the time interval from 5:00 to 10:00 of typical seasonal Ia events.
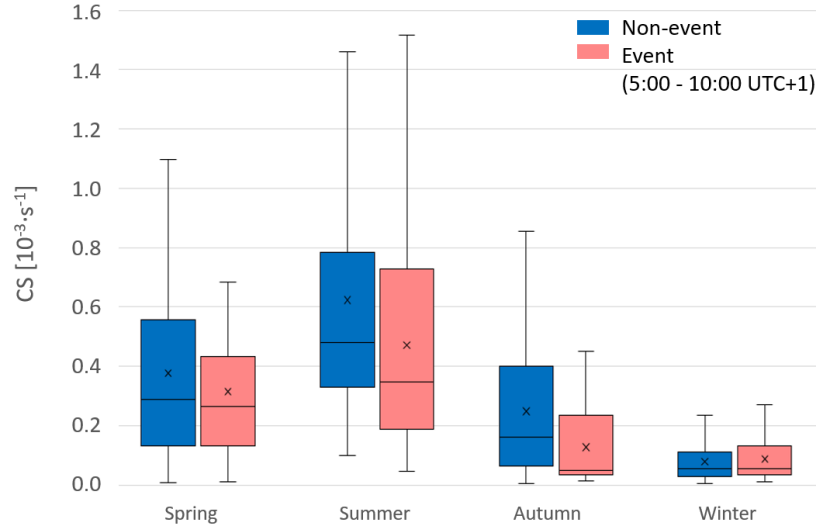
Figure 3.33: Box plot representing the mean, median, and 25- 75th percentile of CS $[10^{-3}s^{-1}]$ values for typical seasonal non-event days and values for the time interval from 5:00 to 10:00 of typical seasonal class Ia event days retrieved from NPSD measured at CMN (November 2005-July 2013).

	Event (5:00-10:00)	
Season	**Mean CS $\pm$ SD** $[10^{-3}s^{-1}]$	**Median CS [25-75th percentile]** $[10^{-3}s^{-1}]$
Spring	0.315±0.228	0.265 [0.141-0.429]
Summer	0.474±0.367	0.340 [0.189-0.727]
Autumn	0.127±0.129	0.050 [0.035-0.213]
Winter	0.087±0.077	0.056 [0.035-0.115]

Table 3.12: Seasonal average±1 standard deviation and median (25thand 75th) percentiles of condensation sink values for the time interval from 5:00 to 10:00 of a typical class Ia event days, retrieved from NPSD measured at CMN (November 2005-July 2013).

3.3.9 New Particle Formation at Mt. Cimone compared to other high altitude ground-based sites

Sellegri et al. published in 2019 a paper entitled *New Particle Formation: A Review of Ground-Based Observations at Mountain Research Stations*, in which long term data from six high altitude ground-based stations at various altitudes (from 1465m to 5420m a.s.l.) were used to derive statistically NPF features (i.e. frequency, growth rates and condensation sink) and seasonal variability. The combined information was also compared to other literature data. For practical reasons, Mt. Cimone contributed to this paper with a year of data (from January to December 2009), and some parameters were missing, such as the growth rate and condensation sink. I will present now more precise data averaged over the period November 2005 to July 2013 obtained through the analyses carried out in the present thesis. All the stations which data were compared in this paper are displayed in Figure 3.34.
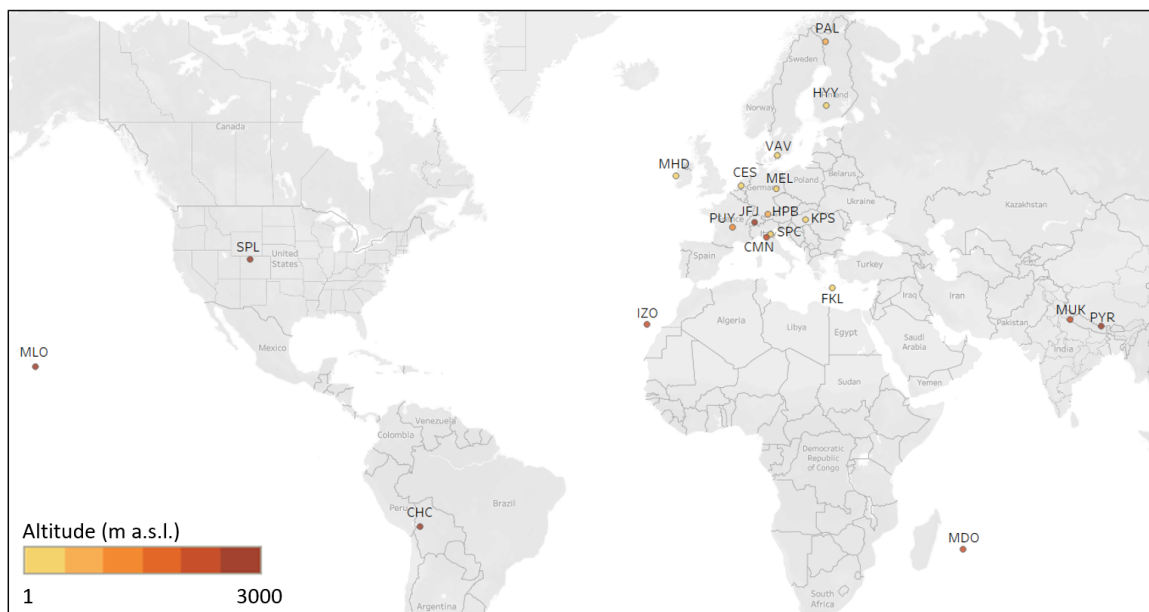
Figure 3.34: Location of sites as described in Sellegri et al., 2019.

NPF Frequency

Figure 3.35 shows average frequencies occurrence of NPF events both from the six stations studied by Sellegri et al. and from other sites below $1000m$ a.s.l., which data were taken from literature. This figure was adapted from the one reported in the paper by updating Mt. Cimone average NPF frequency retrieved over the whole observational period from November 2005 to July 2013.
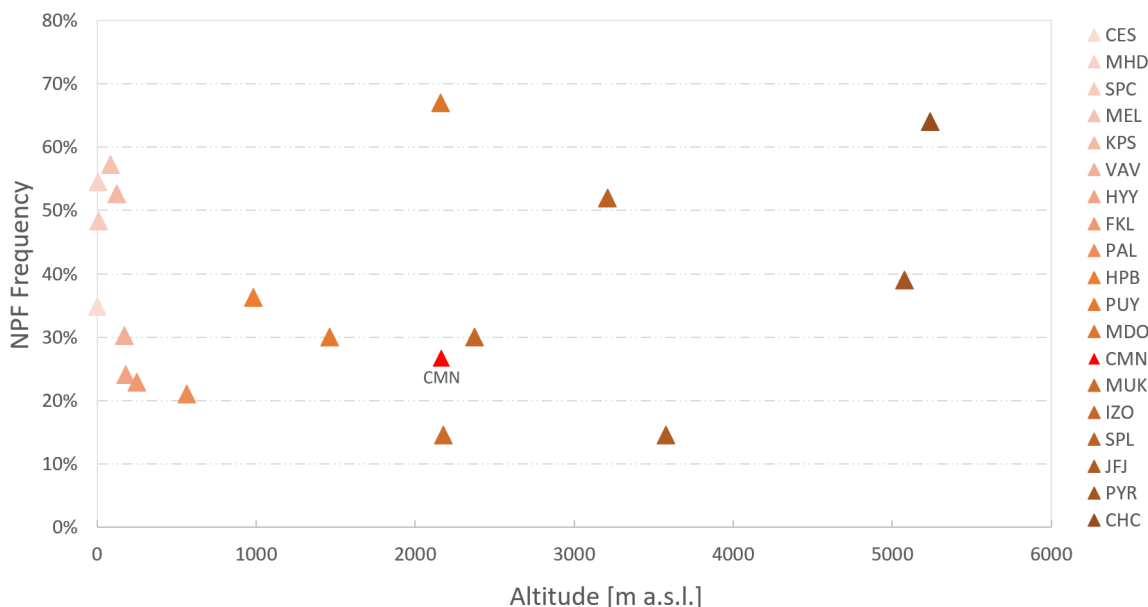
Figure 3.35: Frequency of occurrence of NPF events for the high altitude stations PUY, CMN, JFJ, PYR, MDO, and CHC and for high altitude stations, as reported in the literature. Adapted from Sellegri et al., 2019.

Annual averages of NPF frequencies at high altitudes are extremely variable, as the environments where data have been collected are very different, spanning from tropical to nearly polar sites. It is not evident a clear dependency between nucleation frequency and altitudes, even if mountain stations shows roughly higher frequencies than those located at low altitudes (below $1000m$ a.s.l.) (Sellegri et al., 2019). Mt. Cimone exhibits a NPF frequency of 26.7% very close to the one of 30.0% observed at the Izaňa station (2373 m a.s.l.), located on the Island of Tenerife, Spain, and higher than that of 14.5% observed at Mukteshwar (2180 m a.s.l) in India. Maïdo observatory, with an altitude of 2160 m a.s.l, comparable to Mt. Cimone, instead, showed the highest yearly average NPF event frequency with 67% of occurrence. This is largely due to the fact that La Reunion Island is under the influence of the marine boundary layer during daytime and of the free troposphere during night-time (Tulet et al., 2017). Moreover, the island is characterized by different environments (dense vegetation areas, littoral urbanized areas and a volcanic area) that are present at local scale which can correspond to different types of sources of gas-phase precursor, namely providing sulfur dioxide (SO_2), sulfuric acid (H_2SO_4), ammonia (NH_3), volatile organic components (VOCs), phytoplancton and so on. Solar radiation is also much greater than Mt. Cimone at tropical latitude.

Figure 3.36 shows the averaged frequency occurrences of NPF events only high altitude sites (higher than 1000 m a.s.l.). This figure was adapted from the one reported in the paper by updating Mt. Cimone monthly values of NPF frequency retrieved over the whole observational period from November 2005 to July 2013.
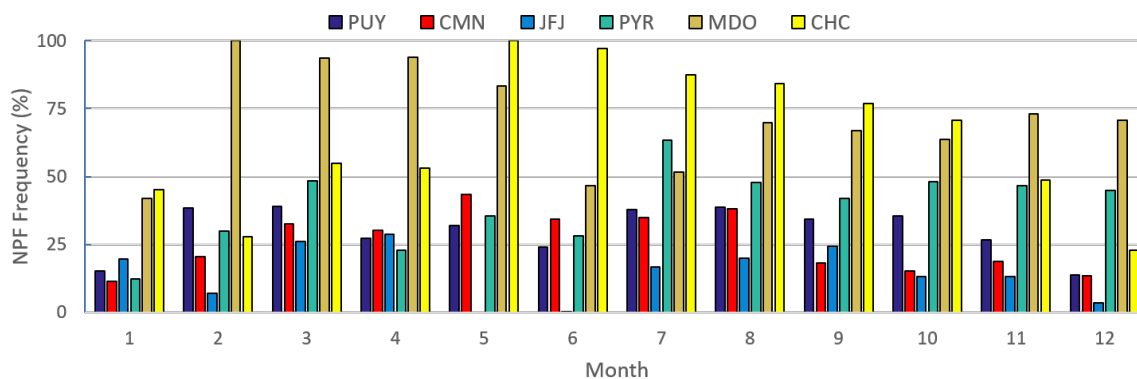
Figure 3.36: Average frequencies occurrence of NPF events only high altitude sites (higher than $1000m$ a.s.l.). Adapted from Sellegri et al., 2019.

Condensational Sink

Sellegri et al., 2019, found that at high altitude sites, the occurrence of the NPF process might be determined rather by the availability of condensable vapors, which are likely to be transported together with pre-existing particles from lower altitudes. In fact, at lower altitude sites condensable vapors are always present at relatively high concentrations due to the proximity of the sources, while at high altitude, especially in wintertime, when the stations are in free troposphere, the presence of condensable vapors is probably the limiting factor to trigger the nucleation at the higher altitude stations. However, the observations show that the impact of CS on the occurrence of NPF at high altitude appeared to be different from site to site. Table 3.13 reports median, 25th and 75th percentile values of condensation sink in the period before the NPF occurrence (07:00–09:00) and segregated into NPF event and non event days for PUY, JFJ, MDO, CMN and CHC stations. This table was adapted from the one reported in the paper by updating Mt. Cimone condensation sink values computed from NPSD over the period from November 2005 to July 2013.

Station	Location, altitude (m a.s.l.)	Median CS [25-75th percentile] $(10^3 s^{-1})$	
		Non event	*Event*
PUY	France, 1465	2.86 [0.80-7.37]	2.77 [0.86-7.42]
MDO	Indian Ocean, 2160	0.49 [0.22-1.27]	0.55 [0.34-0.88]
CMN	Italy, 2165	0.12 [0.04-0.37]	0.24 [0.12-0.49]
JFJ	Switzerland, 3580	0.09 [0.04-0.20]	0.15 [0.07-0.31]
CHC	Bolivian Andes, 5240	2.06 [0.84-3.44]	3.13 [2.03-4.13]

Table 3.13: Median, 25th and 75th percentile values of condensation sink over the period 07:00–09:00 and segregated into NPF event and non event days for PUY, JFJ, MDO, CMN and CHC stations. Adapted from Sellegri et al., 2019.

The study carried out by Boulon et al., 2011, at the puy de Dôme research station (PUY) located in France 1465m a.s.l. showed that the averaged CS over few hours before the mean nucleation onset time (06:00 - 09:00) was lower for NPF event days than for non-event days, demostrating the inhibiting effect of high CS on nucleation. The opposite behaviour was, instead, observed at Jungfraujoch (JFJ), Chacaltaya (CHC), and Maïdo (MDO) stations. At JFJ, the investigation conducted by Boulon et al., 2010, revealed that high CS was not reducing the occurrence of NPF, because they were found to be positively correlated. The same behaviour was found both by Rose et al., 2015, at CHC and by Foucart et al., 2018, at MDO. At Mt. Cimone, the average CS computed over the time interval from 07:00 to 09:00 both for event and non-event days is higher for NPF event days, compared to the non-event ones. This seems at first to be consistent with what was observed at JFJ, CHC and MDO. Nevertheless, from the seasonal study reported in paragraph 3.3.8, CS is always lower for NPF event days than for non-event ones, except during wintertime, when CMN is representative of the lower free atmosphere and very little condensable vapours are available for NPF. In conclusion, during months in which Mt. Cimone receives more often air masses transported by lower altitude and rich of precursor vapours, CS is lower few hours before the mean NPF onset time as it was observed at PUY.

Growth rate

Table 3.14 reports mean GR calculated between different size ranges for high altitude stations and average values for GR_{3-7} and GR_{7-20} at sites below 1000m a.s.l. found in literature by Sellegri et al., the average GR_{3-7} and GR_{7-20} calculated at PUY by Sellegri et al., and the mean GR_{9-25} computed at Mt. Cimone in the present thesis over the long-term observation period from November 2005-July 2013.

Station	Location, altitude (m a.s.l.)	Mean GR $\{\pm\}$ SD (nm/h)
Average low altitude	Sites<1000 m	$GR_{3-7} = 4.2 \pm 1.1$
		$GR_{7-20} = 6.5 \pm 4.1$
PUY	France, 1465	$GR_{3-7} = 6.5 \pm 4.6$
		$GR_{7-20} = 8.9 \pm 5.5$
MDO	Indian Ocean, 2160	$GR_{12-19} = 20.0 \pm 12.7$
CMN	Italy, 2165	$GR_{9-25} = 4.7 \pm 1.9$
MUK	Himalaya, 2180	$GR_{15-25} = 2.4$
IZO	Atlantic Ocean, 2373	$GR_{10-25} = 0.4 \pm 0.2$
SPL	USA, 3210	$GR_{3-15} = 0.7 \pm 0.1$
MLO	Pacific Ocean, 3400	$GR_{3-15} = 0.4$
JFJ	Switzerland, 3580	$GR_{3-7} = 5.3 \pm 3.5$
		$GR_{7-20} = 5.7 \pm 2.2$
CHC	Bolivian Andes, 5240	$GR_{3-7} = 10.3 \pm 14.7$
		$GR_{7-20} = 13.7 \pm 15.9$

Table 3.14: Mean growth rates $\pm$ 1 standard deviation at different high altitude ground-based stations and average growth rates for sites located below 1000m a.s.l.. Adapted from Sellegri et al., 2019.

Sellegri et al. stated that the growth rates calculated for the European high altitudes site puy de Dôme (PUY) and Jungfraujoch (JFJ) were not significantly different from the average GR reported in the literature for sites located below 1000m a.s.l.. By comparing also the GR computed at CMN, the same also applies to the Italian station. From Table 3.14 it is evident that GR are higher for high sites located in the Southern hemisphere (MDO and CHC) than those measured in sites located in the Northern hemisphere. The ocean sites of MLO, IZO and SPL (mountain site) have very similar low growth rates, much lower than others, possibly connected with low abundance of condensing vapour.

Conclusions

In this thesis, I investigated the diurnal, seasonal, annual and interannual variability of the aerosol total number concentration and size distribution at Mt. Cimone GAW global station (2165m a.s.l.). The CMN station, located in Northern Apennines, with 360° free horizon, is a strategic site for long term observations because of its representativeness of the background conditions of the Southern Europe and Mediterranean basin, especially during wintertime. During summertime, instead, it can also and be influenced by polluted air masses carried up from lower altitude with valley breezes (Fischer et al., 2003).

With the aim of contributing to the understanding of direct and indirect effect of aerosol on climate in Mediterranean free troposphere, the aerosol size distribution measurements were carried out continuously from November 2005 to July 2013 in the framework of EUSAAR and ACTRIS projects. This is the longest aerosol size distribution in a mountain environment on the Italian territory. First of all, the raw data obtained from the DMPS, able to detect particles between $9nm$ and $500nm$, have been homogenized and filtered to form a new homogeneous dataset. The latter, which includes $2\,174$ days covering 71.6% of the time over the whole observation period, allows to characterize the aerosol size distribution over the whole acquisition period. The procedures of data preprocessing and data analysis are carried out in an automatic and reproducible way thanks to a set of scripts specifically developed. The latter could be easily adapted for future analysis on different raw data sets. In order to investigate the contribution of the different size fractions to the total particle number concentration, the aerosol number size distribution is studied into the different components: the nucleation mode (9-25nm) representative of recent new particle formation, the intermediate Aitken mode (25-100nm), and the accumulation mode (100-500nm) representing aged particles.

The long-term characterization of the aerosol population at CMN exhibits a typical bimodal number size distribution with the occurrence of one predominant mode in the Aitken range and one mode in the accumulation size range. The typical surface and volume distributions, instead, are defined by a single mode in the accumulation size range. By studying the annual trend of seasonal distributions,

it is clearly evident a seasonal variability, highlighted by the analyses of month by month variation. In particular, there are great differences between fall/winter and spring/summer size distributions, with a general increment of the number concentration for each mode during the warmer seasons, especially for the Aitken mode, which increases distinctively from winter months (DJF) to summer months (JJA). Even the accumulation number concentration increases in the same way, suggesting a possible contribution of aged polluted particles from the underlying Po Valley over summertime. Nucleation mode is less affected by this seasonal behaviour, but its contribution to particle number is more homogeneous through the year.

In this study the particles in the Aitken mode are on average the main contributor to N_{tot} accounting for about 53% (36-62%), followed by particles in the accumulation and nucleation modes with 31% (14-56%) and 16% (4-42%), respectively, throughout the observation period. The total number of particles annual variation is driven by Aitken particles, followed by the accumulation particles, showing very similar behavior, increasing during warm season and decreasing in autumn reaching a minimum concentration in winter. Nucleation mode doesn't exhibit a great median variability, but the higher mean monthly values testify the presence of NPFs which take place over the whole typical year. Concerning the daily cycle, the maximum of total particles occurring in the afternoon is associated with the increase of both Aitken and accumulation fractions generally observed between 17:00 and 18:00, while nucleation get to maximum values around midday.

The identification of NPF observed at Mt. Cimone is conducted through a visual inspection method proposed by Kulmala et al., 2012. The classification is done following the criteria set by Dal Maso et al., 2005, and by Hirsikko et al., 2007, resulting in a subdivision of classifiable days into class Ia, Ib and II events, non-events and undefined days. Over the seven and half years of observation, a total of 570 days are recognized as *events*, and correspond to the 26.7% of classifiable. Class Ia represents the 32.1% of total events with 183 days, class Ib is the 19.3% with 110 days, and class II covers the largest percentage of 48.6% with 277 days. Non-events amount to 29.6% of classifiable days, while other days (43.7%) are classified as undefined. To verify if any interannual variability exists, years with annual coverage greater than 75% are examined. However, no significant trend are identified. The typical annual variation of classifiable days shows that the higher number of events is recorded over spring and summer, with on average 33 total event days for each season. In particular, months with higher frequency of NPF occurrence are May, which reaches the 43.5% of days, and August with the 38.2%. Winter, instead, exhibits the lowest number of days featuring the occurrence of an event. January is the month with the lowest number of total events (11.3%) and the highest occurrence of non-events (48.9%).

By studying only class Ia event days, information about growth rate, time evolution

of nucleation number concentration and condensation sink is obtained. The mean value which results by averaging all the growth rates is $4.65 nm/h$. GR exhibits an increase towards summer and reaches a minimum average monthly value of $2.41 nm/h$ in November. The nucleation particles diameters growth lasts on average 2:45 hours, ranging from 12:33 to 15:18. It generally begins earlier in summer when it also lasts less. In wintertime the growth of Dp_{nuc} starts later than any other season, but it lasts longer in autumn. The same studies conducted for the growth rate are performed for the time evolution of N_{nuc}, which mean rate is $0.50 cm^{-3} s^{-1}$. The monthly average dN_{nuc}/dt has a maximum value in September of $1.77 cm^{-3} s^{-1}$ and a minimum in October of $0.22 cm^{-3} s^{-1}$. The beginning of N_{nuc} growth is on average 12:12, while the growth stops on average at 13:50. The seasonal average time lengths are all quite close to the mean annual duration of 1:38 hours. The study on condensation sink reports that daily variation of CS for non-events is characterized by a quite constant value which is on average $0.280 \cdot 10^{-3} s^{-1}$. In contrast, even if CS for events has a greater mean daily value of $0.483 \cdot 10^{-3} s^{-1}$, it exhibits a decrease during morning hours, consistent with the fact that low condensation sink can be an important factor triggering new particle formation (Kulmala et al., 2005), and an increase during afternoon explainable by the increase of surface area available as a result of new particle formation. The seasonal CS for events during the time interval before the nucleation onset over an event day (from 5:00 to 10:00) is on average always lower than the one retrieved over a whole non-event day, except during wintertime, probably because vapor availability is the limiting factor in this season, when Mt. Cimone is completely decoupled from the polluted PBL and air masses from the ground surface.

Thanks to the long term characterization of the aerosol population carried out in this thesis and the study conducted on NPF occurrences, Mt. Cimone station can be compared to other sites connected to the Global Atmosphere Watch network. The comparison of number concentration observed at CMN station is done with those reported in the article by Laj et al., 2020, showing that Mt. Cimone, as well as other mountain and non-urban continental and coastal sites, features an intermediate average N_{tot} ($\sim 10^2 - 10^3 cm^{-3}$) with respect to the highest values observed at urban sites ($\sim 10^3 - 10^4 cm^{-3}$) and the lowest observed at polar sites ($\sim 10^2 cm^{-3}$). Moreover, a median number concentration very close to the value measured at CMN is recorded at Lulin (LLN) and at Sonnblick (SNB) mountain sites. Regarding the seasonal cycle of N_{tot}, the most clear seasonality is typical of polar sites, while urban stations exhibit a weak variation over the year, connected with the vicinity to sources that are relatively constant through the year. However, mountain sites like CMN, exhibit more pronounced seasonality relative to lowland stations. The NPF features and frequencies, instead, are compared to those obtained by long term data from six high altitude ground-based stations and other literature data reported in the paper

written by Sellegri et al., 2019. It follows that NPF frequencies at high altitudes are extremely variable, as the environments where data have been collected are very different, spanning from tropical to nearly polar sites. Even if there isn't a clear dependency between NPF frequency and altitudes, mountain station feature roughly higher frequencies than those located below 1000m a.s.l.. CMN is compared to stations with similar altitudes and it exhibits a NPF frequency of 26.7% very close to that observed at IZO (30.0%), higher than that recorded at MUK (14.5%) and much lower than that of 67% registered at MDO. Concerning the condensation sink, the observations show that the impact of CS on the occurrence of NPF at high altitude appeared to be different from site to site. At CMN, by conducing a seasonal study, CS is lower few hours before the mean NPF onset time as it was observed at PUY, except on wintertime when the site is representative of the lower free atmosphere and very little condensable vapours are available for NPF. Moreover, GR at CMN, as well as that observed at PUY and JFJ, is on average close to the mean GR reported in the literature for sites located below 1000m a.s.l..

This work can be considered the base for future studies on the processes connected to NPF at Mt. Cimone. More information could be found by studying meteorological variables, namely temperature, relative humidity and cloud cover. Solar radiation is an another fundamental factor which should be taken into account, because in this work it was already noticed that most of the events occurs around noon, when the maximum solar irradiance is achieved. Moreover NPF can be better characterized, through the calculation of formation rate, that was not included in this thesis. Further research is needed to find out which chemical substances undergo nucleation and which substances take part in the growth process for the various atmospheric situations in which nucleation occurs. These substances have to be measured quantitatively (Curtius, 2009), but this need a huge effort in term of instrumentation and human resources. Anyway, it is possible to use proxy for anthropogenic activities, already measured at CMN, such as black carbon or carbon monoxide. These proxies, combined with a deep analysis of the atmospheric circulation (back trajectory model), will allow to better describe which are the conditions favoring the NPF events at CMN.

Acknowledgment

I would like to express my special thanks to Professor Federico Porcù, who gave me the great opportunity to do this wonderful experience by introducing me to the fascinating world of scientific research at the National Research Council.

I am very thankful to Dr. Angela Marinoni whose guidance, suggestions and courtesy have contributed immensely to the evolution of my thesis.

I express my deep sense of gratitude to Dr. Angelo Lupi for his encouragement, constant supervision, as well as for his huge patience in following me closely despite being often far away.

I take the opportunity to extend my appreciation to all the professors of my Master's degree programme, for always stimulating my curiosity with their genuine passion for Science.

I would like to warmly thank all my colleagues for being the best I could imagine; I hope to see them as soon as possible in Bologna, to celebrate together and to make up for time lost due to the pandemic.

Thanks to my best friends for always being there and for all the wonderful adventures, long dinner nights, laughter and wonderful moment we shared together, and all those yet to come.

Two special people deserve a special thanks: Mavi for being the best company in my every day routine, making my days brighter, and Bianca, since we first met at University I knew she'd be my greatest mate.

An immense thank you to my parents, Luciana and Germano, and my brother, Michele; I know I have the strength to handle anything in this world as long as I have the love of my family behind me.

Lastly, thanks to my amazing and supportive boyfriend, Mattia, for all nights and weekends spent helping me; there are no words that say thank you enough for everything you have done.

February 25, 2021   *Martina Mazzini*

Nomenclature

σ_g Geometric standard deviation

$CoagS$ Coagulation sink

CS Condensation sink

Dp Electrical mobility diameter

Dp_g Geometric particle diameters

GR Growth rate

J Formation rate

n_N Aerosol number distribution

n_S Aerosol surface distribution

n_V Aerosol volume distribution

N_{acc} Number concentration of accumulation mode particles

N_{Ait} Number concentration of Aitken mode particles

N_{nuc} Number concentration of nucleation mode particles

N_{tot} Total aerosol number concentration

ASD   Aerosol size distribution

CCN   Cloud condensation nuclei

CPC   Condensation particle counter

DMA   Differential mobility analyzer

DMPS   Differential mobility particle sizer

ERFaci   Effective radiative forcing due to aerosol–cloud interactions

ERFari   Effective radiative forcing due to aerosol–radiation interactions

ERF Effective radiative forcing

FT   Free troposphere

GAW Global Atmosphere Watch Programme

IN   Ice nuclei

NPF New particle formation

NPSD Number particle size distribution

PBL Planet boundary layer

POA Primary organic aerosols

RFaci Radiative forcing due to aerosol–cloud interactions

RFari Radiative forcing due to aerosol–radiation interactions

RF   Radiative forcing

SD   Standard deviation

SOA Secondary organic aerosols

VOC Volatile organic compounds

WMO World Meteorological Organization

CHC Mt. Chacaltaya station, Bolivia (5340m a.s.l.)

CMN Mt. Cimone station, Italy (2165m a.s.l.)

IZO Izaña station, Tenerife island, Spain (2373m a.s.l.)

JFJ Jungfraujoch station, Switzerland (3580m a.s.l.)

MDO Maïdo mount, La Reunion Island, France (2160m a.s.l.)

MLO Mauna Loa Observatory , Hawaii, USA (3397m a.s.l.)

MUK Mukteshwar station, India (2180m a.s.l.)

PUY Puy de Dôme research station, France (1465 m asl)

SPL Storm Peak Laboratory, USA (3210m a.s.l.)

a.s.l. Above sea level

DJF Winter months: December, January and February

JJA Summer months: June, July and August

List of Figures

List of Tables

References

Arneth, Almut et al. (2016). "Future vegetation–climate interactions in Eastern Siberia: an assessment of the competing effects of CO 2 and secondary organic aerosols". In: *Atmospheric Chemistry and Physics* 16.8, pp. 5243–5262.

Baron, PAUL A and K Willeke (2001). "Gas and particle motion". In: *Aerosol measurement: principles, techniques, and applications* 2, pp. 61–82.

Bellouin, N (2014). "Role in Climate Change". In: *Encyclopedia of Atmospheric Sciences* 1, p. 76.

Bernstein, Jonathan A et al. (2004). "Health effects of air pollution". In: *Journal of allergy and clinical immunology.*

Berthet, Sarah et al. (2010). "Scavenging of aerosol particles by rain in a cloud resolving model". In: *Atmospheric Research* 96.2-3, pp. 325–336.

Bohren, Craig F and Donald R Huffman (2008). *Absorption and scattering of light by small particles.* John Wiley & Sons.

Bonasoni, P et al. (2002). "The Mt. Cimone Research Station". In: *Workshop on "Atmospheric Research at the Jungfraujoch and in the Alps"*, p. 37.

Boucher, Olivier (2015). "Atmospheric aerosols". In: *Atmospheric Aerosols.* Springer.

Boulon, J et al. (2010). "New particle formation and ultrafine charged aerosol climatology at a high altitude site in the Alps (Jungfraujoch, 3580 m asl, Switzerland)". In: *Atmospheric Chemistry and Physics* 10.19, pp. 9333–9349.

Boulon, J et al. (2011). "Investigation of nucleation events vertical extent: a long term study at two different altitude sites". In: *Atmospheric Chemistry and Physics* 11.12, pp. 5625–5639.

Bouwman, AF et al. (1997). "A global high-resolution emission inventory for ammonia". In: *Global biogeochemical cycles.*

Boy, Ma and M Kulmala (2002). "Nucleation events in the continental boundary layer: Influence of physical and meteorological parameters". In: *Atmospheric Chemistry and Physics* 2.1, pp. 1–16.

Brattich, E et al. (2020). "Advection pathways at the Mt. Cimone WMO-GAW station: Seasonality, trends, and influence on atmospheric composition". In: *Atmospheric Environment* 234, p. 117513.

Bychkov, Vladimir L, Gennady V Golubkov, and Anatoly I Nikitin (2010). *The Atmosphere and Ionosphere*. Springer. Chap. 2: Formation of Aerosols in the Atmosphere.

Chan, YC et al. (1999). "Source apportionment of visibility degradation problems in Brisbane (Australia) using the multiple linear regression techniques". In: *Atmospheric Environment* 33.19, pp. 3237–3250.

Chowdhury, Sourangsu et al. (2020). "Changing risk factors that contribute to premature mortality from ambient air pollution between 2000 and 2015". In: *Environmental Research Letters* 15.7, p. 074010.

Colbeck, I and Mihalis Lazaridis (2014). *Aerosol Science*. Wiley Online Library.

Colombo, T et al. (2000). "Biospheric influence on carbon dioxide measurements in Italy". In: *Atmospheric environment* 34.29-30, pp. 4963–4969.

Cristofanelli, P et al. (2009). "Significant variations of trace gas composition and aerosol properties at Mt. Cimone during air mass transport from North Africa–contributions from wildfire emissions and mineral dust". In: *Atmospheric Chemistry and Physics* 9.14, pp. 4603–4619.

Cristofanelli, Paolo et al. (2016). "Summer atmospheric composition over the Mediterranean basin: Investigation on transport processes and pollutant export to the free troposphere by observations at the WMO/GAW Mt. Cimone global station (Italy, 2165 m asl)". In: *Atmospheric Environment* 141, pp. 139–152.

Cristofanelli, Paolo et al. (2017). *High-mountain Atmospheric Research: The Italian Mt. Cimone WMO/GAW Global Station (2165 M Asl)*. Springer.

— (2018). "The "O. Vittori" Observatory at Mt. Cimone: A "Lighthouse" for the Mediterranean Troposphere". In: *High-Mountain Atmospheric Research*. Springer, pp. 1–14.

Curtius, J (2009). "Nucleation of atmospheric particles". In: *EPJ Web of Conferences*. Vol. 1. EDP Sciences, pp. 199–209.

Dal Maso, Miikka et al. (2005). "Formation and growth of fresh atmospheric aerosols: eight years of aerosol size distribution data from SMEAR II, Hyytiala, Finland". In: *Boreal environment research* 10.5, p. 323.

DeCarlo, Peter F et al. (2004). "Particle morphology and density characterization by combined mobility and aerodynamic diameter measurements. Part 1: Theory". In: *Aerosol Science and Technology* 38.12, pp. 1185–1205.

Deng, Hua et al. (2016). "Impact of relative humidity on visibility degradation during a haze event: a case study". In: *Science of the Total Environment* 569, pp. 1149–1158.

Dinoi, Adelaide et al. (2020). "Long-term characterization of submicron atmospheric particles in an urban background site in Southern Italy". In: *Atmosphere* 11.4, p. 334.

Douglas, Alyson and Tristan L'Ecuyer (2020). "Quantifying cloud adjustments and the radiative forcing due to aerosol–cloud interactions in satellite observations of warm marine clouds". In: *Atmospheric Chemistry and Physics* 20.10, pp. 6225–6241.

Engelhart, GJ et al. (2011). "Water content of aged aerosol". In: *Atmospheric Chemistry and Physics* 11.3, p. 911.

Epa, US (2004). "Air quality criteria for particulate matter". In: *US Environmental Protection Agency, Research Triangle Park.*

Erupe, Mark E et al. (2010). "Correlation of aerosol nucleation rate with sulfuric acid and ammonia in Kent, Ohio: An atmospheric observation". In: *Journal of Geophysical Research: Atmospheres* 115.D23.

Feingold and Graham (2003). "Modeling of the first indirect effect: Analysis of measurement requirements". In: *Geophysical research letters* 30.19.

Fischer, H et al. (2003). "Ozone production and trace gas correlations during the June 2000 MINATROC intensive measurement campaign at Mt. Cimone". In: *Atmospheric Chemistry and Physics* 3.3, pp. 725–738.

Flagan, RC (2001). "Electrical techniques". In: *Aerosol Measurement: Principles, Techniques, and Applications*, pp. 537–568.

Foucart, Brice et al. (2018). "High occurrence of new particle formation events at the Maïdo high-altitude observatory (2150 m), Réunion (Indian Ocean)". In: *Atmospheric Chemistry and Physics* 18.13, pp. 9243–9261.

Gryspeerdt, Edward et al. (2019). "Constraining the aerosol influence on cloud liquid water path." In: *Atmospheric Chemistry & Physics* 19.8.

Guelle, W et al. (1998). "Wet deposition in a global size-dependent aerosol transport model: 1. Comparison of a 1 year 210Pb simulation with ground measurements". In: *Journal of Geophysical Research: Atmospheres* 103.D10, pp. 11429–11445.

Hansen, J, Mki Sato, and R Ruedy (1997). "Radiative forcing and climate response". In: *Journal of Geophysical Research: Atmospheres* 102.D6, pp. 6831–6864.

Hicks, BB et al. (1987). "A preliminary multiple resistance routine for deriving dry deposition velocities from measured quantities". In: *Water, Air, and Soil Pollution* 36.3-4, pp. 311–330.

Hinds, William C (1999). *Aerosol technology: properties, behavior, and measurement of airborne particles.* John Wiley & Sons.

Hirsikko, Anne et al. (2007). "Identification and classification of the formation of intermediate ions measured in boreal forest". In:

Hosker Jr, RP and Steven E Lindberg (1982). "Atmospheric deposition and plant assimilation of gases and particles". In: *Atmospheric Environment (1967)* 16.5, pp. 889–910.

Hussein, Tareq et al. (2005). "Evaluation of an automatic algorithm for fitting the particle number size distributions". In: *Boreal environment research* 10.5, p. 337.

Hussein, Tareq et al. (2008). "Observation of regional new particle formation in the urban atmosphere". In: *Tellus B: Chemical and Physical Meteorology* 60.4, pp. 509–521.

Jacobson, MC et al. (2000). "Organic atmospheric aerosols: Review and state of the science". In: *Reviews of Geophysics* 38.2, pp. 267–294.

Jaenicke, Ruprecht (1993). "Tropospheric aerosols". In: *International Geophysics.* Vol. 54. Elsevier, pp. 1–31.

Järvinen, E et al. (2013). "Seasonal cycle and modal structure of particle number size distribution at Dome C, Antarctica". In: *Atmospheric Chemistry and Physics* 13.15, pp. 7473–7487.

Kalkavouras, Panayiotis et al. (2021). "Regional New Particle Formation over the Eastern Mediterranean and Middle East". In: *Atmosphere* 12.1, p. 13.

Kerminen, Veli-Matti et al. (2018). "Atmospheric new particle formation and growth: review of field observations". In: *Environmental Research Letters* 13.10, p. 103003.

Kim, Minjoong J (2019). "Sensitivity of nitrate aerosol production to vehicular emissions in an urban street". In: *Atmosphere.*

Knutson, EO and KT Whitby (1975). "Aerosol classification by electric mobility: apparatus, theory, and applications". In: *Journal of Aerosol Science* 6.6, pp. 443–451.

Kulkarni, Pramod, Paul A Baron, and Klaus Willeke (2011). *Aerosol measurement: principles, techniques, and applications.* John Wiley & Sons.

Kulmala, Markku, KEJ Lehtinen, and A Laaksonen (2006). "Cluster activation theory as an explanation of the linear dependence between formation rate of 3nm particles and sulphuric acid concentration". In:

Kulmala, Markku et al. (2005). "On the growth of nucleation mode particles: source rates of condensable vapor in polluted and clean environments". In: *Atmospheric Chemistry and Physics* 5.2, pp. 409–416.

Kulmala, Markku et al. (2012). "Measurement of the nucleation of atmospheric aerosol particles". In: *Nature protocols* 7.9, pp. 1651–1667.

Kulmala, Maso et al. (2001). "On the formation, growth and composition of nucleation mode particles". In: *Tellus B* 53.4, pp. 479–490.

Laj, Paolo et al. (2020). "A global analysis of climate-relevant aerosol properties retrieved from the network of Global Atmosphere Watch (GAW) near-surface observatories". In: *Atmospheric Measurement Techniques* 13.8, pp. 4353–4392.

Lehtinen, Kari EJ et al. (2007). "Estimating nucleation rates from apparent particle formation rates and vice versa: Revised formulation of the Kerminen–Kulmala equation". In: *Journal of Aerosol Science* 38.9, pp. 988–994.

Lupi, Angelo et al. (2016). "Multi-seasonal ultrafine aerosol particle number concentration measurements at the Gruvebadet observatory, Ny-Ålesund, Svalbard Islands". In: *Rendiconti Lincei* 27.1, pp. 59–71.

Malm, William C (1999). *Introduction to visibility.* Vol. 40. Cooperative Institute for Research in the Atmosphere, NPS Visibility Program …

Malm, William C and Derek E Day (2001). "Estimates of aerosol species scattering characteristics as a function of relative humidity". In: *Atmospheric Environment* 35.16, pp. 2845–2860.

Merikanto, J et al. (2009). "Impact of nucleation on global CCN". In: *Atmospheric Chemistry and Physics* 9.21, pp. 8601–8616.

Myhre, C Lund and U Baltensberger (2012). "Recommendations for a Composite Surface-Based Aerosol Network". In: *GAW Report n. 207.*

Olenius, Tinja et al. (2018). "New particle formation and growth: Creating a new atmospheric phase interface". In: *Physical Chemistry of Gas-Liquid Interfaces.* Elsevier, pp. 315–352.

Peng, JF et al. (2014). "Submicron aerosols at thirteen diversified sites in China: size distribution, new particle formation and corresponding contribution to cloud condensation nuclei production". In: *Atmospheric Chemistry and Physics* 14.18, pp. 10249–10265.

Penner, Joyce E (2019). *Soot, sulfate, dust and the climate—Three ways through the fog.*

Perrino, Cinzia (2010). "Atmospheric particulate matter". In: *Biophysics and Bioengineering Letters* 3.1.

Ramanathan, VCPJ et al. (2001). "Aerosols, climate, and the hydrological cycle". In: *science* 294.5549, pp. 2119–2124.

Renzi, Laura (2019). "Characterization of atmospheric aerosol absorption properties at different sites in the Po Valley during ACTRIS-2 experiment." MA thesis. Alma Mater Studiorum - Università di Bologna.

Rose, Clémence et al. (2015). "Frequent nucleation events at the high altitude station of Chacaltaya (5240 m asl), Bolivia". In: *Atmospheric Environment* 102, pp. 18–29.

Salimi, Farhad (2014). "Characteristics of spatial variation, size distribution, formation and growth of particles in urban environments". PhD thesis. Queensland University of Technology.

Seinfeld, John H and Spyros N Pandis (2016). *Atmospheric chemistry and physics: from air pollution to climate change.* John Wiley & Sons.

Sellegri, Karine et al. (2019). "New particle formation: a review of ground-based observations at mountain research stations". In: *Atmosphere* 10.9, p. 493.

Shiraiwa, Manabu et al. (2017). "Aerosol health effects from molecular to global scales". In: *Environmental science & technology* 51.23, pp. 13545–13567.

Sipilä, Mikko et al. (2008). "Applicability of condensation particle counters to measure atmospheric clusters". In:

Small, Jennifer D et al. (2009). "Can aerosol decrease cloud lifetime?" In: *Geophysical Research Letters* 36.16.

Solomon, Susan et al. (2007). *IPCC 2007. Climate change the physical science basis.* Cambridge university press Cambridge, United Kingdom and New York, NY, USA.

Stocker, Thomas F et al. (2013). *IPCC 2013. Climate change, the physical science basis.* Cambridge university press Cambridge, United Kingdom and New York, NY, USA. Chap. 7.

Szymanski, W and PE Wagner (1983). "Aerosol size distribution during a condensational growth process. Measurements and comparison with theory". In: *Atmospheric Environment (1967)* 17.11, pp. 2271–2276.

Tomasi, Claudio, Sandro Fuzzi, and Alexander Kokhanovsky (2017). *Atmospheric aerosols: Life cycles and effects on air quality and climate.* John Wiley & Sons.

Tunved, Peter, Johan Ström, and Radovan Krejci (2013). "Arctic aerosol life cycle: linking aerosol size distributions observed between 2000 and 2010 with air mass transport and precipitation at Zeppelin station, Ny-Ålesund, Svalbard". In: *Atmospheric Chemistry and Physics* 13.7, pp. 3643–3660.

Wang, Chiu-sen (2005). *Inhaled particles.* Elsevier.

Wang, Wan (2010). "Inorganic and organic speciation of atmospheric aerosols by ion chromatography and aerosol chemical mass closure". PhD thesis. Ghent University.

Wang, Yang et al. (2017). "Influence of flame-generated ions on the simultaneous charging and coagulation of nanoparticles during combustion". In: *Aerosol Science and Technology* 51.7, pp. 833–844.

Watson, John G (2002). "Visibility: Science and regulation". In: *Journal of the Air & Waste Management Association* 52.6, pp. 628–713.

Wiedensohler, A et al. (2012). "Mobility particle size spectrometers: harmonization of technical standards and data structure to facilitate high quality long-term observations of atmospheric particle number size distributions". In:

Wu, Yee-Lin et al. (1992). "Dry deposition of atmospheric contaminants: the relative importance of aerodynamic, boundary layer, and surface resistances". In: *Aerosol Science and Technology* 16.1, pp. 65–81.

Xu, Danhui et al. (2019). "Multi-method determination of the below-cloud wet scavenging coefficients of aerosols in Beijing, China". In: *Atmospheric Chemistry and Physics* 19.24, pp. 15569–15581.

Zhang, Jianjun et al. (2012). "Effects of divalent metal ions on the flame retardancy and pyrolysis products of alginate fibres". In: *Polymer degradation and stability* 97.6, pp. 1034–1040.